UC Irvine
UC Irvine Electronic Theses and Dissertations

Title

Role of particle laden interface in the rheology and design of bicontinuous interfacially jammed emulsion gels

Permalink

https://escholarship.org/uc/item/1qg2n2tt

Author

Ching, Herman

Publication Date

2022

Peer reviewed|Thesis/dissertation

UNIVERSITY OF CALIFORNIA,
IRVINE

Role of particle laden interface in the rheology and design of bicontinuous interfacially
jammed emulsion gels

DISSERTATION

submitted in partial satisfaction of the requirements
for the degree of

DOCTOR OF PHILOSOPHY

in Chemical and Biochemical Engineering

by

Herman Ching

Dissertation Committee:
Professor Ali Mohraz, Chair
Professor Elliot L. Bovinick
Professor Vasan Venugopalan

2022

TABLE OF CONTENTS

LIST OF FIGURES

LIST OF TABLES

ACKNOWLEDGEMENTS

VITA

Herman Ching

EDUCATION

2016	Bachelor of Science in Chemical Engineering, University of California, Santa Barbara
2020	Master of Science in Chemical and Biochemical Engineering, University of California, Irvine
2022	Ph.D. in Chemical and Biochemical Engineering, University of California, Irvine

FIELD OF STUDY

Colloidal Science, Polymer Science, Emulsion Science.

PUBLICATIONS

1. Laser cavitation rheology for measurement of elastic moduli and failure strain within hydrogels, J. Luo, **H. Ching**, B. G. Wilson, A. Mohraz, E. L. Botvinick, and V. Vengugopalan. Scientific Reports (2020).
2. Rapid production of bicontinuous macroporous materials using intrinsically polymerizable bijels. **H. Ching**, T. J. Thorson, B. Paul, and A. Mohraz. Materials Advances (2021).
3. Bijel rheology reveals a 2D colloidal glass wrapped in 3D. **H. Ching** and A. Mohraz. Soft Matter (2022).

CONFERENCE PRESENTATIONS

1. Development and rheological characterization of non-volatile bijels, H. Ching, A. Mohraz, 34th Annual Meeting of the American Society for Gravitational and Space Research.
2. Facile Bijel Template Production with Photoreactive Fluid Mixtures, H. Ching, T. J. Thorson, A. Mohraz, 35th Annual Meeting of the American Society for Gravitational and Space Research.
3. Bijel rheology and its link to interfacial particle dynamics, H. Ching, A. Mohraz, 37th Annual Meeting of the American Society for Gravitational and Space Research.

ABSTRACT OF THE DISSERTATION

Role of particle laden interface in the rheology and design of bicontinuous interfacially jammed emulsion gels

by

Herman Ching

Doctor of Philosophy in Chemical and Biomolecular Engineering

University of California, Irvine, 2022

Professor Ali Mohraz, Chair

Bicontinuous interfacially jammed emulsion gels, or bijels, is a class of soft material uniquely characterized by its co-continuous and interpenetrating fluid domains. These novel materials are formed by jamming nano-scale colloidal particles at the interface between two fluids undergoing spinodal decomposition. As such, the internal microstructure of the resulting bijel bears a striking resemblance to the morphology of spinodal decomposition. This unique morphology exhibits attractive transport potentials that are desired in the development of functional porous materials such as bio-implants, electrochemical devices, catalytic devices, separation membranes, and structural supports. However, there is a lack of understanding of the mechanisms that impart stability in bijels, which significantly limits the large-scale production of bijels and their derivatives. To this end, I have performed extensive rheological characterizations to examine the roles of particles and the interface within bijels to elucidate the origin of mechanical stability. First, by testing bijels at different temperatures and particle volume fractions, it was revealed that interfacial jamming alone is sufficient to impart stability in bijels. Second, bijels were deformed near their yield limits to explore the connection between particle jamming and the continuous interface which

percolates the sample. In the transition to yielding, bijels uniquely exhibit a self-rejuvenating quality where shear-induced stretching of the interface is reversible by interfacial compaction. Incorporating approximate particle dynamics under dilute conditions into a simple rheological model produces stress responses that closely mimic the nonlinear rheological response measured from bijels. Lastly, I have developed a bijel templating method that bypasses a significant limiting factor of existing protocols, specifically the addition of monomer to bijels which disrupts the stability of the particle-laden interface. Bijel templating was simplified by forming bijels using partially miscible mixtures of solvent and monomer and directly polymerizing them into porous polymeric scaffolds for further processing. My results provide insights into the fundamental physics of bijels and pave ways for mass production of bijel-derivatives.

CHAPTER 1: Introduction

1.1 Bijels

Bicontinuous interfacially jammed emulsion gels, or bijels, are an emerging class of solid stabilized emulsion first conceptualized in 2005 by Stratford et al. using lattice-Boltzmann simulation.[1] Unlike typical emulsions, where immiscible mixtures of fluids (such as oil and water) form discrete droplets, bijels were envisioned to comprise two separate fluid domains which are fully continuous to themselves. A 3-dimensional (3D) rendering of such a structure is shown in Fig. 1.1. The fascinating feature of bijels is the continuous fluid-particle-fluid interface, which has a net-zero negative Gaussian curvature throughout that separates the fluids into two separate uniform and unrestricted domains. This unique morphology opens up the possibility for advanced transport properties that are desirable in the development of nano- or mesoporous material.[2–4] As such, it took a mere two years for researchers to experimentally realize this novel emulsion using a semi-miscible mixture of water and 2,6-lutidine and near-neutrally wetting colloidal silica.[2]
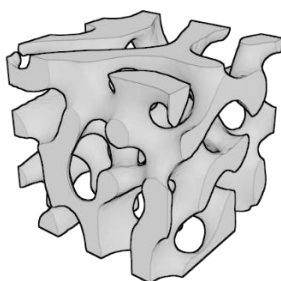
Fig. 1.1 A 3D rendering of bijel showcasing its unique bicontinuous morphology. The solid grey matter and the void each presents one continuous fluid phase.

To form bijels, typically process involves initiating spinodal decomposition in a partially miscible mixture of fluids mixed with neutrally wetting nanoparticles.[2,5] Upon phase separation, particles are irreversibly adsorbed to the continuous interface with

1

adsorption energy on the orders of >10^4 k_bT, where k_b is the Boltzmann constant, and T is the temperature. The energy can be estimated by the equation:

$$\Delta G = \pi a^2 \sigma_{\alpha\beta}(1 - |cos\theta|)^2,$$

Where a is the particle radius, $\sigma_{\alpha\beta}$ is the fluid-fluid interfacial tension, and θ is the three-phase contact angle.[6] As interfacial tension compresses the interface, particles are compacted into a tightly packed network until particles are jamming and coarsening is arrested. The resulting material is energetically unfavorable but kinetically arrested through mechanical jamming.

The discovery of bijels in 2007 motivated the development of processing techniques to harness their unique morphological attributes in emerging applications such as electrochemical energy storage and conversion,[4,7–12] catalysis,[13,14] and human health devices.[15,16] These efforts are enabled by bijel-templating methods first developed by Lee and Mohraz or Haase et al.[5,17] to transform bijels into polymeric scaffolds with minimal alteration to the internal microstructure. In briefs, these processes involve selective incorporation of polymer precursors into one single fluid phase of the bijels, and subsequent chemically process bijels into a solid scaffold, which can further process into porous functional materials, hierarchical structures, and micro-architected composites. While this is a tried-and-true process on the laboratory scale, there are still many significant obstacles which prevent realization of marketable bijel-derived technologies, most of which stems from our general lack of understanding regarding the origin of stability in bijels.

Since 2007, most research has been invested in processing and applying bijels as functional materials. However, bijels themselves present a plethora of intriguing physics that warrant an in-depth investigation to improve bijel-templating processes and expand our

understanding of solid stabilized interfaces. Unlike traditional solid stabilized emulsions, bijels are kinetically arrested by a monolayer of solid particles closely jammed along the interface by contraction of interfacial tension. In a way, bijels are structurally similar to colloidal gels, where attractive forces link up particles to form a sample spanning network of particles. An early study by Lee et al. demonstrated that incorporating polymer precursor materials to bijels with weak interparticle attraction introduces sufficient internal stress leading to catastrophic breakdown of the internal microstructure.[18] However the origin, or the necessity, of these interparticle attractions remains an open question. Like colloids at the interface, the interparticle attraction in bijels can originate from electrostatic repulsion, hydrophobic attraction, capillary attractions, van der Waals, steric repulsion, solvation mediated attractions, and interfacial compaction,[19] all of which are functions of the chemical potential in the fluid-particle system. Indeed, previous studies on different bijel systems suggested that interparticle attractions are weak and particles are mobile along the fluid-particle-fluid interface.[20–24] While the gel argument is valid, an analogous claim can be made that bijels are glassy materials formed by the concentration of particles by interfacial tension. Identifying mechanism(s) by which bijel stabilizes could aid the designs of mechanically robust bijels, or Pickering emulsion, which resist deformation throughout templating efforts.

Aside from chemical perturbation of the particle-interface layer, processing of bijels typically introduce mechanical forces in the forms of shear or compression. For instance, Lee's method introduces monomer precursors to the top of the bijels, which leads to the gravitational force that compress the bijel.[17] Similarity, in Haase's method, fluids are injected into an inert solvent, raising shear stress on the STRIPS bijel.[5] To date, the underlying

yielding mechanism within bijels remains another unsolved problem. Simple compressional tests have demonstrated the irreversible transformation of the internal microstructure, possibly by the re-arrangement of particles along the interface.[24] Rudimentary rheology of bijels suggests that shearing induces irreversible structural breakdown into droplets (as shown in Fig. 1.2). The ability of bijels to resist structural breakdown is vital in the manufacturing of bijel-related materials. Direct investigation into the origin of yielding in bijels could shed light on the development of manufacturing techniques that circumferent bijel deformation and rupture.
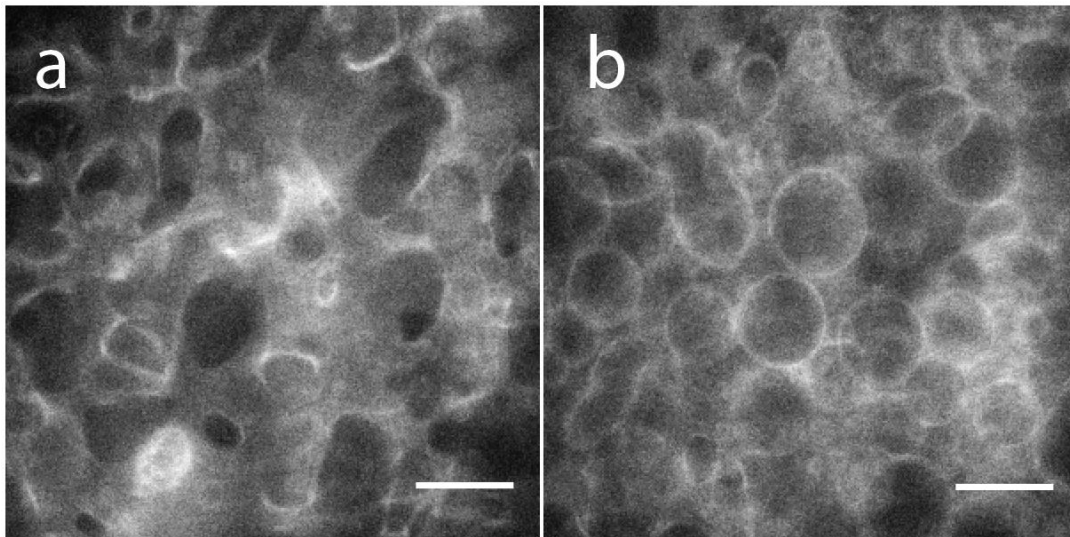
Fig. 1.2 Microstructural breakdown of a bijels after large strain oscillatory shear. Scale bar = 30 μm.

1.2 Bijel rheology

Although bijels are typically formed at low volume fractions of solids (0.005-0.1 vol%), they exhibit surprisingly gel-like and glass-like responses (solid-like). In the seminal work by Herzig et al., it was demonstrated that bijels are self-standing gels with yield stress capable of withstanding the weight of a small wire.[2] Later, Lee and Mohraz conducted the first rheological characterization of bijels using traditional rheometers and demonstrated

gelation-like events following the forming of bijels, where the storage G' and loss G" moduli sharply increase as bijels form. Overtime, both G' and G" plateaus to steady-state values with a predominately G' response, indicative of gel-like behavior (illustrated in Fig. 2.2). Imperiali et al. separately investigated the rheological or bijels via small amplitude oscillatory shear at different frequencies and reported frequency-dependent G" responses reminiscent of glassy materials (exemplified in Fig. 2.4).[22] Bai et al. later revealed aging-like rheology in non-polar bijels comprising polymers and silica nanoparticles, citing possible particle rearrangement at the interface.[23] Rumble et al. and Tavacoli et al. separately introduced compressional stress within bijels and observed isotropic to anisotropic transformation of the fluid domains.[21,24] Macmillan et al. performed rheology with in-Situ confocal microscopy imaging on bijels formed by direct mixing and recorded signatures of fluidization of the interface prior to drastic structural breakdown.[25] Unfortunately, the literature on the rheology of bijels is limited. To address our limited understanding of bijel rheology, Chapter 2 and 3 will heavily focus on examining the rheology of bijels under different conditions, with emphasis on understanding the origin of stability and yielding in bijels.

1.3 Experimental techniques

1.3.1 Linear Rheology

Rheology is the study of the flow of matter. For viscoelastic materials (things that exhibit both solid and liquid mechanical behaviors), such as colloidal gels, emulsions, polymers, and suspensions, rheology is a powerful tool that enables the characterization of the deformation and relaxation behavior of materials. Particularly, oscillatory shear rheology examines the extend of solid-like and liquid-like behaviors of viscoelastic

materials. In these types of experiments, small amounts of sample are placed on a

rheometer (as shown in Fig. 1.3), and shear is applied sinusoidally at a fixed frequency ω:

$$\gamma(t) = \gamma_0 \sin(\omega t),$$

where γ and γ_0 is the strain and strain amplitude, respectively. If the material is perfectly

elastic, the resulting stress will be in-phase with the applied strain, and it is governed by

the equation $\sigma = E^*\gamma$, where σ is the stress and E is the elastic modulus. For viscous

materials, the stress is proportional to the shear rate (90 degree off-phase from the applied

strain), and it is governed by the equation $\sigma = \eta^*\dot{\gamma}$, where η is the viscosity. By measuring

the phase angle (δ) between the applied strain and the resulting stress, and the stress

amplitude σ_0, the elastic (G') and loss (G") moduli can be calculated by:

$$G' = \frac{\sigma_0}{\gamma_0}\cos(\delta)$$

$$G'' = \frac{\sigma_0}{\gamma_0}\cos(\delta)$$

The quantities G' and G'' are important measures of the material's ability to store and

dissipate elastic energy, respectively. Comparison between the two moduli can also offer a

simplistic handle on whether a material is predominantly elastic or viscous, i.e., when

$G'>G''$, the material is elastic-like, and when $G''>G'$, the material is viscous-like.
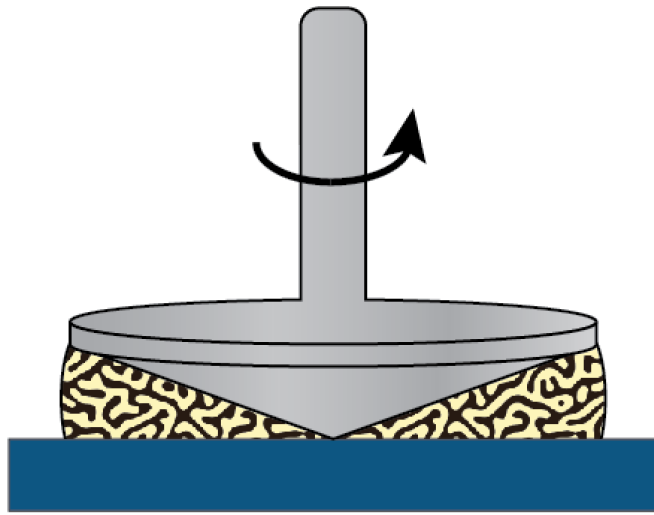
Fig. 1.3 Schematic illustration of a sample (bijel, not to scale) being shear by a cone-and-plate geometry.

Oscillatory rheology is presented throughout Chapters 2 and 3 to illustrate the rheological properties of bijels. Constant amplitude and constant frequency small amplitude oscillatory shear (SAOS) tests allow monitoring of time-dependent behavior such as aging in bijels (exemplified in Fig. 2.2). Constant amplitude oscillatory experiments performed over a range of frequencies (frequency sweeps) reveal frequency or shear rate-dependent behaviors that could have profound implications for the relaxation dynamics of viscoelastic materials (exemplified in Fig. 2.4). In glass-forming materials such as bijels, G' and G'' exhibit a wide range of frequency-dependent behaviors as shown in Fig. 1.4. At low frequency, the sample is dominated by liquid-like behavior, and it is considered "fluidized." At intermediate frequencies, G' crosses over G'' and the material is predominately elastic in a "rubbery state." The G' transitions to a second plateau called the "glassy state" as

frequency increases. Here the material is arrested or jammed, resulting in high shear

moduli with a dominant G' effect.
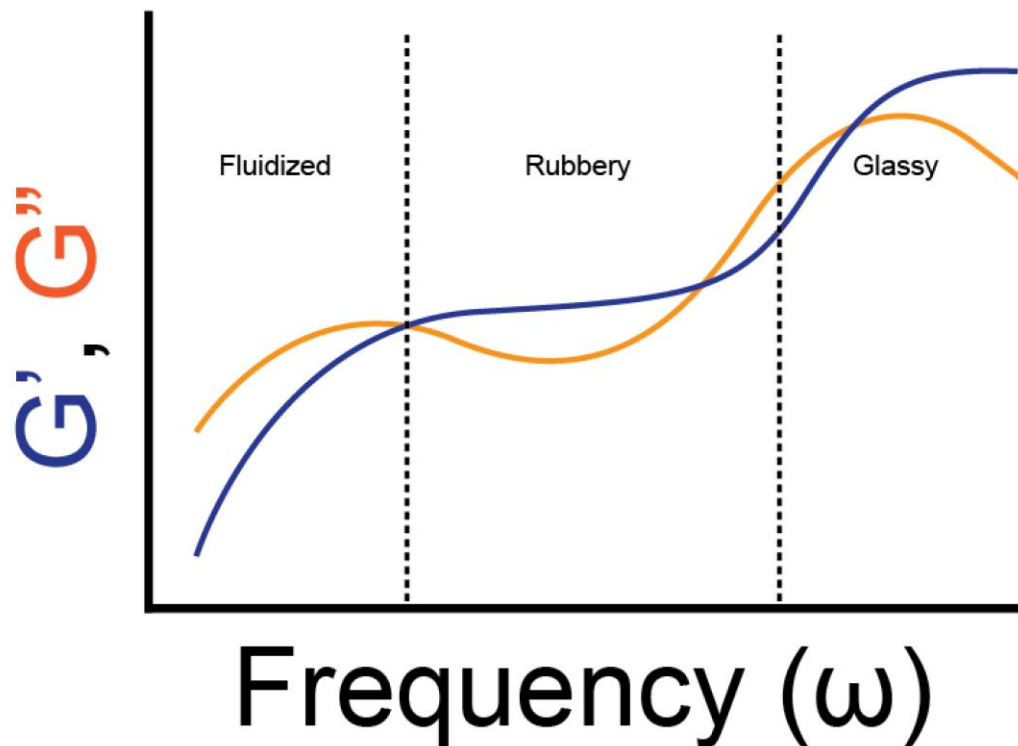
Fig. 1.4 Characteristic frequency sweep of glass forming materials.

1.3.2 Nonlinear rheology

For bijels, and many other structured viscoelastic materials exhibiting yield stress,

large strain deformation can induce microstructural yielding and manifest weakening

effects. Increasing the oscillatory amplitude at constant frequency allows for monitoring of

G' and G'' in response to large strain deformations, as exemplified in Fig. 1.5.
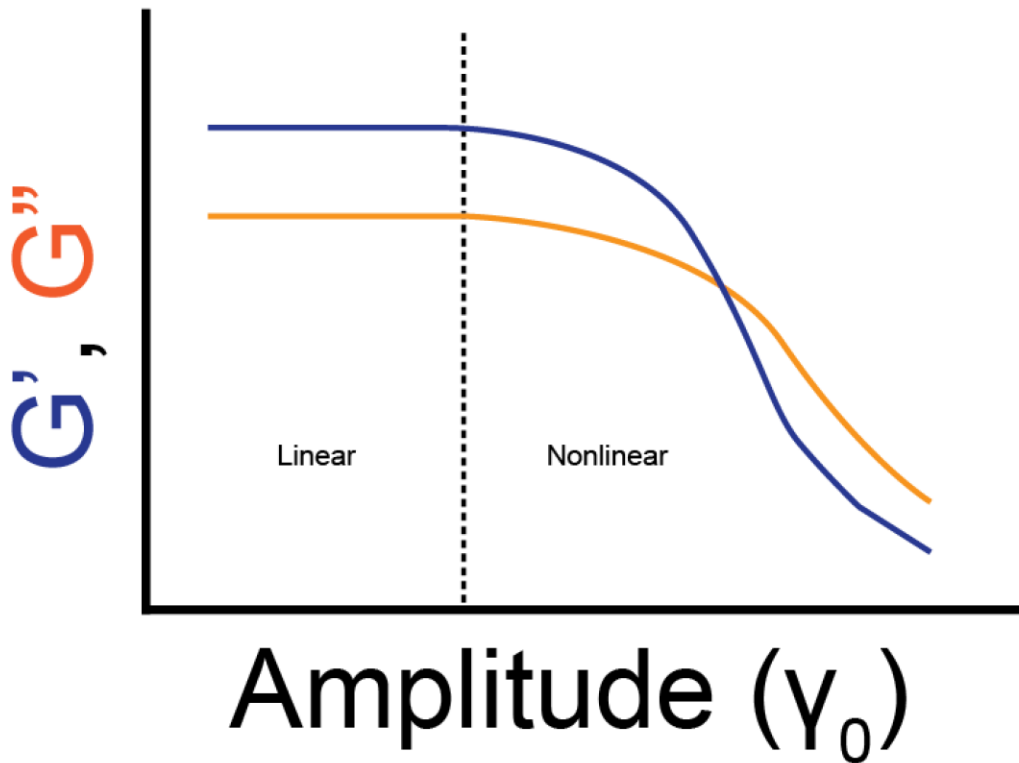
Fig. 1.5 Characteristic amplitude sweep on a gel-like or glass-like material.

This test can also pinpoint the limit of linear viscoelasticity by locating the range of shear amplitude in which the material's behaior is strain independent, i.e., the range where the material has not yielded. At larger strains, the proportionality between stress and strain or stress and shear rate are no longer linear functions, and G' and G'' only offer a simple representation of the general mechanical properties. The nonlinearity between stress and applied strain can reveal important information regarding the nature of yielding. In Chapter 3, frequency sweeps were conducted at increasing strains to explore the nonlinear rheological properties of bijels, which enables examination of the origin of yielding in bijels. To measure these nonlinearities, the stress response to applied strain is recorded over time, and the deviation from linear behavior is analyzed, as exemplified in Fig. 3.4. The

stress and strain information can also be plotted as a Lissajous curve where stress vs. strain is plotted (exemplified in Fig. 1.6).
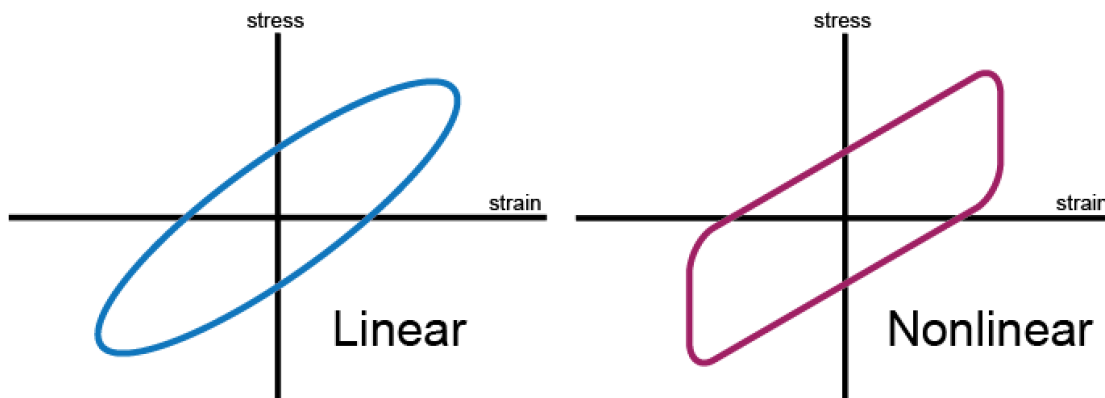
Fig. 1.6 Schematic representations of linear (left) vs. nonlinear (right) viscoelasticity in Lissajous curves, where stress vs. strain is plotted.

1.4 Dissertation Objectives

This dissertation is structured as follows. In Chapter 1, I will examine the linear viscoelasticity of bijels by performing frequency sweeps at different temperatures and particle volume fractions. The rheology results will be supplemented with energetic approximations of the interparticle attraction energy within bijels to understand better whether attractive interactions are necessary. An analogous colloidal system will be presented and tested with rheology to qualitatively demonstrate the rheology of colloidal gels stabilized solely by interparticle attractions. Chapter 2 will follow up with an investigation of the nonlinear rheology of bijels. Bijels are sheared to intermediate amplitudes to investigate the origin of yielding. It is shown that the rheology of bijels is governed by the dynamics of particles at the interface, which can be fluidized by stretching of the interface, resulting in shorter relaxation time scales. Having demonstrated the

importance of the particle-interface layer in bijel stability, Chapter 4 will focus on a bijel

templating method that bypasses the limitations of existing protocols. Specifically, I present

a protocol in which no mechanical or chemical stresses are applied to the bijel once formed,

and bijels can be rapidly polymerized into a polymeric scaffold. Lastly, in Chapter 5, I

conclude my dissertation with a summary of my work and future potential endeavors.

CHAPTER 2: Bijel rheology reveals a 2D colloidal glass wrapped in 3D

2.1 Introduction

Bicontinuous interfacially jammed emulsion gels, or bijels, are multiphase soft materials comprised of interpenetrating co-continuous fluid domains separated by a monolayer of colloidal particles.[1,26] Bijels are typically formed by incorporating a kinetic trap, namely an interfacial jamming step, along the phase separation pathway of a liquid mixture undergoing bicontinuous demixing.[5,27] A commonly used protocol for bijel formation involves preparing a partially miscible binary liquid mixture at its critical composition and rapidly changing its thermodynamic state from miscible to immiscible, for example via a temperature quench as schematically shown in Fig. 2.1a, in the presence of neutrally wetting colloidal particles.[2] The rapid quench results in spinodal decomposition and the neutrally wetting particles get irreversibly adsorbed onto the fluid-fluid interface.[3] Reduction of interfacial area by phase separation eventually results in colloidal jamming at the interface, which halts demixing and imparts mechanical stability to the mixture.[28,29] The resulting material bears a spinodal-like morphology with co-continuous fluid domains, nearly uniform and tunable domain size,[2,15] and a continuous interface with zero mean, negative Gaussian curvatures.[3,30] Owing to these unique microstructural attributes and their inherent scalability,[5] bijels have attracted considerable attention for functional materials syntheses such as cell delivery scaffolds and regenerative biomaterials,[15,16] electrochemical device components,[7–10,4,11,12] high surface area catalysts,[13] separation membranes,[14] and structural supports.[31]

While applied research on the use of bijels for materials synthesis has enjoyed significant advances in the past decade, our fundamental understanding of bijels has not experienced similar growth. For example, the rheology of bijels is a rich area with a plethora of interrelated questions at both the microscopic and macroscopic scales that have not yet been fully addressed. In their 2008 article introducing bijels as a new class of soft materials, Clegg and Cates posed the question of whether attractive interparticle interactions are necessary for bijel stability.[3] Here, we rephrase this question as follows: are the rheological properties of bijels best explained in the context of 2-dimensional (2D) colloidal glasses or 3-dimensional (3D) colloidal gels? The 2D glass viewpoint is justified by the jammed particle monolayer that is constrained to the fluid-fluid interface. On the other hand, one can view the particles as having formed a self-supporting network at a low volume fraction (typically $\phi < 0.02$ in bijels) that spans the entire 3D sample volume and imparts mechanical stability to the mixture, an unequivocal signature of colloidal gels.[32] A principal differentiator between these perspectives is the nature of interparticle interactions: dilute colloidal gels require strong (>10 k_BT, where k_B is the Boltzmann constant, and T is the absolute temperature) attractive interparticle interactions to form a percolating network and remain mechanically stable, whereas the interactions in basic colloidal glasses are hard sphere-like, with elasticity arising from particle caging.[33] Since interparticle interactions have a profound impact on the rheology of particulate suspension,[34,35] this relationship can be exploited to investigate the possible importance of attractive interactions for bijel stability. Aside from its scientific significance, the nature of interparticle interactions and its impact on rheology has profound implications for the processability of bijels and the ability to transform them into functional materials.[18] Namely, the bijel processing protocols first pioneered in our

laboratory involve a monomer exchange step that can induce Marangoni stresses and cross-flow within the bijel interior, resulting in structural breakdown if the particle monolayer is not strong enough to withstand these effects.[18] Therefore, a deeper understanding of the nature of interparticle interactions in bijels can also pave the way for the chemical library of bijel-derived materials to be expanded, and their technological applications to evolve from proof-of-concept demonstrations to large scale production.

In pursuit of better understanding the underlying physics behind bijel stability, various groups have conducted rheological characterizations of bijels. In 2013, Lee et al. reported a gelation-like event following the formation of water/2,6-lutidine (W/L) and nitromethane/ethylene glycol (NM/PG) bijels, characterized by sharp increases in both the storage (G') and loss (G'') moduli, with a dominating G' signal.[18] The authors also identified notable rheological differences between the two bijels, attributing them to possible system-specific interparticle interactions. In that same year, Imperiali et al. studied a W/L bijel under small amplitude oscillatory shear (SAOS) at various frequencies (ω) and observed a nearly flat $G'(\omega)$ response and a notable minimum in $G''(\omega)$, and cited this behavior as soft glassy-like.[22] Bai et al. later revealed an aging behavior following the formation of non-polar bijels and attributed it to the rearrangement of particles at the interface.[23] Rumble et al. and Tavacoli et al. separately compressed bijels and reported anisotropic rearrangement of the fluid domains, attributing it to particles re-jamming at the interface after deformation.[21,24] Macmillan et al. investigated the yielding of bijels formed by direct mixing and observed a two-step yielding process where the jammed interface appears to be fluidized prior to structural breakdown.[25] These studies concluded that the rheology of bijels is intimately linked to the properties of the particle monolayer, and that particle rearrangements along

14

the fluid-fluid interface are possible. However, they have not directly addressed the possible necessity of attractive interparticle interactions for stability, and whether they play an important role in bijel rheology.

To address this knowledge gap, here we report a set of experiments that are particularly sensitive to the nature of interparticle interactions, contributing important new information to the existing body of literature on bijel rheology. To enable these tests, we first developed a new bijel system comprising 1,4-butanediol (14BD), propylene carbonate (PC), and neutrally wetting colloidal silica, with physiochemical properties that are suitable for long-duration rheological measurements on a traditional rheometer. These properties include low volatility of the solvents (vapor pressures of 1.1×10^{-2} and 5.8×10^{-2} mmHg at 25°C for 14BD and PC, respectively),[36,37] and an upper critical solution temperature (UCST) of 30.3°C, which renders the miscibility gap easily accessible and enables measurements at near-ambient temperatures.[18] The longevity of this new bijel system allows for rheology tests that are difficult or impossible to perform using most other systems due to possible evaporation of solvents over extensively long testing periods. We performed comprehensive frequency sweep measurements both within and beyond the limit of linear viscoelasticity in bijels. We used temperature as a handle to modulate the interfacial tension, and colloid volume fractions to vary the interfacial curvature, both of which would influence the degree of attractive capillary interactions between the particles,[38] if such forces were significant. These measurements provide critical insights into the dynamics of particle rearrangements in scenarios that are highly sensitive to the nature of interparticle interactions. We demonstrate that the linear rheology of bijels can be fully explained by an early adaptation of the Mode Coupling Theory (MCT) for a soft glassy system, with clear indications that

15

attractive interactions are not responsible for particle localization and viscoelasticity. The frequency response of the bijels within and beyond the limit of viscoelasticity are then compared to a colloidal gel stabilized by capillary bridges as a representative system in which attractive capillary interactions are necessary for stability, highlighting qualitative differences between the two. Overall, our findings indicate that bijels are adequately described as 2D colloidal glasses weaving in 3D space, and attractive interparticle interactions are not responsible for their viscoelasticity and mechanical stability. Our results also shed light on the dynamics of jammed particles along a fluid-fluid interface and the role of particle-laden interfaces in the rheology of the broader class of multiphase mixtures such as Pickering emulsions and solid-stabilized foams. Finally, our findings provide critical insights for designing processing protocols to convert bijels into functional materials, since processability has been shown to be linked to rheology and the nature of interparticle interactions in bijels.[18]

2.2 Materials and methods

2.2.1 Materials

The following materials were used as received. 1,3-butanediol (13BD, 99%) was purchased from Acros Organics. 1,4-butanediol (14BD, 99%), propylene carbonate anhydrous (PC, 99.7%), dioctyl phthalate (DOP, 99%), fluorescein isothiocyanate isomer I (FITC, ≥90%), and tetraethyl orthosilicate (≥99.0%) were purchased from Sigma Aldrich. (3-aminopropyl) triethoxysilane (APTES, ≥98%) was purchased from TCI America. Submicron filtered water (HPLC grade) was purchased from Fisher Chemical. Hexamethyldisilazane (HMDS, 98+%) was purchased from Alfa Aesar. Strong ammonia hydroxide solution (27-

30%) was purchased from VWR. Anhydrous ethanol (200 proof) was purchased from Rossville Gold Shield.

2.2.2 Development of 14BD/PC bijels

The phase diagram for the 14BD/PC mixture was experimentally determined through a series of cloud point measurements at different compositions, using a custom-made apparatus reported in one of our previous papers.[39] Briefly, weighed amounts of 14BD and PC were added to a 7 mL optical glass cell (Hellma Analytics) with a 10 mm light path, and subsequently heated to 40°C and homogenized by stirring. The cell was then placed into the light path of a custom-made turbidity meter with a temperature probe attachment. A jacketed heat exchanger was used to lower the temperature of the sample at a cooling rate of approximately -0.5°C/min, while concurrently recording the transmitted light intensity and the temperature. We defined the cloud point as the temperature corresponding to a 5% drop in light intensity from the maximum. The 14BD/PC phase boundary was constructed by fitting a 3rd order Fourier series to the cloud point data, and the critical composition and temperature were numerically calculated from the maximum point on the fitted curve. The cloud points and phase boundaries obtained from these measurements are plotted in Fig. 2.1a. The interfacial tension ($\sigma_{\alpha\beta}$) of the 14BD/PC mixture was measured at different temperatures by using the pendant drop method on a tensiometer (Biolin Scientific Attension Theta) and is plotted as a function of temperature in Fig. 2.1b.
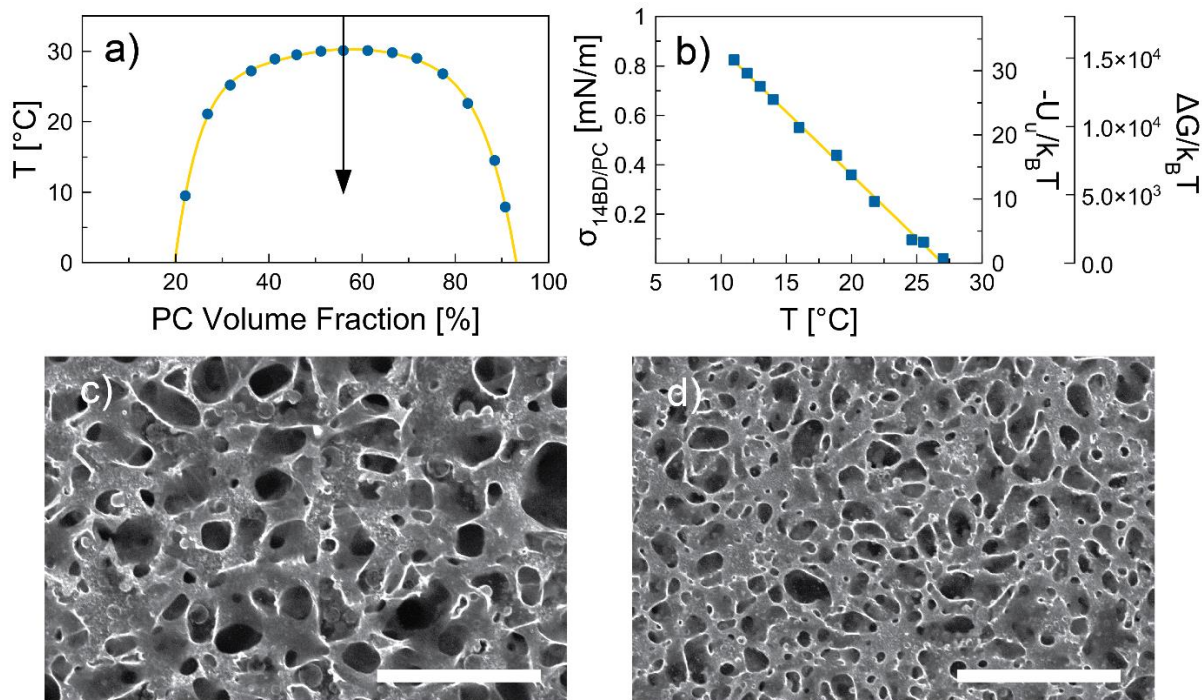
Fig. 2.1 Physical properties of the 14BD/PC mixture and the formation of 14BD/PC bijels. (a) Phase diagram for the 14BD/PC mixture. The blue circles are measured data, and the yellow line is the phase boundary derived from the Fourier fit. The arrow schematically indicates a quench at the critical composition (56.0 vol% PC). (b) The interfacial tension (left axis) of the 14BD/PC mixture measured (blue squares) at different temperatures. The corresponding detachment energy ($\Delta G/k_B T$) of an adsorbed 310 nm particle and the capillary potential ($-U_u/k_B T$) induced by contact line undulations are plotted on the right axes. The yellow line is a linear fit drawn to guide the eye. (c,d) CLSM images of 14BD/PC bijels prepared with ϕ_{SNP} = 7.5 × 10⁻³ and 1.5 × 10⁻², respectively. Scale bars = 200 μm.

We employed the well-known Stöber process and subsequent silanization of particle surfaces to synthesize monodispersed, fluorescently tagged, and neutrally wetting silica nanoparticles (SNPs) for stabilizing the 14BD/PC bijels.[10,21,23,40] In our experience, the ability to form mechanically stable bijels in the 14BD/PC system strongly depends on the wetting properties of the SNPs, which themselves are sensitive to external factors such as the local temperature and humidity during synthesis. In addition, these wetting properties gradually evolve over time regardless of the storage conditions (vacuum or low temperature), making the particles only usable for a few days after synthesis. Therefore, a fresh batch of neutrally

18

wetting SNPs had to be synthesized every 3 days during our studies, and the extent of silanization needed to produce neutrally wetting SNPs varied between these batches. To account for these variations, we set up six separate reactions simultaneously with different amounts of HDMS in each round of SNP synthesis and assessed particle wettability by their ability to form mechanically stable bijels.[21] First, a silane-coupled fluorescent dye solution was prepared by mixing 8.0 mg of FITC, 33.8 μL of APTES, and 6.4 mL of anhydrous ethanol together for 15 min. Then, in six separate 20 mL scintillation vials, a 1 mL aliquot of the dye solution, 8.8 g of anhydrous ethanol, 1.0 mL of water, 680 μL of tetraethyl orthosilicate, and 295 μL of strong ammonia solution were mixed by vortex mixing (Vortex Genie 2, Science Industries) and placed in a 4°C refrigerator. After 3 h, varying amounts of HMDS (150-200 μL, with 10 μL intervals) were added to the different reaction vials followed by vortex mixing for 15 s, and then allowed to react unperturbed in the refrigerator for an additional 18 h. Typically, one of the six reactions would produce neutrally wetting SNPs, while the others were either too hydrophobic or too hydrophilic to sustain mechanically stable bijels.[21] The resulting SNPs were subsequently washed by repeated centrifugation and resuspension in anhydrous ethanol and dried in a 110°C vacuum oven for 1 h. Scanning electron microscopy (SEM, FEI Magellan 400 XHR) was used to characterize the particle size (radius, a = 160 nm) and distribution (coefficient of variance, CV = 6.7%). A representative SEM micrograph is shown in Fig. S2.1.

The wetting properties of the SNPs were qualitatively assessed by imaging the samples on a confocal microscope after a temperature quench and testing for successful bijel formation. Here, the criteria for success include the formation of bicontinuous fluid domains (as opposed to solid-stabilized discrete droplets), as well as relative uniformity in the

domain size, as assessed by confocal microscopy imaging. To form the bijels, SNPs were first dispersed in a critical mixture of 14BD/PC using an ultrasonic horn (Sonifier 250, Branson Ultrasonics), which provided vigorous agitation and heating. After 30 s of sonication, the final temperature was approximately 50°C, and the dispersion was visually homogenous without any indications of particle aggregation or fluid interface formation. The dispersion was then transferred to a glass cuvette (400 μm ID, VitroCom) preheated to 50°C. Quenching into the 14BD/PC mixture's miscibility gap was achieved by placing the cuvette in direct contact with an aluminum heat sink at room temperature (~22°C). An inverted microscope (rheometer microscopy module, TA Instruments) coupled with a VT-Eye confocal scanner (VisiTech International), or a standalone Olympus Fluoview 3000 confocal laser scanning microscope (CLSM) was used to examine the internal microstructure of the bijels. Fig. 2.1c and 1d show CLSM (Olympus) images of 14BD/PC bijels formed with $\phi_{SNP} = 7.5 \times 10^{-3}$ and 1.5×10^{-2}, where ϕ_{SNP} denotes the volume fraction of SNPs.

2.2.3 Bijel rheology

The rheological measurements presented in this paper were conducted using a stress-controlled rheometer (ARG2, TA Instruments) equipped with a sandblasted, 40 mm diameter, 2° cone-and-plate geometry and a temperature-controlled bottom plate. To maintain consistency, an aliquot of the dispersion from every rheological experiment was also tested for successful bijel formation using CLSM imaging. Bijels were formed directly on the rheometer stage by transferring the homogenized dispersion to a preheated rheometer stage (36°C) and quenching it using the maximum cooling rate available (approx. -16°C/min). A 2 h long SAOS (at strain $\gamma = 1.0 \times 10^{-1}$ % and frequency $\omega = 6.3 \times 10^{-1}$ rad/s) test was applied to monitor the formation behavior during and after quenching. Oscillatory

amplitude sweep experiments were conducted by performing three oscillation cycles at a fixed frequency of $\omega = 6.3 \times 10^{-1}$ rad/s and strains spanning from $\gamma = 1.0 \times 10^{-2}$ % to 1.0×10^3 %. Since amplitude sweeps extend to large strains that plastically deform the microstructure of bijels,[25] each of these tests was conducted on a separate bijel. For small and medium amplitude oscillatory frequency sweeps, six separate tests were conducted in succession on one single bijel, at fixed strains of $\gamma = 1.0 \times 10^{-2}$ %, 1.0×10^{-1} %, 1.0%, 2.0%, 5.0%, and 10%, and frequencies ranging from $\omega = 6.3 \times 10^{-3}$ to 6.3×10^2 rad/s. The frequency sweeps at $\gamma = 1.0 \times 10^{-2}$ % and 1.0×10^{-1} % were conducted from low-to-high and high-to-low frequencies to demonstrate the repeatability of the linear viscoelastic response. For strains greater than $\gamma = 1.0 \times 10^{-1}$ %, we have occasionally observed sudden drops in both G' and G'' during oscillatory measurements, possibly due to microstructural breakdown of the bijel. It is possible that shearing at high rates promoted particle rearrangement or detachment, which, upon repeated cycles, cascaded into catastrophic microstructural failure.[41] Therefore, frequency sweeps at $\gamma > 1.0 \times 10^{-1}$ % were conducted only from low-to-high frequency.
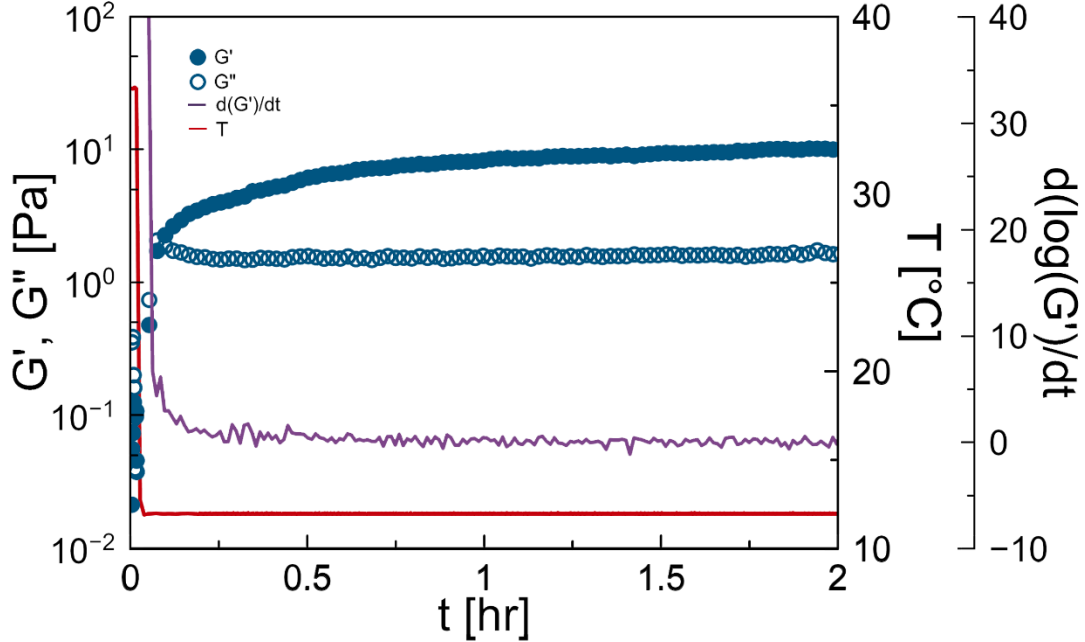
Fig. 2.2 Time evolution of G' (close symbols) and G'' (open symbols) following the formation of a 14BD/PC bijel with $\phi_{SNP} = 1.5 \times 10^{-2}$. The purple and red lines (plotted on the right axis) mark the derivative of $\log(G')$ with respective to time and the temperature quench from 36°C to 12°C.

2.2.4 Capillary suspension preparation

In our experience, the interfacial tension of the 14BD/PC mixture is too weak to sustain a sample spanning network of dense SNPs at low ϕ_{SNP} against gravitational forces. Therefore, capillary suspensions were formulated using polymethylmethacrylate (PMMA) microparticles grafted with poly-12-hydroxystearic-acid (PHSA) in a mixture of 13BD/DOP, whose interfacial tension, measured via the pendant drop method on a tensiometer is $\sigma_{13BD/DOP}$ = 5.26 mN/m at 12.0°C. Fluorescently tagged PHSA-PMMA particles were synthesized via established protocols.[42,43] In brief, 1.75 g of PHSA, 0.27 g of 2,2'-azobis-isobutyronitrile, 8.00 mg of Nile Red dye, 0.17 g of 1-octanethiol, 32.54 g of methyl methacrylate, and 0.67 g of methacrylic acid were mixed into 21.98 g of hexane and 10.98 g of dodecane, and reacted under full reflux for 2 h at 80°C to produce PMMA particles. Then 0.16 g of N,N-dimethylethanolamine dissolved in 21.98 g of dodecane was added to the

reaction flask and reacted for 12 h at 120°C to covalently bond the PHSA to the PMMA particles. The PHSA-PMMA particles were then washed through repeated centrifugation and resuspension in hexane. A sputter coater (EM ACE600, Lecia) was used to deposit a 4 nm layer of iridium onto the particle surface prior to SEM imaging. The resulting iridium-coated PMMA-PHSA particles had an average diameter of 1.05 μm and a CV of 2.1% (shown in Fig. S2.2). Capillary suspensions were prepared via a procedure similar to that outlined by Bossler and Koos.[44] In brief, 22.8 mg of DOP was dispersed in 769.8 mg of 13BD via ultrasonication by an ultrasonic horn for 60 s, which also raised the mixture temperature to approximately 50°C. Once the suspension naturally cooled back down to room temperature, 169.5 mg of dried PMMA-PHSA particles was added to yield ϕ_{PMMA} = 0.20, and subsequently dispersed using an ultrasonic horn. This sonification process was split into three repeated cycles of ~30 s of ultra-sonification and 2 min of resting to avoid overheating. For CLSM characterization, an oil solubilized fluorescent dye (10-5045, ACDelco) was added to the DOP fluid (1 vol% dye) as a tracer to enable imaging of the capillary bridges between the particles.

2.2.5 Capillary suspension rheology

To load the capillary suspension onto the rheometer, the sample was first transferred onto the rheometer bottom plate using a spatula, and then compressed by lowering the prechilled (12.0°C) measuring geometry (sandblasted, 40 mm diameter, 2° cone) to a gap height of 100 μm, which is 40 μm above the required measurement height. Since compression can cause microstructural changes in the suspension, a 500 s^{-1} pre-shear step was applied for 60 s before lowering the gap height to 60 μm. Then, the suspension was pre-sheared again at 100 s^{-1} for 60 s, and subsequently monitored for 10 h via SAOS (γ = 1.0 × 10^{-2} %, ω = 6.3 × 10^{-1} rad/s) while the particle network reformed. Oscillatory amplitude or

frequency sweeps were conducted following this formation-and-aging step. Oscillatory amplitude sweep experiments were conducted at a fixed frequency of $\omega = 6.3 \times 10^{-1}$ rad/s and strains spanning from $\gamma = 1.0 \times 10^{-3}$ % to 1.0×10^3 %. For frequency sweeps, strain amplitudes of $\gamma = 1.0 \times 10^{-2}$ %, 2.5×10^{-2} %, 4.0×10^{-2} %, and 1.0×10^{-1} % were selected based on the results of amplitude sweeps to span the linear viscoelastic region and the transition to non-linearity. Amplitude and frequency sweeps were conducted on separate samples since large strain deformation causes irreversible breakdown of the particle network.

2.3 Results and discussion

2.3.1 Characterization of 14BD/PC bijels

Fig. 2.1a summarizes the phase behavior of the 14BD/PC binary mixture. We recorded an UCST of 30.3°C and a critical composition of 56.0 vol% PC. It is worthwhile to mention that this fluid mixture exhibits a symmetric phase boundary centered near 50% volume fraction, which has been previously hypothesized as an important attribute for optimal bijel formation.[21] This symmetry allows for direct access from the single-phase into the spinodal region via a temperature quench as well as a near-equal volume split between the two phases.[21] Mechanical arrest of spinodal decomposition was made possible by incorporating neutrally wetting SNPs that were modified using the HMDS silanization method outlined in Materials and Methods. Fig. 2.1c-d display CLSM images of 14BD/PC bijels at two different values of ϕ_{SNP}, demonstrating its effect on the bijel characteristic domain size.

To monitor the formation and assess the mechanical stability of this new bijel system, 2-h long SAOS tests were conducted on samples comprising $\phi_{SNP} = 7.5 \times 10^{-3}$ and 1.5×10^{-2} at 21 and 12°C. An example of these tests is plotted in Fig. 2.2. In general, the formation of

14BD/PC bijels appears to have the rheological signatures of a gelation process with a sharp increase in both G' and G'' (which happens upon crossing the UCST of 30.3°C), and a prominent $G'>G''$ signal afterward. Following the formation is a slow aging process where G' gradually increases to its terminal value while G'' plateaus early on, akin to the behavior reported by Lee et al., Imperiali et al., and Bai et al.[18,22,23] These observations were consistent across all samples that were tested. Importantly, the results of Fig. 2.2 show that our bijels reach mechanical stability, manifested by a plateau in both G' and G'', in approximately 100 min, thus enabling the examination of the role of interparticle interactions in bijel stability after a 2 h waiting period. Separately, we monitored the microstructure of these bijels using CLSM for 2 h and did not observe any coarsening of the fluid domains during this aging period. The gradual rise in G' after bijel formation may therefore be related to localized particle rearrangements along the interface that do not amount to appreciable changes in the overall microstructure, a topic that will be discussed in later sections.

The near-steady state shear moduli of the 14BD/PC bijels were recorded at the end of the 2 h aging period and plotted in Fig. S2.3. Although we have only tested two ϕ_{SNP} and two temperatures, our rheology findings suggest a direct relationship between the shear moduli and ϕ_{SNP} or $\sigma_{14BD/PC}$, where stronger bijels can be formed with either a larger volume fraction of particles or higher interfacial tension, which is consistent with the observation made by Lee et al. on the rheology of W/L bijels.[18] Interestingly, the SAOS moduli of the 14BD/PC bijels are at least an order of magnitude weaker than the reported values for the W/L and polystyrene/polybutene (PS/PB) bijels stabilized with similar solid volume fractions.[18,23] This disparity is likely a result of the differences in interparticle attractions between different bijel systems. For instance, the W/L and PS/PB bijels are known to

transition to monogels, a concept first introduced by Sanz et al.,[45] where van der Waals interactions result in a particle network that can remain intact even if the fluids are remixed.[18,23] While the relationship between the shear moduli and van der Waals forces has not been fully explored, the transition to a monogel is a clear indicator for the presence of strong van der Waals attractions between the particles. Therefore, to examine the possible role of van der Waals interactions in our system, we formed a 14BD/PC bijel as described earlier, and after a 2 h waiting period, reheated it to above its UCST to allow remixing of the fluids. Fig. 2.3 shows confocal microscopy snapshots of this experiment, which confirm that the removal of interfacial tension results in complete re-dispersion of the particle network. Importantly, from this observation, we conclude that van der Waals forces are not responsible for the mechanical stability of 14BD/PC bijels.[18]
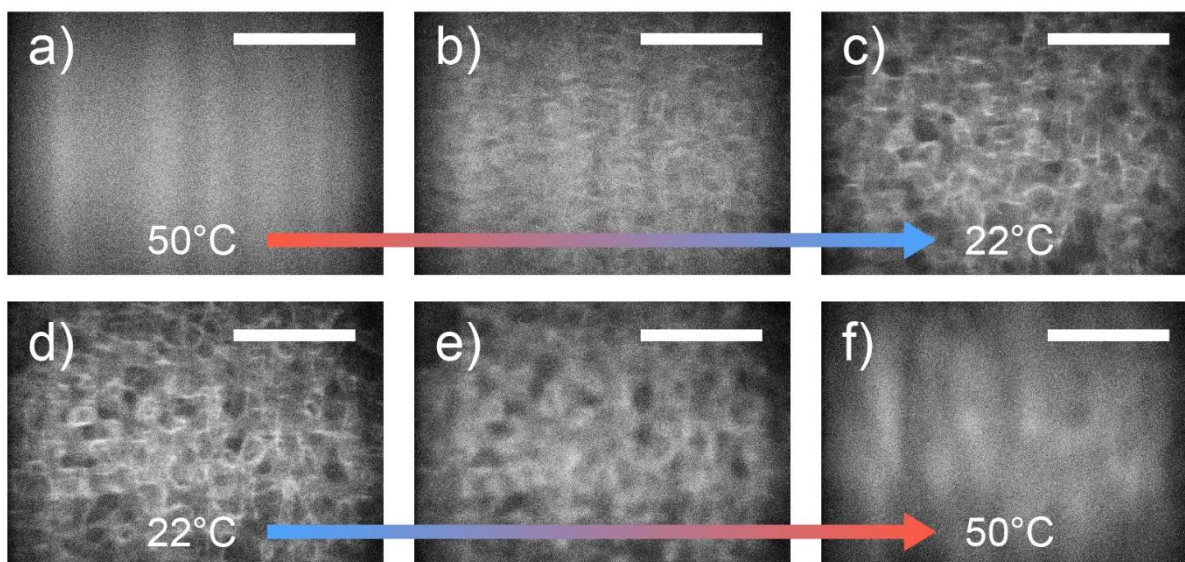
Fig. 2.3 CLSM (Vt-Eye, VisiTech International) snapshots of the formation and breakdown of a 14BD/PC bijel prepared with ϕ_{SNP} = 1.5 × 10⁻². (a-c) A dispersion of SNPs in a critical mixture of 14BD/PC was quenched from 50°C to 22°C. (d-f) After 2 h, the bijel was reheated from 22°C to 50°C. Scale bar = 100 μm.

Having ruled out van der Waals interactions as major contributors to mechanical stability in our system, we now focus on capillary forces between the particles. In bijels, particles may experience attractive capillary interactions through two different mechanisms. First, sequestration of a spherical particle at an interface with negative Gaussian curvature induces quadrupolar deformation to the interface, which in turn promotes attractive capillary interactions between neighboring particles.[46] For a particle with a 90° contact angle, the pair potential for such interactions can be approximated as $U_q = \sigma_{\alpha\beta} c^2 a^4$, where c is the radius of curvature.[38] In this study, ϕ_{SNP} = 7.5 × 10⁻³ and 1.5 × 10⁻² correspond to average domain sizes of 51.9 and 24.4 μm, respectively, as measured by CLSM imaging. The combination of nm-sized SNPs, weak interfacial tension, and μm-sized domains provide negligible capillary potentials on the order of 10^{-3} k_BT (see Fig. S2.4). Second, and more importantly, topological and chemical heterogeneities on the particle surface can cause undulations in the fluid-particle-fluid contact line, resulting in irregular distortions of the interface in the particle's vicinity, which in turn can cause strong capillary attractions between nearest neighbors.[47] Here, we approximated the deformation due to contact line undulation as quadrupoles and calculated the attraction potential following the formulation derived by Kralchevsky et al.: $U_u = -0.48(\pi\sigma_{\alpha\beta}H^2)$, where H is the undulation amplitude.[48] We asserted an overestimation of H = 10 nm, and computed attraction energy spanning a few to tens of k_BT (see Fig. 2.1b) for particles in contact. Note that this calculation provides an upper bound for the capillary potential because of the overestimated value of H, and the assumption of particles being in contact, which is not the case in the 14BD/PC bijels, given that particles are decorated with a steric layer of trimethylsilyl groups,[49] and that monogels do not form.[23] These approximations suggest that the capillary attractions in 14BD/PC bijels

are weak and that long-lasting interparticle bonds are unlikely, which are consistent with the weak shear moduli measured in our experiments. To place the values of U_u in better context, in Fig. 2.1b we also plot the energy required to detach a particle from the interface, $\Delta G = \pi a^2 \sigma_{\alpha\beta}(1 - |cos\theta|)^2$, where θ is the three-phase contact angle.[6] A quick comparison between the magnitudes of U_u and ΔG suggests that, while particle movements perpendicular to the interface involve a heavy energetic penalty, rearrangements along the interface are much more freely allowed. This rudimentary assessment suggests that bijels may be well described as 2D colloidal glasses, a conjecture that we will return to in more detail in later sections.

2.3.2 Linear rheology of 14BD/PC bijels

To further investigate the possible role of attractive capillary interactions in our system, we conducted small amplitude frequency sweep experiments at two different colloid volume fractions (modulating the interfacial curvature),[2] and temperatures (modulating the interfacial tension). The results for ϕ_{SNP} = 7.5 × 10⁻³ at the two temperatures studied are plotted in Fig. 2.4, and are representative of the overall behavior for both colloid volume fractions (see Fig. S2.5 ϕ_{SNP} = 1.5 × 10⁻²). In all cases, we observe a soft-glassy-like response where G' is nearly independent of frequency and G'' is marked by a prominent minimum near 1.0 × 10⁻¹ rad/s.[22] This behavior typically signifies an interplay between distinct fast and slow relaxation mechanisms in an arrested system, and has been observed in colloidal glasses,[50] weak colloidal gels,[51] concentrated emulsions,[52,53] and even polymers and surfactant systems.[54–56] In bijels, the fast and slow relaxation dynamics can be conceptualized as follows. On short time scales, localized thermal motions of a particle rattling against its nearest neighbors rapidly shear the fluids in the particle's vicinity and

induce lubrication stresses.[57] Over long periods, such fluctuations can create occasional transitory gaps within the particle network by chance, allowing particles to exchange neighbors or escape cages formed by nearby particles and relax stressed particle cages.[58] Hence, in both high and low frequency regimes, there are noticeable increases in G''. This framework also explains the slow aging dynamics that were observed following the formation of 14BD/PC bijels in Fig. 2.2. Following the initial jamming transition, the minimization of surface area by interfacial tension gradually drives the particle network toward a higher packing state through slow particle rearrangements. These gradual transition toward more tightly packed cages results in a gradual increase in G' over time.[59]

In this context, our explanation of bijel rheology as seen in Fig. 2.4 is reminiscent of colloidal glasses where the frequency scalings of G' and G'' are attributed to the localized Brownian dynamics of caged particles.[60,61] Therefore, to quantify our observations, we propose the use of a rheological model that was derived from Mode-Coupling Theory (MCT) by Mason and Weitz, which incorporates the α (slow, out of cage rearrangement) and β (fast, in-cage rattling) dynamics of a dense colloidal suspension to describe the frequency scaling of G' and G'' as follows:[60]

$$G'(\omega) = G_p + G_\sigma \left[\Gamma(1-a')cos\left(\frac{\pi a'}{2}\right)(\omega t_\sigma)^{a'} - B\Gamma(1+b')cos\left(\frac{\pi b'}{2}\right)(\omega t_\sigma)^{-b'} \right] + G_D(\omega),$$

$$G''(\omega) = G_\sigma \left[\Gamma(1-a')sin\left(\frac{\pi a'}{2}\right)(\omega t_\sigma)^{a'} + B\Gamma(1+b')sin\left(\frac{\pi b'}{2}\right)(\omega t_\sigma)^{-b'} \right] + G_D(\omega) + \eta_\infty \omega,$$

where G_p is the plateau modulus, t_σ is the β-relaxation time, G_σ is the viscoelastic amplitude, G_D is the high frequency modulus, and η_∞ is the high frequency suspension viscosity. a' and b' are critical exponents that are associated with the relaxation time scales and B is the scaling constant in the von Schweidler law.[62] These are predicted by MCT for hard spheres

as: a' = 0.301, b' = 0.545, and B = 0.963. Here, we employed the same parameters as 3D hard

sphere glasses since interfacially trapped colloids exhibit in-plane, 2D random walks similar

to Brownian motions in 3D,[63] and that previous applications of MCT to 2D systems have

revealed similar glass transition features as those in 3D.[64] The equations above were fitted

to our data treating the parameters G_p, G_σ, t_σ, G_D, and η_∞ as adjustable, and the results are

overlaid in Fig. 2.4. Overall, this adaptation of MCT captured the essential features of the

rheology of bijels, enabling a quantitative assessment of whether the relaxation dynamics of

our system are affected by interfacial tension. In Table 1 we report two important

parameters extracted from fitting the Mason-Weitz adaptation of MCT to our data: G_p, which

describes the magnitude of the G' plateau, and the frequency at which G'' reaches a minimum

$(\omega @ G''_{min})$.
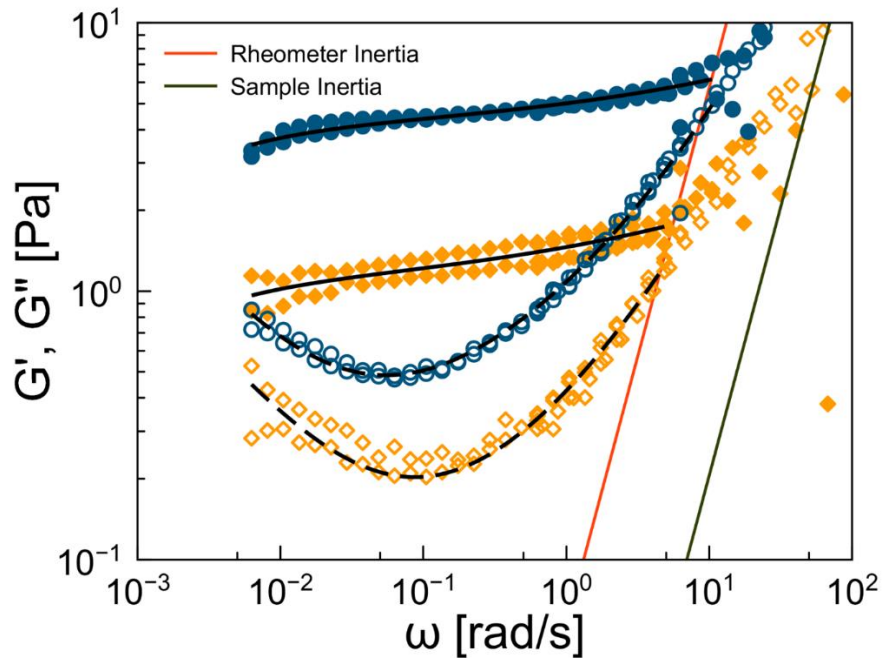
Fig. 2.4 Frequency response of 14BD/PC bijels comprising ϕ_{SNP} = 7.5 × 10⁻³ at T = 12 (blue) and 21°C (orange). G' and G'' are marked by open and close symbols, respectively. The solid and dashed lines represent the MCT fits. The red and green lines indicate the rheometer and sample inertia limit, respectively.[65]

Table 2.1 Fitted parameters from the MCT model for 14BD/PC bijels at different values of ϕ_{SNP} and T. The values for G_p were obtained directly from MCT fits. The frequencies corresponding to the G'' minimum were numerically calculated from the global minimum of the reconstructed $G''(\omega)$ using the MCT fitting parameters.

Volume Fraction (ϕ_{SNP}) and Temperature (T)	G_p [Pa]	ω @ G''_{min} [rad/s]
$\phi_{SNP} = 7.5 \times 10^{-3}$ $T = 12°C$	4.16	5.53×10^{-2}
$\phi_{SNP} = 7.5 \times 10^{-3}$ $T = 21°C$	1.05	8.73×10^{-2}
$\phi_{SNP} = 1.5 \times 10^{-2}$ $T = 12°C$	6.31	1.54×10^{-1}
$\phi_{SNP} = 1.5 \times 10^{-2}$ $T = 21°C$	2.68	8.83×10^{-2}

If attractive interparticle interactions were responsible for the viscoelasticity of bijels, one would expect that an increase in interfacial tension would lead to further arrest of particles and suppression of their slow relaxation dynamics, which would manifest as a shift in the location of G''_{min} to lower frequencies, together with an increase in G'. In an earlier study of this concept, Bergenholt et al. expanded MCT to dilute and attractive colloidal gels and demonstrated an ergodicity breaking transition prompted by interparticle attractions in the ranges of a few $k_B T$.[66] Importantly, their model predicted that the long-time structural decay and the shear moduli exhibit a relaxation time scale that depends on the interaction strength. In other words, a shift in the α relaxation timescale is expected at different attraction potential strengths. Similarly, a shift in the α-relaxation time scale and the location of G''_{min} was observed in colloidal suspensions as particle concentration approaches the glassy limit.[50] Yet, as seen in Fig. 2.4 and Table 2.1, G'' expressed a minimum at approximately the same frequency at both values of T (or $\sigma_{\alpha\beta}$) in our bijels, indicating that the α-relaxation timescales are unaffected by interfacial tension. Together with the remixing results shown in Fig. 2.3, this important observation further corroborates our proposition that attractive

interparticle interactions are not responsible for the viscoelasticity of 14BD/PC bijels, and are not required for their mechanical stability. Our explanation for the rises in G' and G'' with $\sigma_{\alpha\beta}$ is that a larger $\sigma_{\alpha\beta}$ would provide greater resistance to shear-induced dilation of the tightly packed interface. More specifically, the viscoelasticity of the interface in bijels stems from the packing of the particles on the interface,[67] whose surface coverage is capped at the jamming limit regardless of the strength of $\sigma_{\alpha\beta}$. At larger $\sigma_{\alpha\beta}$, a larger shear force is needed to stretch the interfaces between the particles, hence the shear moduli are larger. The findings presented in this section suggest that the rheology of bijels in the linear viscoelasticity regime is consistent with that of a jammed particle monolayer without significant attractive interactions, and therefore bijels can generally be viewed as 2D colloidal glasses weaving in 3D space. To provide further evidence for this conjecture, in the next section we compare the rheology of our bijels beyond their limit of linear viscoelasticity to a dilute colloidal gel in which attractive capillary interactions are necessary for stability, and demonstrate qualitative differences between the two.

2.3.3 Beyond linear viscoelasticity: comparison to an attractive system

As a representative example of a dispersion in which capillary interactions are necessary for mechanical stability, we prepared a capillary suspension made of colloidal PMMA particles, 1,3-butanediol (13BD), and dioctyl phthalate (DOP) as the continuous and secondary (bridging) liquid phases, respectively. As demonstrated first by Koos and Willenbacher, including a small amount of a secondary wetting fluid (here DOP) in a suspension can result in particle aggregation due to capillary pendular bridges, and the formation of a sample-spanning particle network.[44,68] Fig. 2.5 shows a confocal microscopy image of a capillary suspension at ϕ_{PMMA} = 0.20, ϕ_{13BD} = 0.62, and ϕ_{DOP} = 0.08, demonstrating

the tenuous particle network held together by pendular capillary bridges of DOP in a continuous 13BD phase.
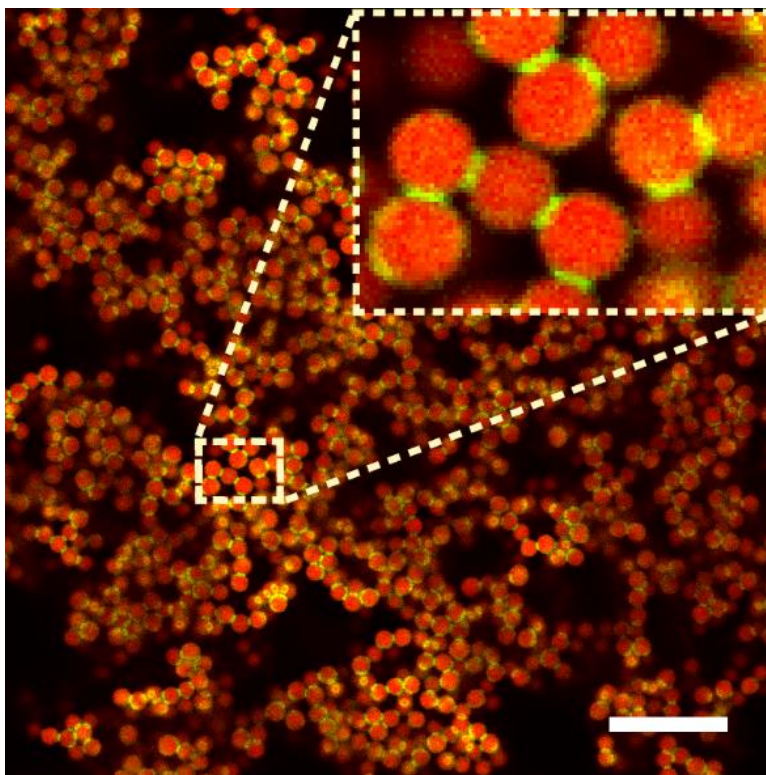
Fig. 2.5 CLSM image of a capillary suspension prepared with ϕ_{PMMA} = 0.20. The particles are loaded with Nile Red fluorescent dye and shown in red, and the secondary fluid that forms the pendular bridges is loaded with a green fluorescent dye (see methods) and colorized in green. Inset shows a magnified view (5x) of the suspension. Scale bar = 10 μm.

Here ϕ denotes a volume fraction, with the subscript specifying the species. This section will compare the rheology of such a system to our bijels, especially beyond their limit of linear viscoelasticity. We chose this regime because in dilute gels, shear deformation beyond the linear limit typically results in dramatic microstructural, and consequent rheological, changes in a narrow range of strain amplitudes. This behavior is unlike colloidal glasses, where yielding is typically a more gradual event involving changes in the identity of nearest neighbors through cage breaking, without noticeable transformations in the overall microstructure. These distinct features will enable us to further explore signatures of glass-

like or gel-like rheological behavior in bijels. To locate the limit of linear viscoelasticity, oscillatory amplitude sweeps were conducted on each system. Fig. 2.6a-c display the results for bijels at T = 12°C and two different values of ϕ_{SNP} (for a complete set of data on bijels, please see Fig. S2.6), and the capillary suspension at T = 12°C. For bijels, the linear viscoelastic region resides at γ < 0.1%. A gradual transition to non-linearity is observed past this region, where G' slowly drops, eventually resulting in a crossover between G' and G''. Beyond the crossover point, both G' and G'' appear to follow power law scaling with respect to γ, with exponent $n \approx$ -3/4. Macmillan, et al. reported irreversible breakdown of the bicontinuous structure of bijels formed by direct mixing at large strains.[25] It is likely that bijels formed through spinodal decomposition experience the same microstructural changes at or near the G'-G'' crossover. For capillary suspensions, the linear viscoelastic regime extends only to $\gamma \approx$ 0.05%, and the transition to non-linearity is marked by a sharp decline in both G' and G'' with a power-law exponent of $n \approx$ -1. The local power-law exponents of $G'(\gamma)$, calculated as $n(\gamma)$ = d(log(G'))/d(log(γ)) from the complete set of strain sweep data in Figs. S2.6 and 2.6c are plotted in Fig. 2.6d to quantify the abruptness of the linear to nonlinear transition between the two systems. Although both materials are stabilized by interfacial tension, the role of the interface and its impact on rheology vary dramatically between them. In bijels, shear deformation results in an overall dilation of the particle-laden interface, subsequently reducing the interfacial coverage and loosening the particle network.[69] These events do not result in catastrophic microstructural changes. Instead, the particles remain irreversibly sequestered at the interface, with interfacial tension continuously re-compressing them toward other jammed configurations, provided that the interface remains continuous. As such, the transition to nonlinear viscoelasticity in bijels is a gradual process

involving local particle rearrangements along the dilated interface, possible shear-induced reorientation of the fluid domains,[24] and re-jamming of particles into configurations that may slightly differ from the original undeformed state, rendering a small portion of the applied strain unrecoverable. Unlike bijels, however, the limit of linear viscoelasticity in capillary suspensions is determined by the stability of their pendular liquid bridges which form a sample spanning network.[70] At $\gamma > 0.05\%$, shear deformation can stretch and pinch off the pendular bridges and release the particles from their capillary traps.[70] Since particles are not localized to a restorative, continuous interface like bijels, such local bond breakages can result in dramatic changes to the microstructure, loss of sample-spanning paths along the particle network, and a precipitous drop in the mixture's viscoelastic moduli. In this qualitative comparison, our results point to clear distinctions between bijels and suspensions with attractive interparticle capillary forces, here in the context of their transition to nonlinear viscoelasticity and yielding.
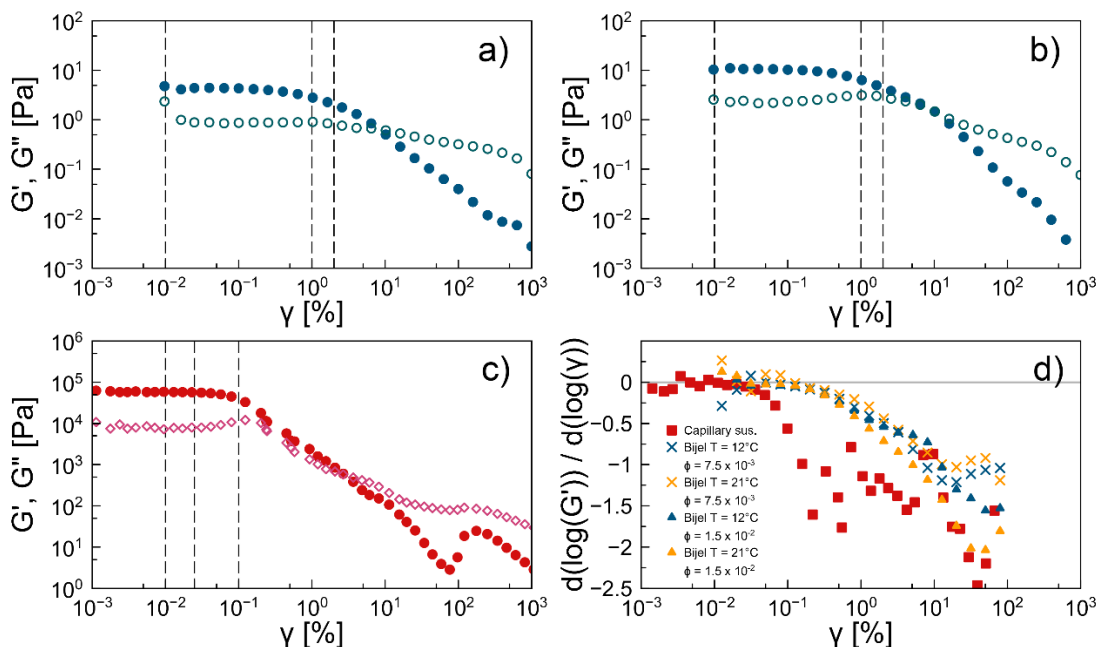
Fig. 2.6 Oscillatory amplitude sweeps showcasing the transition of G' (close symbols) and G'' (open symbols) from linear to non-linear viscoelasticity in 14BD/PC bijels (a-b) and 13BD/DOP capillary suspensions (c). Bijels were prepared with $\phi_{SNP} = 7.5 \times 10^{-3}$ (a) and 1.5×10^{-2} (b), and the capillary suspension was prepared with $\phi_{PMMA} = 0.20$. The dashed lines correspond to the strain amplitudes of the oscillatory frequency sweeps in Fig. 2.7. (d) Local power-law exponent $n(\gamma)$ (see text for detail) of $G'(\gamma)$ for bijels and the capillary suspension.

To further examine the transition to nonlinear viscoelasticity in bijels and capillary suspensions, we performed a series of frequency sweep experiments at different strain amplitudes on each system. The selected strain amplitudes for these tests are marked by dashed lines in Fig. 2.6, including one baseline test in the linear regime ($\gamma = 0.01\%$ for both systems), one test near the crossover point between G' and G'' ($\gamma = 5\%$ for bijels, $\gamma = 0.1\%$ for the capillary suspension), and an intermediate value to help elucidate the nature of the transition toward yielding ($\gamma = 1\%$ for bijels, $\gamma = 0.025\%$ for the capillary suspension). A subset of the frequency sweep results is shown in Fig. 2.7 (see Fig. S2.7-8 for the complete data set). All bijel results share an intriguing phenomenon where the G'' valley discussed earlier (recall Fig. 2.4) gradually disappears as the strain amplitude is increased. The overall

values of G' also drop as the strain amplitude is increased, but their frequency dependence remains flat. Frequency sweep experiments on bijels examine a rich interplay among several dynamic processes with different timescales, especially at intermediate strain amplitudes where shear deformation can reduce the particle surface coverage. The response is therefore rich and non-trivial. Nevertheless, we believe that the results of Fig. 2.7 provide important clues that corroborate the representation of bijels as 2D colloidal glasses weaving in 3D. We explain these results with a focus on the dynamics of particle cage relaxation and re-jamming along the interface. There are likely two phenomena occurring under shear deformation: (1) dilation of the particle-laden interface results in the formation of excess interfacial area and a lower interfacial coverage,[71] effectively dissolving the particles cages to dissipate shear energy, (2) local bending or shearing of the interface forcibly breaks open particle cages,[69] consequently melting the 2D glass network akin to shear-induced melting of a 3D colloidal glass.[70] Unlike colloidal glasses, however, the disruption to the particles cages is simultaneously accompanied by re-compaction by interfacial tension, which increases the surface coverage. At low shear frequencies and large strain amplitudes, the particle network is continually disrupted and loosened by shear, and re-jammed into new mechanically arrested states by interfacial tension. Since cages are persistently being fluidized and rejuvenated, α relaxation is overwritten by shear-induced cage breaking, resulting in a gradual disappearance of the low-frequency rise in G'' that was discussed in Fig. 2.4. In other words, because shear deformation dilates the interface, out of cage movement is no longer limited to the exceedingly large timescales associated with α relaxation, and can instead occur on the oscillation timescale. In the high frequency and intermediate strain limit, the interface cannot recoil fast enough for the particles to continuously re-jam by interfacial

tension. However, particles remain in proximity and experience local interparticle hydrodynamics interactions caused by ballistic motions of particles barraging against nearby neighbors, giving rise to high frequency responses similar to β dynamics. Therefore, we interpret the gradual disappearance of the G'' valley at intermediate strains to be associated with shear-induced melting and re-jamming of a 2D colloidal glass that is weaving in 3D. Importantly, our results also indicate that the restorative nature of the continuous interface within bijels provides them with incredible ductility and even self-healing characteristics, a unique attribute that may be exploited for technological applications.

These rheological responses are vastly different in the case of capillary suspensions. In the linear viscoelastic limit, Both G' and G'' appear to follow a mild power law scaling with respect to ω, and no G'' minimum is observed. Therefore, even in the linear regime, the capillary suspensions do not exhibit the same time-dependent relaxation dynamics as bijels. For these colloidal suspensions stabilized by capillary bridges, the strength of attraction due to the capillary force can be approximated as: $F_c = 2\pi a \sigma_{13BD/DOP} cos\theta \approx 16 \, nN$.[68] This strong attraction results in a large elastic modulus as seen in Fig. 2.7g, and also overcomes Brownian forces to lock the particles in their initial arrested configuration. As such, α and β dynamics are suppressed, resulting in a featureless G'' response. Notably, comparing these results to bijel rheology (Fig. 2.7a, d, and g) establishes the consequential effects of α and β suppression, which further support our assertion that strong attractions are not present within 14BD/PC bijels, and they are not a requirement for viscoelasticity or stability in bijels. Furthermore, unlike bijels, increasing the strain amplitude ($\gamma = 0.025\%$, Fig. 2.7h) did not change the response in the capillary suspension, but a further increase to near the nonlinear regime ($\gamma = 0.1\%$, Fig. 2.7i) resulted in dramatic changes where the sweep-up and sweep-

down experiments resulted in vastly different responses, likely due to microstructural collapse and breakup of the particle network. This failure mode is consistent with our strain sweep experiments (Fig. 2.6), which suggested a brittle response in capillary suspensions, due to their short interparticle bonds and the lack of a continuous interface, like that in bijels, to impart them with self-healing characteristics.
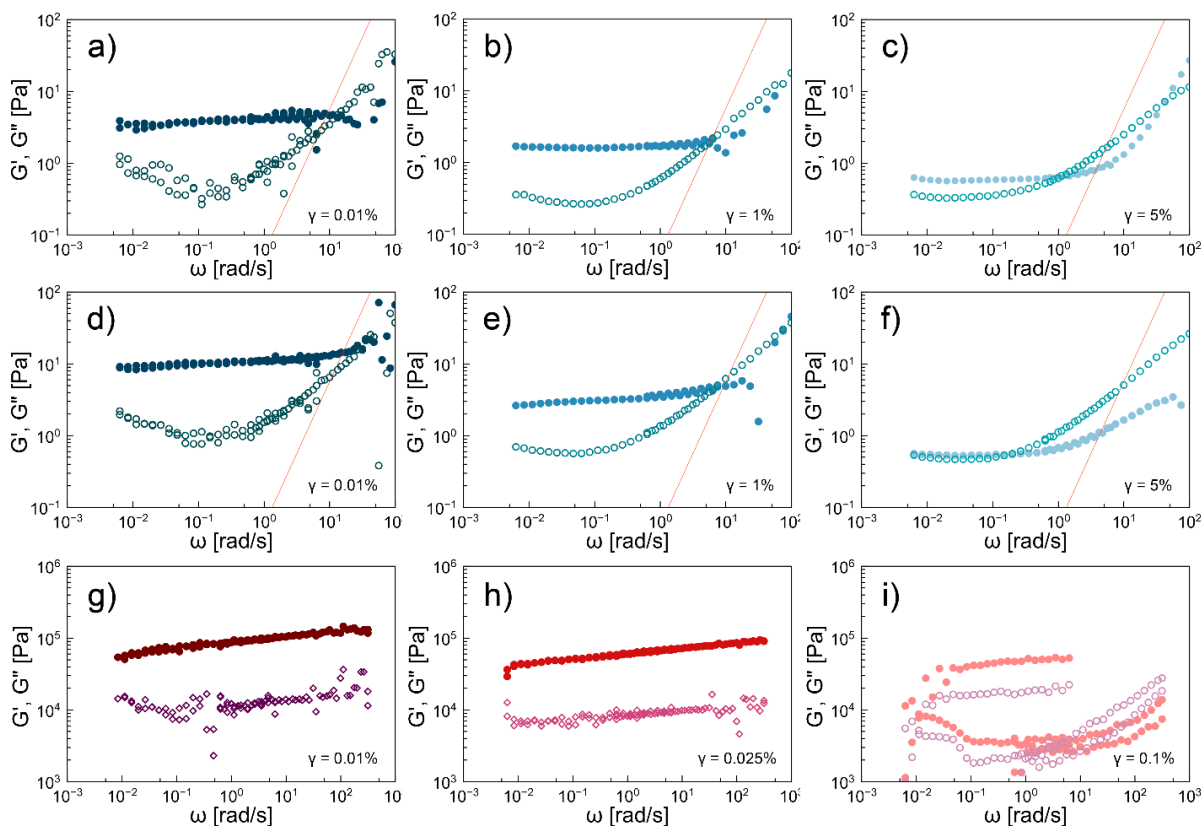
Fig. 2.7 Frequency response of 14BD/PC bijels (a-f) comprising ϕ_{SNP} = 7.5 × 10⁻³ (a-c) and 1.5 × 10⁻² (d-f), and 13BD/DOP capillary suspensions (g-i) comprising ϕ_{PMMA} = 0.20 at small and medium strains. G' and G'' are marked by open and close symbols, respectively. The strain amplitude increases from left to right in each row.

2.4 Conclusion

The nature of interparticle interactions in bijels and the possible necessity of attractive forces for bijel stability were investigated through remixing as well as linear and nonlinear rheological measurements. We ruled out van der Waals forces by performing fluid

remixing experiments and used temperature and particle volume fraction as means to modulate the interfacial tension and curvature, in turn tuning the strength of capillary interactions within mechanically stable 14BD/PC bijels. Our linear rheology experiments revealed signatures of long- and short-time relaxation timescales that are invariable to increasing capillary interaction strength, reminiscent of Brownian-driven in-cage (β) and out-of-cage (α) dynamics in colloidal glasses. Nonlinear rheology experiments revealed signatures of cage relaxation and unjammed dynamics at intermediate strains, which we contributed to shear-induced dilation of the continuous interface facilitating in-plane particle rearrangements. Our results also demonstrated remarkable ductility in bijels owing to the strong adsorption of particles to the continuous interface and its regenerative nature, which can continuously re-compress the particles into new jammed configurations. These results were qualitatively compared to a capillary suspension as a representative system in which attractive interactions are necessary for stability. The capillary suspension showed suppression of α and β dynamics, which we attributed to strong interparticle attractions, along with loss of ductility due to the non-restorative nature of the particle network. Our results indicate that attractive interparticle interactions are not required for stability or responsible for viscoelasticity in bijels, and interfacial jamming alone is sufficient to produce a mechanically stable 2D colloidal glass that percolates in 3D. In addition, our findings provide new insights into the dynamics of particles jammed along fluid interfaces, which have important implications in the design of bijel-derived functional materials and the mechanics of the broader class of solid-stabilized mixtures such as Pickering emulsions.

2.5 Supporting information
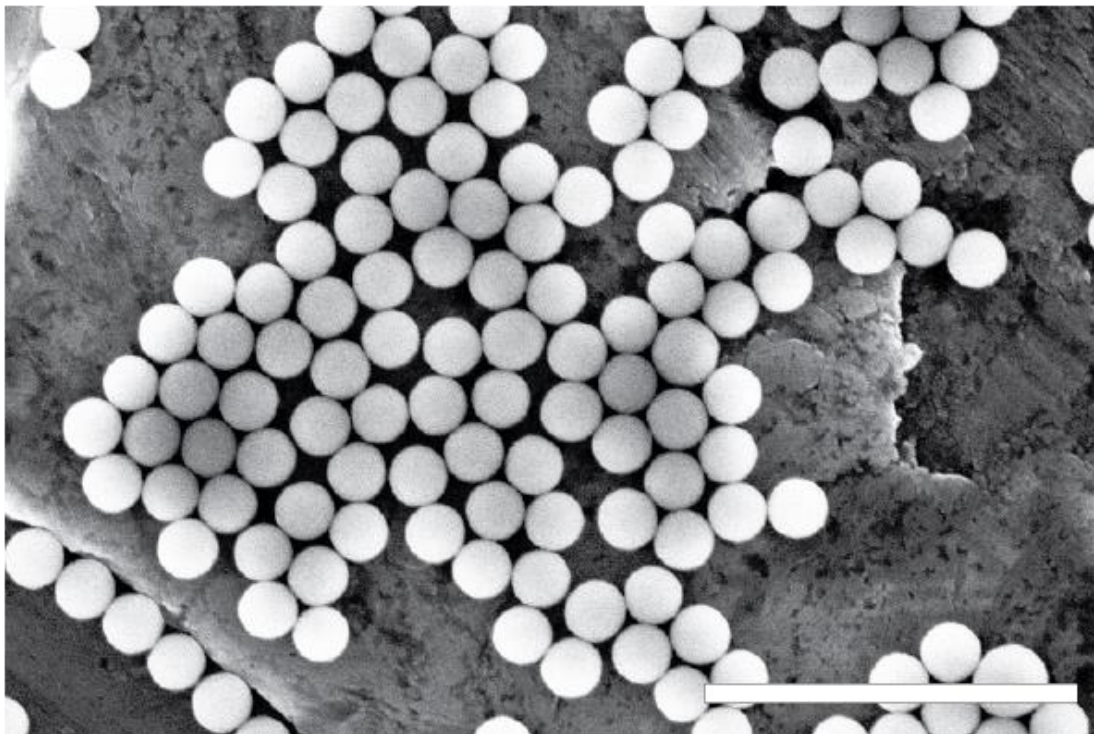
Fig. S2.1 A SEM micrograph of the SNPs used in the preparation of 14BD/PC bijels. Scale bar = 2 μm.
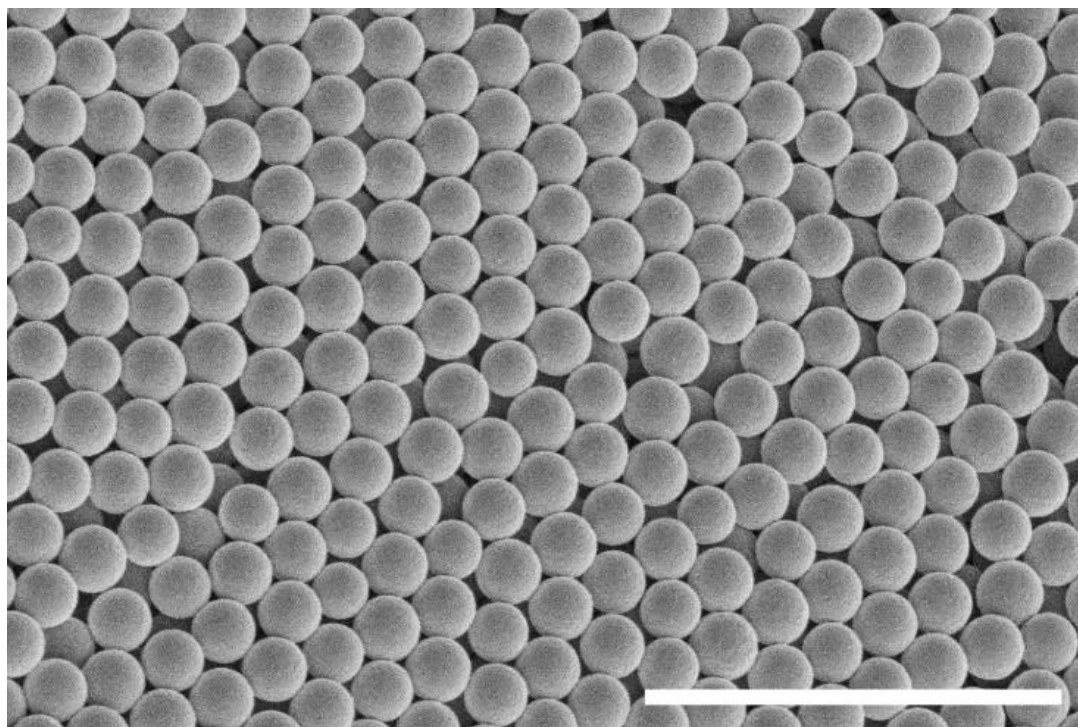
Fig. S2.2 A SEM micrograph of the PHSA-PMMA particles used in the preparation of 13BD/DOP capillary suspensions. Scale bar = 10 μm.
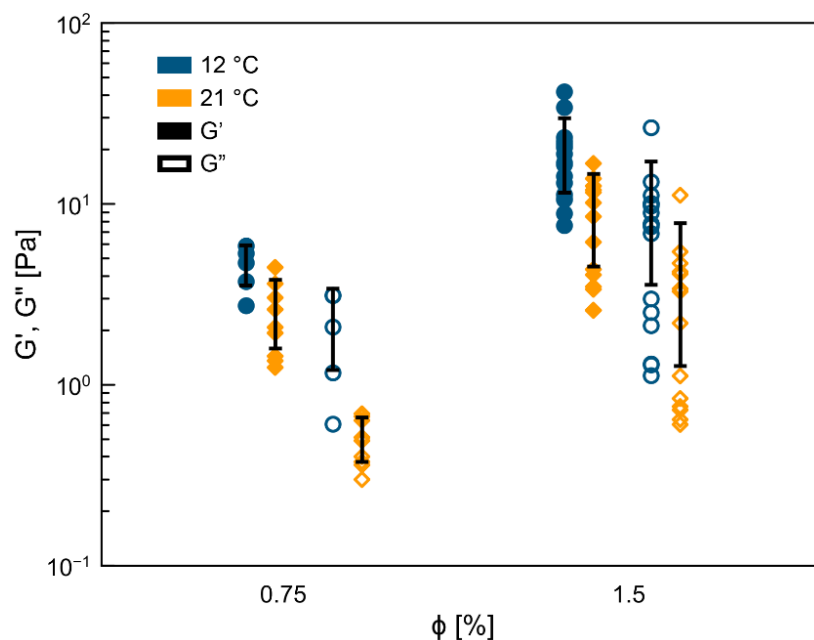
Fig. S2.3 Near-steady state G' (close symbols) and G'' (open symbols) of 14BD/PC bijels with ϕ_{SNP} = 7.5×10^{-3} and 1.5×10^{-2} at 12°C (orange) and 21°C (blue). The samples were measured at $\gamma = 1.0 \times 10^{-1}$ % strain and frequency $\omega = 6.3 \times 10^{-1}$ rad/s after a 2 h long aging period. Error bars represent the relative error (N ≥ 5).
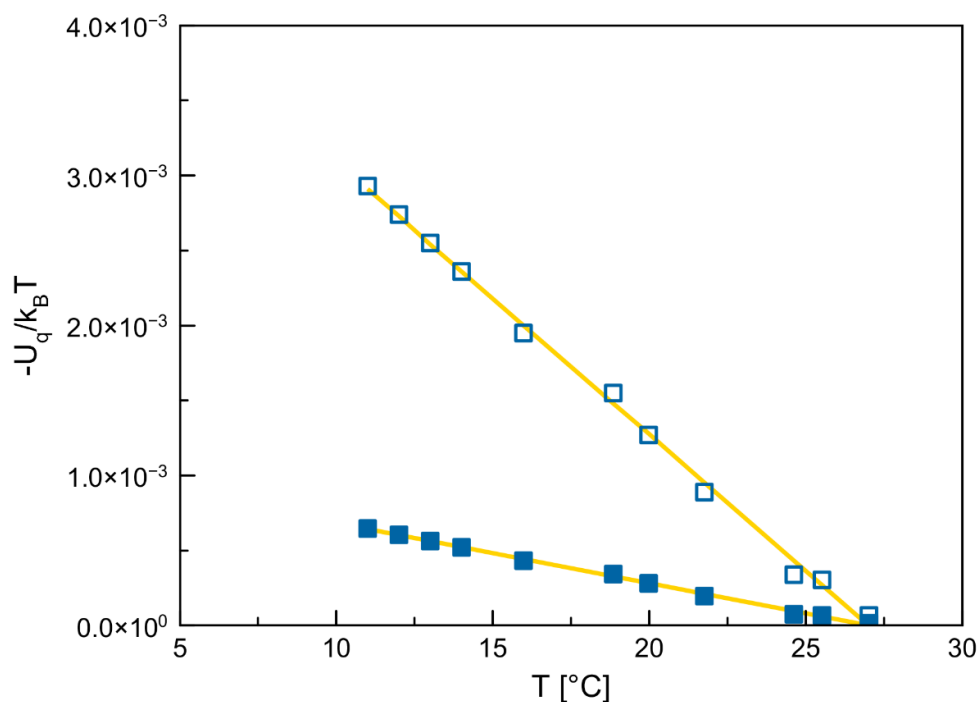
Fig. S2.4 Capillary pair-potential (U_q) induced by local quadrupolar deformation of an interface with negative Gaussian curvature, plotted as a function of temperature for 14BD/PC bijels comprising ϕ_{SNP} = 7.5×10^{-3} (close symbols) and 1.5×10^{-2} (open symbols). The blue markers present values calculated from the interfacial tension measurements, and the yellow lines are linear fits.
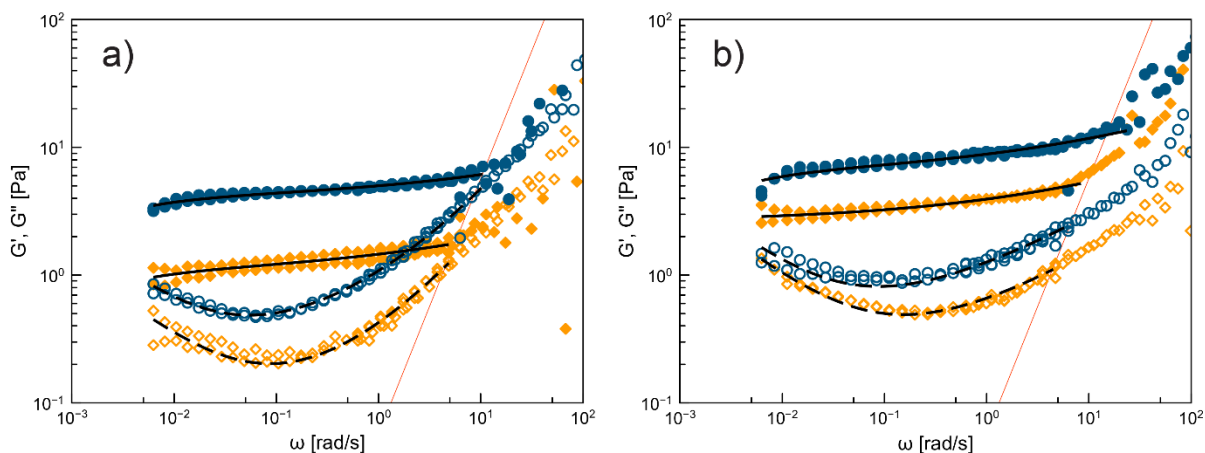
Fig. S2.5 Frequency response of 14BD/PC bijels comprising ϕ_{SNP} = 7.5 × 10⁻³ (a) and 1.5 × 10⁻² (b) at T = 12 (blue) and 21°C (orange). G' and G'' are marked by open and close symbols, respectively. The solid and dashed lines represent the MCT fits. The red lines indicate the rheometer inertia limit.
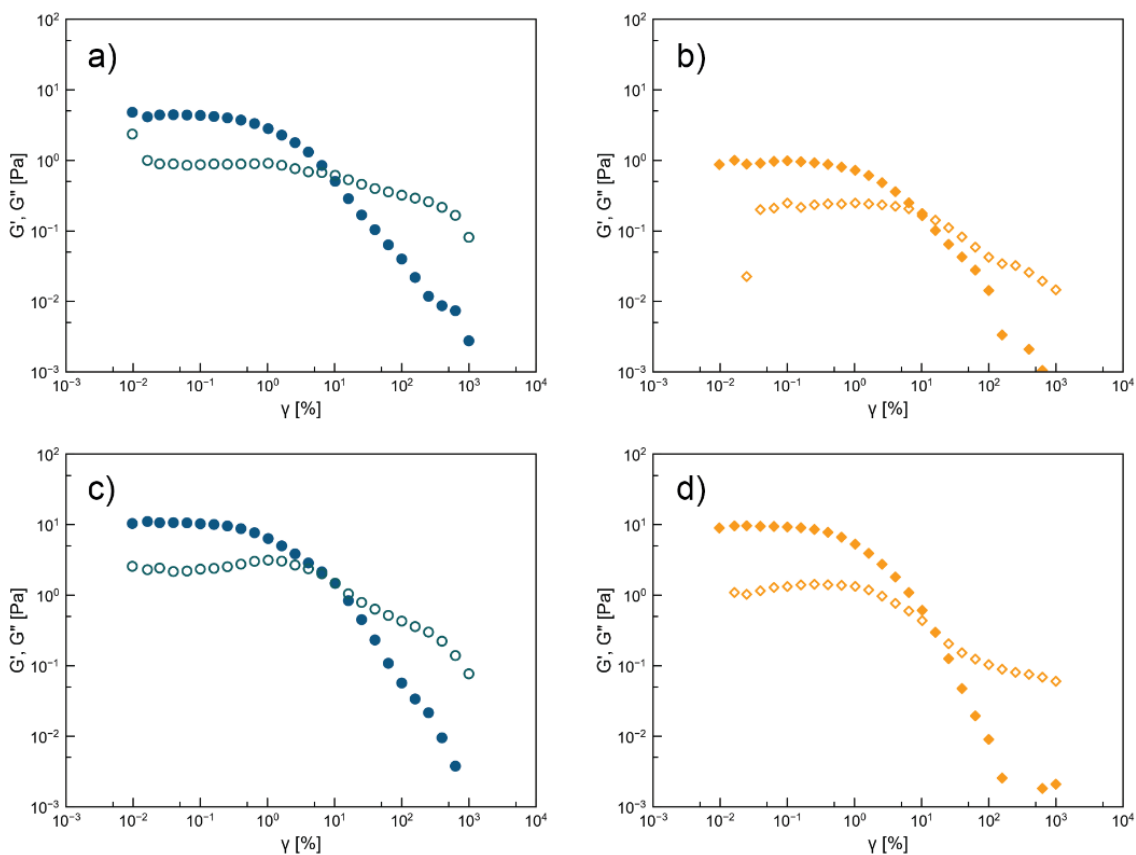
Fig. S2.6 Oscillatory amplitude sweeps showcasing the transition of G' (open symbols) and G'' (close symbols) from linear to non-linear viscoelasticity for 14BD/PC bijels comprising ϕ_{SNP} = 7.5 × 10⁻³ (a, b) and 1.5 × 10⁻² (c, d). The blue and orange symbols represent measurements conducted at T = 12 and 21°C, respectively.
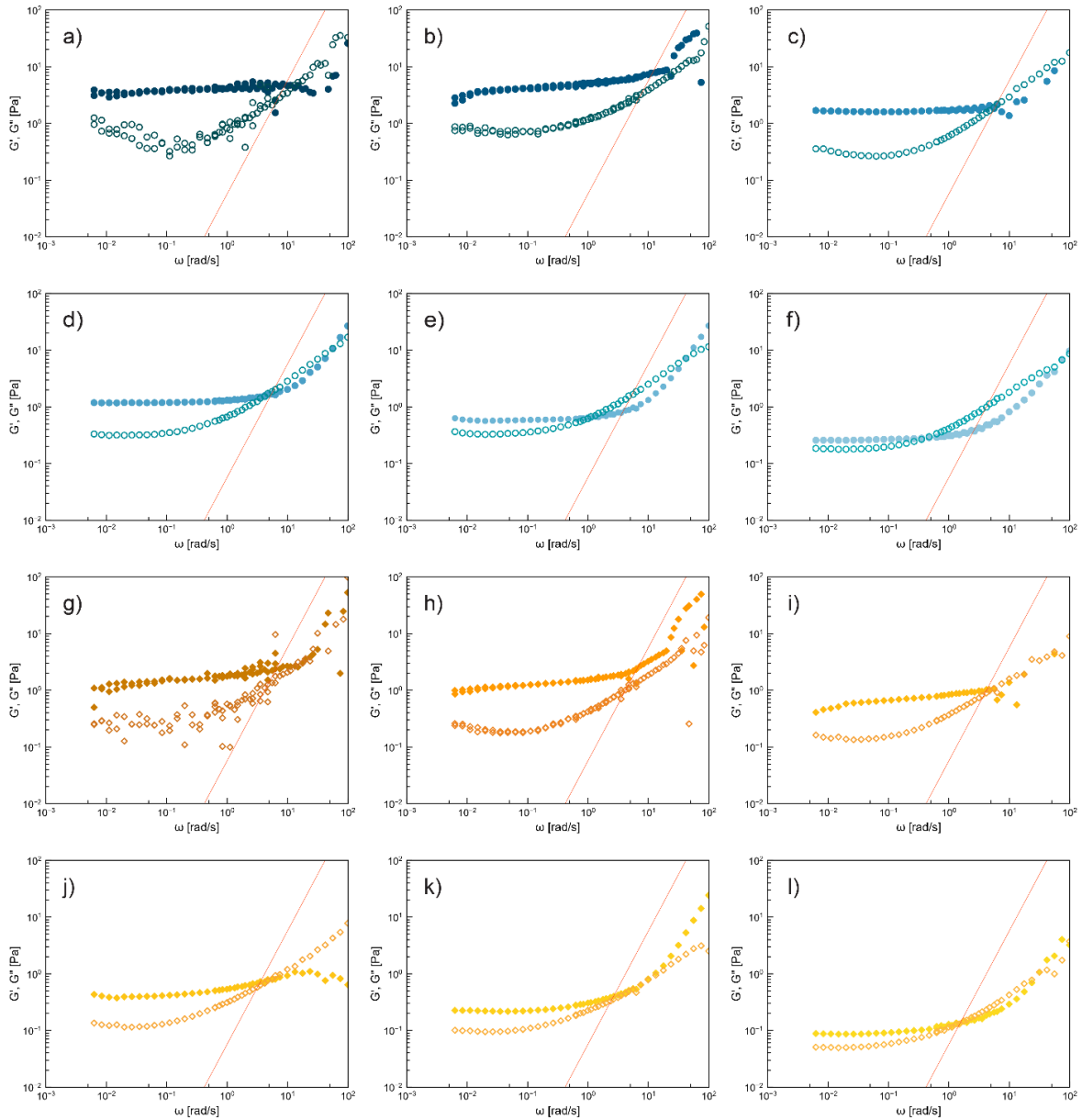
Fig. S2.7 Frequency response of 14BD/PC bijels comprising ϕ_{SNP} = 7.5 × 10^{-3} (a-l) and 1.5 × 10^{-2} (m-x) at small and medium strains. G' and G'' are marked by open and close symbols, respectively. The dark to light colors (or a->f, g->l, m->r, s->x) represent 1.0 × 10^{-2}, 1.0 × 10^{-1}, 1.0, 2.0, 5.0, and 10% strains, respectively. The blue and orange symbols represent measurements at 12 and 21°C, respectively. The red lines indicate the rheometer inertia limit.
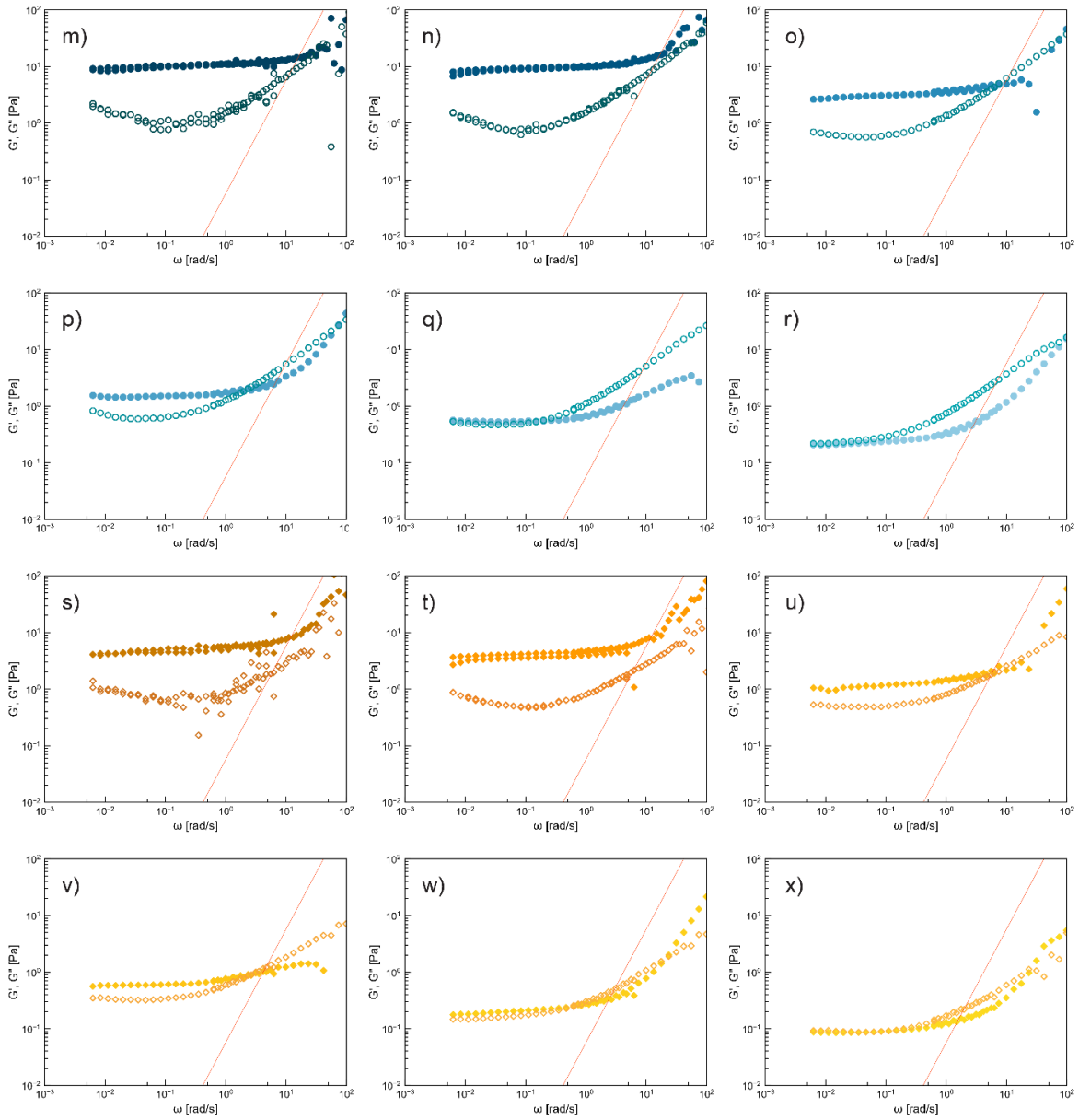
Fig. S2.7 Continue.
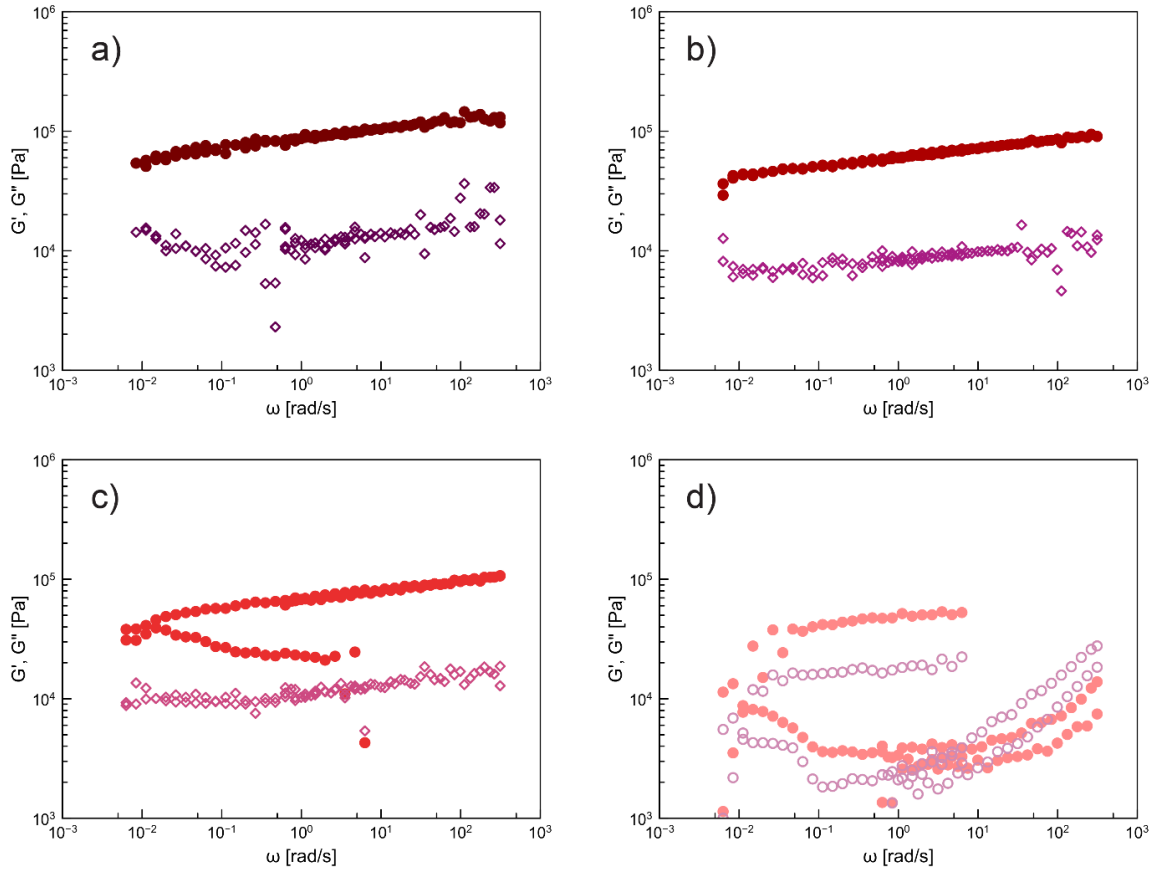
Fig. S2.8 Frequency response of 13BD/DOP capillary suspensions comprising ϕ_{PMMA} = 0.20 at small and medium strains. The strain amplitude of each frequency sweep is: (a) 1.0×10^{-2} %, (b) 2.5×10^{-2} %, (c) 4.0×10^{-2} %, (d) 1.0×10^{-1} %. G' and G'' are marked by open and close symbols, respectively.

CHAPTER 3: Fluidization of jammed particles introduces nonlinear phenomena in bijels

3.1 Introduction

Bicontinuous interfacially jammed emulsion gels, or bijels, are solid-stabilized emulsions uniquely distinguished by its co-continuous and interpenetrating fluids domains that are mechanically stabilized by a particle ladened interface.[1] Bijels are typically self-assembled by initiating spinodal decomposition in a dispersion of nanoparticles suspended in a partially miscible fluid mixture.[3,5,72] Upon phase separation, nanoparticles are irreversible adsorbed to the continuous interface with adsorption energy >10^3 k_bT.[73] Meanwhile, the minimization of interfacial area by interfacial tension aligns and compresses the particles together until the surface coverage approaches the 2-dimensional (2D) jamming limit.[40,74] The congregation of particles along the interface restricts further coarsening through steric resistance and impart sufficient mechanical rigidity to sustain a self-standing emulsion.[2,26] Due to the mechanism by which it is formed, the internal microstructure of bijels bears a striking resemblance to the morphology of spinodal decomposition, namely: fully co-continuous fluid domains, uniform domain size, and a continuous interface with zero mean, negative Gaussian curvatures.[1,17] Furthermore, the domain size of bijels can be modulated by varying the concentration of nanoparticles within the mixtures.[2,75,76] The combination of these microstructural features demonstrates high transport potential as compared to other porous materials derived from discrete emulsion templating, powder sintering and particle templating.[77] As such, bijels have been pursued by numerous researchers to develop next the generation of functional porous materials such as

bio-implantable tools,[15,16] components for electrochemical devices,[7–10,4,11,12] high surface area catalysts,[78,13] and structural composites.[31,79]

While bijel-derived materials have been an active area of research since 20XX, the general lack of understanding of the mechanism by which bijel yields greatly impedes the implementation of bijel-related technologies.[41,80] To address this concern, Lee and Mohraz conducted the first rheological study on water/2,6-lutidine (W/L) and nitromethane/ethylene glycol (NM/PG) bijels, and concluded that greater interparticle attractions in W/L bijels resulted in more mechanically robust bijels, which enables templating into bijel derived polymer while NM/PG bijels yielded due to possible Marangoni forces.[18] Macmillan, et al. later performed a rheological investigation with in Situ confocal imaging on bijels prepared by direct shear and recorded two step yielding, and cited possible fluidization of the interface prior to microstructural break down.[25] Until recently, it was uncleared whether interparticle attractions are required to achieve mechanical stability in bijels,[3] or if bijels are more gel-like or glass-like given that particle rearrangement along the interface appeared be possible.[21–24] To address these uncertainties, we have recently investigated relation between interparticle attractions and the stability of bijels and demonstrated that, in the absence of strong interparticle attraction (<10 k_bT), interfacial jamming alone provides sufficient viscoelasticity to achieve mechanically stable in bijels. However, our investigation raises further questions. First, are bijels viscoelastic solids or liquids? Our demonstration of glassy dynamics in bijels revealed both α and β-like relaxation mechanisms similar to those found in colloidal glasses, and the rheology was aptly described by an early adaption of Mode Coupling Theory that was derived to model colloidal glasses. If one envisions bijels as colloidal glasses, bijels should ultimately relax via slow particle

exchanges between particle cages (β-kinetics), and behave as viscoelastic liquids.[81] However, one can also argue that the constant compression by interfacial tension and small capillary attractions would create energetic barriers that restricts particle motion, and limit complete relaxation of the particle cages along the interface. Furthermore, if bijels are truly glassy materials, how would particle dynamics change when interfacial packing deviate from the jamming limits? For jammed interfaces, deformation results in a net increase in total interfacial area, which lowers the surface coverage of particles, effectively un-jamming the interface.[71,69,82] And given that glassy materials derive viscoelasticity from the packing of particles,[60] bijels poses as an intriguing case study for the solid stabilized interfaces because slight increases in strain results in a drop in the surface packing and the viscoelasticity of the interface. Meanwhile, interface tension continuously re-compresses the interface towards the 2D packing limit.[21,24] Therefore, the rheology of bijels, even small strain, is likely a rate dependent competition between the deformation induced unjamming of the interface and the re-jamming of the interface by interfacial tension.

To follow up on our previous article on the glassy rheology of bijels, here we report a set of experiments designed to relate particle dynamics and interfacial compression to bijel rheology. First, we performed a simple stress relaxation experiment to elucidate the behavior of bijels in the extreme short and long-time limits. Such experiment supplements crucial information regarding the nature of α and β-like relaxation in bijels, which are difficult, if not impossible, to test for in typical frequency sweep experiments ($<10^{-3}$ Hz or $>10^2$ Hz) due to the length of the experiment and the rheometer measurement limits.[65] From these stress relaxation results and the frequency results outlined in our previous article, we propose the application of a double Maxwell viscoelastic model, whose Maxwell-elements

described the short time α and long time β relaxation, to capture the general rheology of bijels. This simple model will serve two purposes: 1) it simplifies the complex α and β dynamics to two distinct relaxation time scales that captures the gross features of bijel rheology, and 2) it sets a basis to study the physical origin of the yielding that arise in large strain deformation experiments. Next, we revisited the transition from linear to nonlinear rheology by conducting a series of oscillatory experiments at different fixed frequencies and strain amplitudes, and characterized the nature of nonlinearities during the oscillation cycles. The onset, and the nature of nonlinearities revealed important information regarding competing effects of shear induced un-jamming of the interface against the continual compaction of the interface by interfacial tension. To account for these competing effects, we incorporated nonlinear and shear rate and shear strain dependent Maxwell elements that physically represent the loss of viscoelasticity due to shear induced dilation of the interface, and demonstrated overall prediction of the linear to nonlinear transitions by our implementation of the nonlinear double Maxwell model. Overall, our findings affirms that glass-like particle dynamics plays an important role in the rheology of bijels, and interfacial compaction is the predominant contributor for viscoelasticity and mechanical stability in bijels. Furthermore, the onset of yielding originates from the lowering of interfacial surface coverage lead by deformation induced dilation of the interface, resulting in fluidization of the interface.

3.2 Materials and methods

3.2.1 Materials

All materials were used as received. 1,4-butanediol (BD, 99%), propylene carbonate anhydrous (PC, 99.7%), fluorescein isothiocynate isomer I (FITC, ≥90%), and tetraethyl

orthosilicate (≥99.0%) were purchased from Sigma Aldrich. (3-aminopropyl) triethoxysilane (APTES, ≥98%) was purchased from TCI America. HPLC grade filter water was purchased from Fisher Chemical. Strong ammonia hydroxide solution (27-30%) was purchased from VWR. Anhydrous ethanol (200 proof) was purchased from Rossville Gold Shield. Hexamethyldisilazane (HMDS, 98+%) was purchased from Alfa Aesar.

3.2.2 Silica nanoparticle synthesis

Monodispersed, fluorescently tagged silica nanoparticles (SNPs) were synthesized using a modified Stöber process, and subsequently silanized to achieve neutrally wetting with respect to BD and PC. In brief, 8.0 mg of FITC and 33.8 μL of APTES were mixed into 6.4 mL of anhydrous ethanol for 15 min to synthesize a silane-coupled fluorescent dye. Then 1 mL of the dye solution was reacted with 1 mL of water, 680 μL of tetraethyl orthosilicate in 8,8 g of anhydrous ethanol and 295 μL of strong ammonia solution for 3 h at 4°C. Next, 175 μL of HMDS was added to the reaction mixture and reacted for 18 h. In our experience, the silanization process is not fully reproducible and the synthesis procedure was repeated until neutrally wetting SNPs were produced, as confirmed by confocal laser scanning microscopy (CLSM, Olympus Fluoview 3000) visualization of successful bijel formation (see section 3 of Materials and Methods). The resulting particles were recovered via centrifugation and washed by repeated re-suspension in anhydrous ethanol. After three washes, the particles were dried in a 110°C vacuum oven for 1 h. The particles size (radius, a = 160 nm) and distribution (coefficient of variance, CV = 6.7%) was determined using a high-resolution scanning electron microscopy (SEM, FEI Magellan 400 XHR). A representative SEM micrograph is shown in Fig. S3.1.

3.2.3 BD/PC bijel formation

A non-volatile fluid mixture comprising 1,4-butanediol (BD) and propylene carbonate (PC) was chosen to prepare bijels for extensive rheological characterization. First, an ultrasonic horn (Sonifier 250, Branson Ultrasonics) was used to disperse SNPs in a critical mixture of BD and PC (56.0 vol% PC) at a particle volume fraction (ϕ_{SNP}) of 1.5%. The violent sonification also heated the mixture to roughly 50°C (well above its upper critical solution temperature of 30.3°C). Then, a small aliquot of the mixture was transferred to a preheated glass cuvette (400 µm ID, VitroCom) for the purpose of assessing the wettability of SNPs with respect to BD and PC. By placing the hot cuvette onto a room temperature heat sink (~22°C), the sudden drop in temperature initiates spinodal decomposition and begins the bijel formation process. SNPs which are too hydrophobic (too much HMDS) or too hydrophilic (not enough HMDS) would produce discrete droplets while neutrally wetting SNPs would produce bicontinuous structures. In this study, the criteria for successful bijel formations are the formation of bicontinuous fluid domains and uniformity in the domain sizes, as verified through CLSM imaging. An example of successful bijel formation is shown in Fig. 3.1.
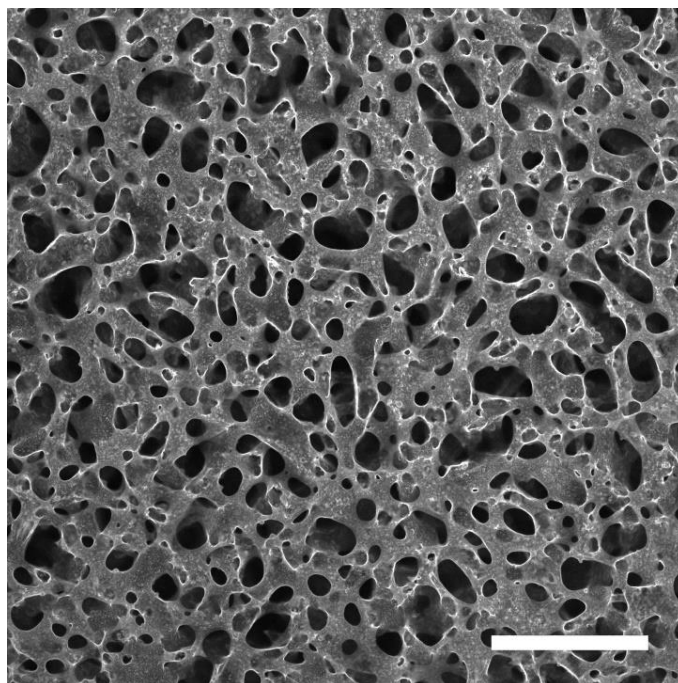
Fig. 3.1 Confocal laser scanning microscopy micrograph of a BD/PC bijel prepared with ϕ_{SNP} = 1.5 × 10^{-2}. The bright pixels correspond to the locations of fluorescently tagged SNPs. Scale bar = 200 µm.

3.2.4 Bijel rheology

The rheological behavior of the BD/PC bijels were characterized using a stress-controlled rheometer (DHR-3, TA Instruments) equipped with a cone-and-plate geometry (2°, 40 mm dia., sandblasted) and a temperature-controlled bottom plate. Bijels were formed on the rheometer using SNPs that has been tested by CLSM for successful bijel formation. To form the bijels, the hot dispersion mixture was transferred directly to the preheated (36°C) rheometer stage, and pre-sheared at 30 s^{-1} for 20 s. Then a rapid temperature quench (approx. -0.35°C/s) was applied to initiate bijel formation at 21°C. Meanwhile, a 2 h long small amplitude oscillatory shear test (SAOS, strain γ = 1.0 × 10^{-1} % and frequency ω = 6.3 × 10^{-1} rad/s) was applied at the beginning of the temperature quench to: 1) monitor the formation of the bijels, and 2) allow for slow particle rearrangements along the interface to approach the maximum close packings (or the steady state viscoelasticity).[23] To perform

stress relaxation experiments, a γ = 0.5% step strain (rise time = 0.01 s) was applied to the bijels after the 2 h SAOS, and the stress was monitored for 24 h. In our experience, there are significant differences in the shear moduli between each bijel that were formed. As such, small and medium amplitude oscillatory shear (MAOS) tests were conducted in succession on one single bijel to maintain consistency in the data. These SAOS-MAOS tests were conducted by performing two oscillation cycles at different fixed frequencies (ω = 1.3×10^{-1}, 6.3×10^{-1}, 0.63, 6.3 rad/s) from low to high amplitudes (γ = 0.1%, 1%, 5%, 10%), and recording the real-time stress and strain information throughout the oscillation cycles (~488 pt./s). Small to medium amplitude oscillatory frequency sweeps were also perform at strains of γ = 0.1%, 1%, 5%, 10% and frequencies spanning from ω = 6.3×10^{-3} to 6.3×10^2 rad/s.

3.3 Results and discussion

3.3.1 Long- and short-time relaxation in bijels

An example of the relaxation behavior of BD/PC bijels in response to a γ = 0.5% step strain is plotted in Fig. 3.2. Immediately after the 0.01 s step strain, bijels express a high modulus plateau (~500 Pa) that relaxes to a secondary plateau (~10 Pa) after ~5 s, which ultimately relaxes again to near-zero stress after $\sim 3 \times 10^4$ s. This slow and fast relaxation behavior is consistent with relaxation of other condensed materials, such as colloidal glasses and gels,[83,84] concentrated suspensions,[85] polymer systems.[86,87] For these materials, the short time (or high frequency behavior) is associated with a glassy state that transitions to a rubbery state at intermediate time, and eventually relaxes to viscous flow at long time (or low frequency). Recently, we have presented evidence of both short- and long-time dynamics in bijels that are attributed to particle caging dynamics similar to the in-cage (α-relaxation)

and out-of-cage (β-relaxation) found in colloidal glasses. Here, our two-step relaxation result further corroborates with our previous claims, where α and β-relaxations contribute to high and low frequency relaxations, respectively. In bijels, bulk deformation likely leads to isotropic deformation of interface in the form of extension, compression, shearing, and bending. In the direction of compression, shearing and bending, the sudden step strain applied rapid shearing to the concentrated particle network and prompted shear-induce jamming towards the glassy state, where particles are seized and rendered immobile like shear of 3D glasses.[88] After some time, in-cage particle motions relax the jammed particles and directs the system into a rubbery state where particle cages are placed in an unfavorable configuration along the interface because of the applied strain.[89] Over time, Brownian motions of the particles open temporary gaps by chance and allow for particle exchange between the cages, which also distribute local stresses throughout the interface.[90] This process continues until the interface is fully relaxed, and the particles are oriented in the configuration of the deformed interface. The lack of a third, long-lasting, plateau also confirmed that the stressed interface can be fully relaxed by slow β-relaxation. And the compaction of the interface by interfacial tension does not restrict relaxation dynamics at long time, or results in long lasting stressed particle structures like those found in viscoelastic solid materials such as colloidal gels.[91]
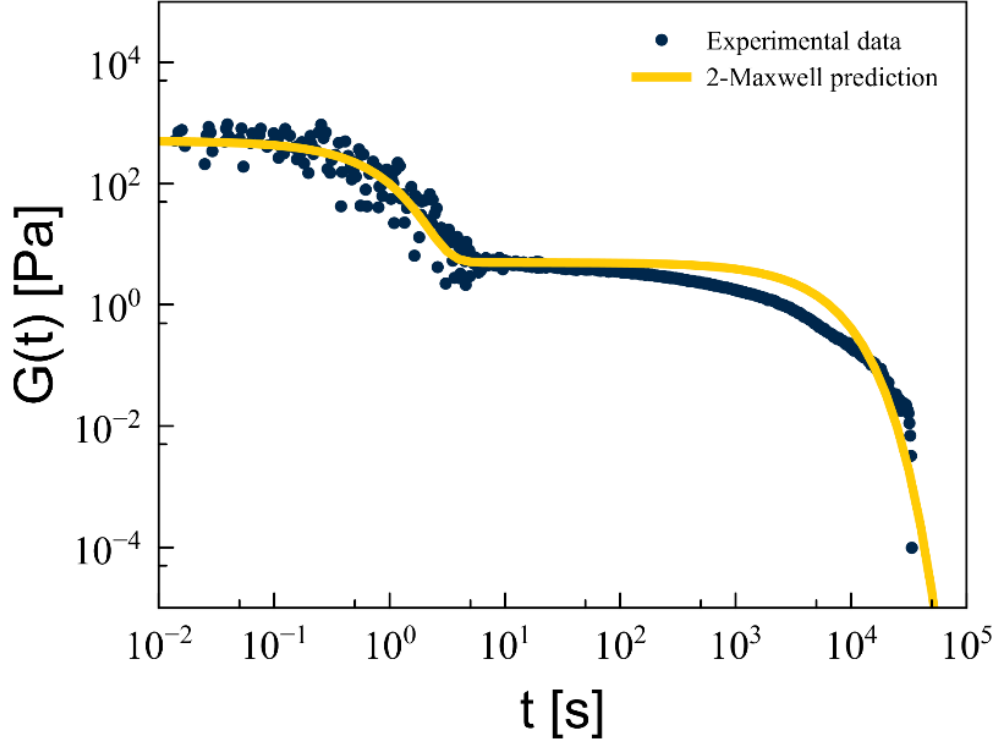
Fig. 3.2 Example of stress relaxation behavior (blue circles) of BD/PC bijels (ϕ_{SNP} = 1.5 × 10^{-2}) in response to a step strain γ = 0.5% (rise time = 0.01s). The stress response σ(t) is plotted as the shear modulus G(t) = σ(t)/γ. The yellow solid line represents stress relaxation prediction by a viscoelastic model comprising two Maxwell materials configured in parallel (see Fig. 3.3, G_1 = 3.5 Pa, G_2 = 100 Pa, η_1 = 10000 Pa·s, and η_2 = 0.5 Pa·s).

      Having established that the dynamics of the particles within bijels are analogous to Brownian motions of particles in colloidal glasses, we propose a simple viscoelastic model comprising two Maxwell materials in parallel (illustrated in Fig. 3.3) to model the rheology of bijels and to investigate the sources of nonlinearity within bijels, which will be discussed in latter sections. In a Maxwell system, the distribution of recoverable (γ_e) and unrecoverable (γ_v) strain (total strain $\gamma = \gamma_{e,n} + \gamma_{v,n}$, where n differentiate the two viscoelastic pathways) are determine by the overall shear rate ($\dot{\gamma}$) and the relaxation time constant $\tau_n = \eta_n/G_n$, where η_n is the viscosity and G_n is the elastic modulus. Here the assumption is that one set of spring and dashpot (n = 1) represents the viscoelasticity of the short time (high frequency) response corresponding to the fast, in-cage ballistic motions of particles bouncing against

neighbors, while the other set of spring-dashpot (n = 2) describes the long time (low frequency) behavior corresponding to the slow, out-of-cage exchange of particles between cages. Together, the total stress is defined as $\sigma = \sigma_1 + \sigma_2$, and each Maxwell element has the constitutive equation:

$$\dot{\sigma}_n + \frac{G_n}{\eta_n}\sigma_n = G_n\dot{\gamma},$$

where the dot notation represents differentiation with respect to time. This model, while simple, has profound rate dependent mechanical responses that connect to the physical properties of glass-forming liquid such as colloidal glasses and bijels. In bijels, the transition to the glassy state only occurs at sufficiently high shear rate, and the corresponding shear energy is stored in the first set of spring and dashpot. Note that the other spring also store elastic energy, but at a much lower magnitude. After some short period of time (~5s), $\gamma_{e,1}$ relaxes via viscous dissipation by the dashpot, and the overall materials properties only depends on the other set of spring and dashpot (i.e., $\gamma_{e,1} = 0 \rightarrow \sigma_1 = 0 \rightarrow \sigma = \sigma_2$), which has τ_2 >> τ_1. Over a long period of time (~>10^{-4} s), $\gamma_{e,2}$ also relaxes via viscous dissipation, and the material appears as a viscoelastic liquid. Fig. 3.2 presents simulated stress relaxation response using the constitutive equation for the double Maxwell model (G_1 = 3.5 Pa, G_2 = 100 Pa, η_1 = 10000 Pa·s, and η_2 = 0.5 Pa·s). Overall, this model captures the essentials two-step relaxation behavior by incorporating two distinct relaxation time scales. Note that this is a simplified approximation of the rheology by restricting α- and β-relaxation to two distinct time scales. A continuous relaxation spectrum or a statistical based model such as Mode-Coupling theory would more accurately depict the Brownian dynamics of colloids clustered at the interface, as we have shown in Chapter 2. Nonetheless, this model captures the gross

features of bijel rheology and we will utilize it as a basis for investigating the dynamics

particles in bijels in response to medium strain deformations.
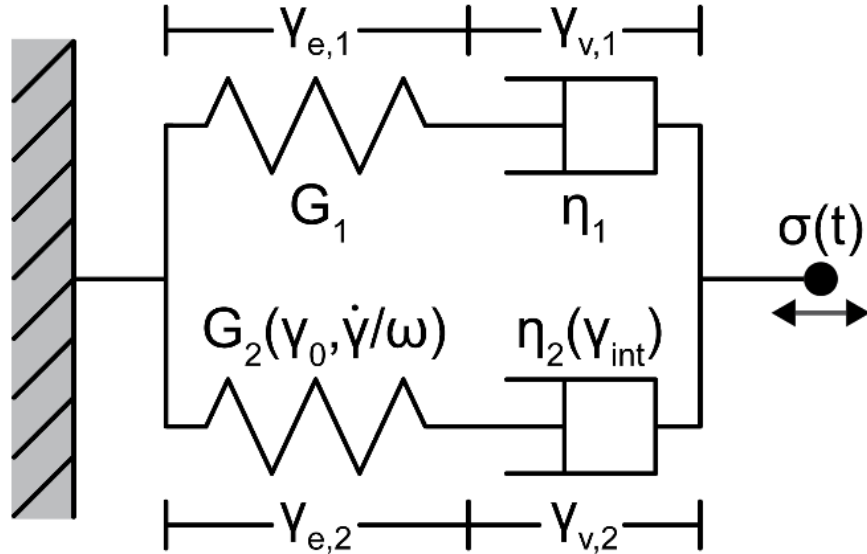
Fig. 3.3 Schematic illustration of the double Maxwell viscoelastic model. Each Maxwell system constitute one set of recoverable and unrecoverable strains (γ_e and γ_v, respectively). For this study, the elastic modulus G_1 and the viscosity η_1 representing the fast in-cage dynamics are held constant, while G_2 and η_2 representing the slow out-of-cage dynamics are defined as functions of the interfacial strain γ_{int}, strain amplitude γ_0, and the normalized shear rate $\dot{\gamma}/\omega$.

3.3.2 Nonlinear bijel rheology

In our previous demonstration of glassy dynamics in bijels, we have hinted that large

strain deformation can lead to shear-induced stretching of the interface, which lowers the

interfacial coverage and fluidizes stressed particle cages. Such dynamics are reflected in the

nonlinear rheology of bijels under intermediate strains, which is exemplified in Fig. 3.4a-b.

Here, bijels are subjected to small and medium strain oscillatory shear (γ = 0.1% and 10%,

respectively). At low strain, the stress response appears to be sinusoidal with a small phase

angle deviation from the applied strain, indicating linear viscoelastic response. Medium

strain deformation brought about a distorted and backward tilted stress response, where

the stress precipitately dropped at the return from maximum strain, and noticeable increased viscous effect (non-zero stress) during the high shear rate (~zero strain) portion of the oscillation cycle (Fig. 3.4b).[92] These behaviors contain important information regarding the onset of yielding which are not captured by the calculation of simple storage (G') and loss (G'') moduli. We believe these nonlinear phenomena can be explained by the competition between the shear-induced fluidization of the interface and the re-compaction of the interface by interfacial tension. As stated, shearing, even at small strain, will bring about stretching of the interface, which lowers the overall surface coverage along the interface. Given that compacted materials such as the jammed interface in bijels develop their mechanical rigidity from densely packed materials,[60] reduction in surface coverage is accompanied by loss of viscoelasticity. At intermediate strains, the interface would dilate to a point where the cages are dissolved and the particles' lateral in-plane movements become less restricted, resulting in overall fluidization of the interface that is similar in principle to diluting a 3D colloidal glass.[93] Unlike colloidal glasses, however, there is a competing effect where the particle interface is continuously driven toward maximum packing limit by the interface, which piece the particles together to recover the viscoelasticity of the interface. As such, the underlying physics for the rheology of bijels is likely a strain rate dependent function that encompasses the interplay between α and β relaxations, the rate of deformation, and the rate of re-compaction.

To elucidate the rate dependency of nonlinear bijel rheology, the stress response to oscillatory shear at strain amplitude γ_0 = 0.1%, 1%, 5%, and 10% and frequency ω = 0.009, 0.063, 0.63, and 6 rad/s are plotted as Lissajous curves (stress vs strain) in Fig. 3.5. In all cases (low and high strains), bijels exhibited increased viscous behavior at high and low

frequency, which are in part attributed to the competition between α and β relaxations. Nonlinearities in the stress-strain cycles were observed in the transition from low to high strains, i.e., the Lissajous curves are not symmetric along the elongated axis. In all large-strain cases, the bijels saw increase viscous behavior in the high shear rate, or zero strain, regions of the oscillatory cycles as marked by the reduced slope, but non-zero stress. The increase in strain also brought about a precipitate drop in stress during the return from maximum strain, as mentioned earlier. Furthermore, in the low frequency and high strain limits, the Lissajous curves appear as parallelogram-like shapes, signifying regions of constant modulus. We interpret these behaviors as increased plasticity in the system owing to high shear rate deformation. At higher shear rates, the interface is stretched faster than it can re-jam, resulting in a loose particle network which translates to lowered viscosity and increased viscous behaviors. Physically, excess interfacial area dissolute particle cages and limits storage of elastic energy throughout the particle cages/network. As such, increased plasticity lowers the recoverable strain throughout the high shear rate portion of the oscillation cycle. Note, it is likely that this shear induced plasticity is localized to region of the interface that is stretched. Given that the bijel microstructure is isotropic, other portions of the interface are bent, sheared, or compressed and resulted in some locally stressed particle cages. As shear rate slow down to zero (or strain $\gamma \to \gamma_0$), viscoelasticity is recovered as the interface re-compacts into a new jammed state (if time allows). At this point in the oscillation cycle, viscosity of the network is high and small decreases in strain from the maximum strain rapidly relaxes stress cages, resulting in a rapid drop in stress.
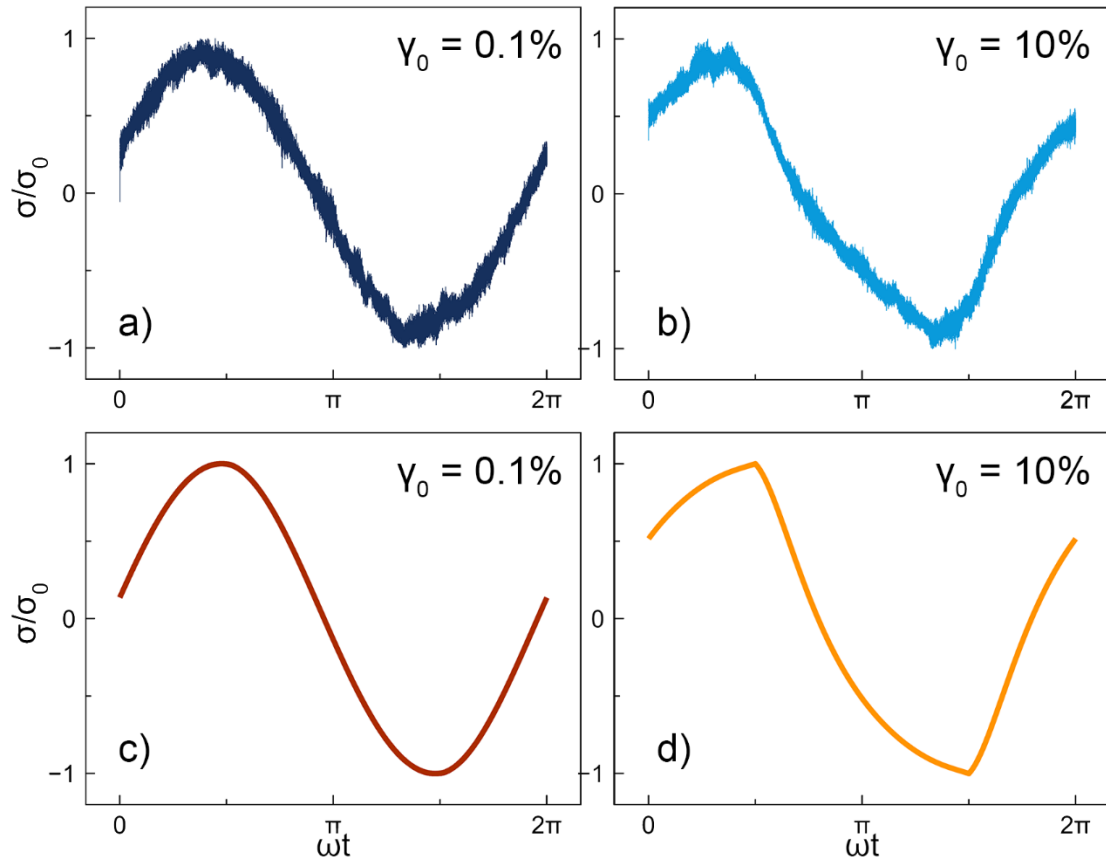
Fig. 3.4 Normalized stress response (σ/σ_0) of bijels under 0.1% (a) and 10% (b) oscillatory strain plotted as a function of ωt (ω = 0.009 rad/s). The corresponding simulated normalized stress responses (σ/σ_0) by the nonlinear double Maxwell model are plotted below (c-d).
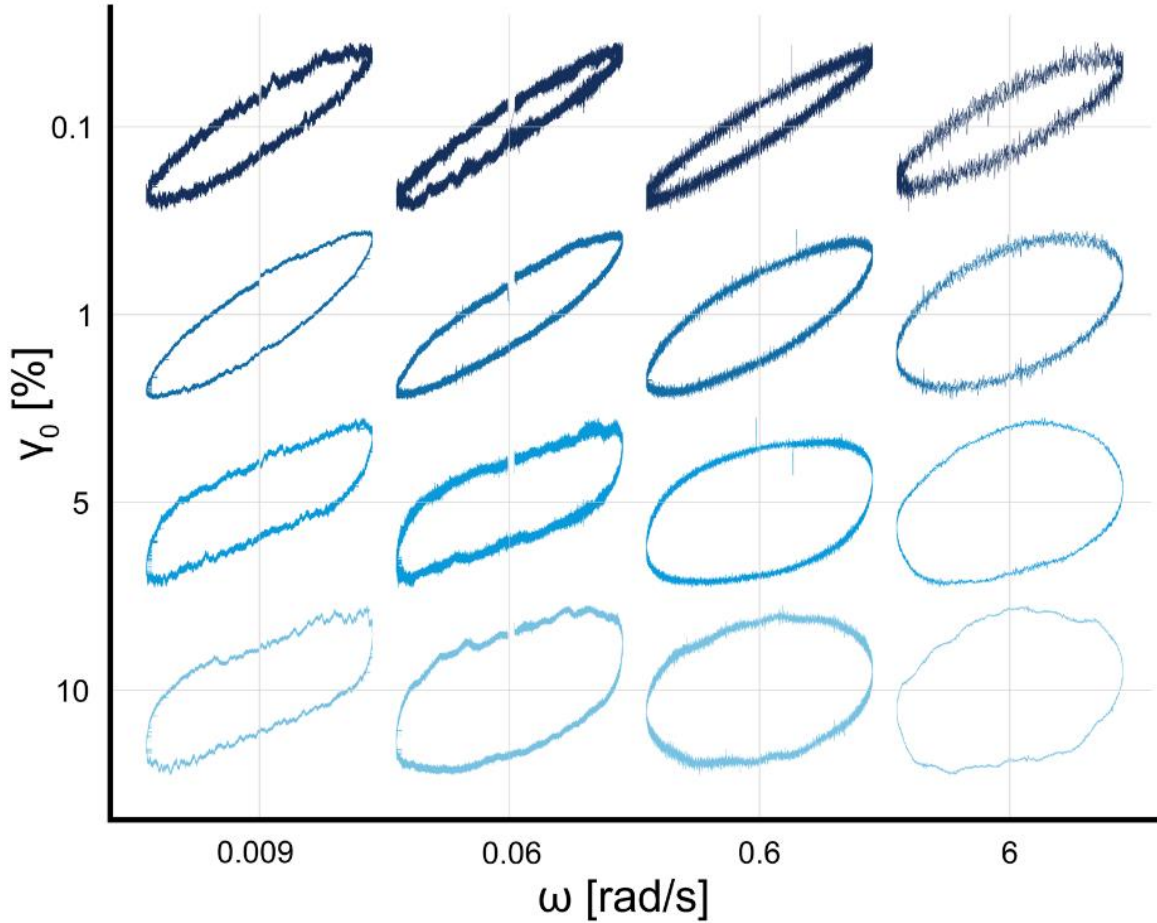
Fig. 3.5 Lissajous plots (stress vs. strain) of bijels under small and medium amplitude oscillatory shear at different oscillation frequencies (ω). Each Lissajous plot was normalized to its stress amplitude (σ_0) and stain amplitude (γ_0). A 500 point (recorded at $\sim$488 pt./s) running average was applied to each plot to smooth out the measurement noise for illustration purposes.

3.3.3 Nonlinear double Maxwell model

To account for the dilation of the interface, we propose nonlinear G_2 and η_2 functions to account for the loss of viscoelasticity associated with shear-induced dilation of the interface. Analogous modifications have been demonstrated before by Kamani, et al., and de Souza Mendes to describe the linear-to-nonlinear transition of structured, yield stress fluids such as glasses and gels.[94,95] In Kamani's model, they incorporated a Herschel-Bulkley representation of viscosity to model the plastic deformation of yield stress fluids. Likewise, de Souza Mendes proposed the use of a structural factor λ which defines the functions $G(\lambda)$

and $\eta(\lambda)$ to describe the change in viscoelasticity in response to shear induced changes of the internal microstructure. Other stepwise constitutive laws have also been proposed as well. For instance, Dimitrious et al. defined the onset of plasticity by a specifying a critical stress that switches the material properties to plastic behavior.[96] In bijels, plastic deformation initiates when shear rate exceed re-compaction rate to create excess interfacial area. Therefore, we recommend the use of a shear rate-dependent interfacial strain γ_{int} as described by the ordinary differential equation:

$$\frac{d\gamma_{int}}{dt} = \dot{\gamma} - R_f \gamma_{int},$$

where R_f represents the restorative elastic force by interfacial tension. Physically, this equation describes the interfacial area created by $\dot{\gamma}$, and the minimization of free surface area by interfacial tension. For oscillatory shear $\gamma(t) = \gamma 0 * Sin(\omega * t)$, the above equation simplifies to:

$$\gamma_{int} = \frac{-\gamma_0 R_f \omega}{R_f{}^2 + \omega^2} e^{-bt} + \frac{\gamma_0 \omega (R_f \cos(\omega t) + \omega \sin(\omega t))}{R_f{}^2 + \omega^2}.$$

We postulate at low interfacial strain γ_{int}, the viscoelasticity of the interface approaches its maximum terminal values. As γ_{int} increases, excess interfacial area loosens the particle network and increase particle mobility. As such, α relaxation (inter-cage exchanges) time scale τ_2 shortens. To model this behavior, we defined $\eta_2(\gamma_{int})$ with a sigmoid function that exponentially weakens at high γ_{int}. The sigmoidal function is defined by:

$$\eta_2(\gamma_{int}) = \eta_0 10^{\left(\frac{c_1}{1 + c_2 |\gamma_{int}|^{c_3}} - c_1\right)},$$

where η_0 is the viscosity corresponding to maximum interfacial coverage, and c_n are constants that define the magnitudes, decay rate, and inflection point of the sigmoidal

function. The absolute value of the shear rate γ_{int} was applied to account for the negative strain in the oscillation cycle. The parameters c_n that were chosen for this study and their resulting sigmoidal function are shown in Fig. S3.2. Note that G_0 = 15 Pa, η_0 = 40,000 Pa·s, c_n and were chosen to match the nonlinear rheology data shown in Fig. 3.5 and 3.7, and they do not match the values presented in Fig. 3.2. The stress relaxation experiments were conducted by rapid shearing (high $\dot{\gamma}$) which likely resulted in nonlinear dynamics at the interface, therefore the result in Fig. 3.2 does not accurately represent the linear rheology of bijels. Furthermore, each bijel that were tested varies slightly in their shear moduli and relaxation behavior. Here, we focus our analysis on qualitive measure of changes in shapes of the Lissajous curves as well as changes in G' and G'' at increasing strain amplitude γ_0. Fig. S3.3 and S3.4 illustrate simulated stress responses from small and intermediate strain deformation of the double maxwell model based on $\eta_2(\gamma_{int})$ alone. While this non-linear model captures some general features of the frequency response, primarily the flattening of G'' at increasing strain, and some weakening of G', it failed to predict the general shapes of the Lissajous curve and underpredicts the strain weakening behavior of G'.

The strain softening behavior in bijels is a non-trivial subject. From our previous examination of bijel frequency response at intermediate strains (also shown in Fig. 3.7 of this text), bijels appear to experience strain dependent and frequency (or strain rate) independent $G'(\omega)$ response. Furthermore, close examination of the Lissajous curves (see Fig. 3.5) suggests high G or low τ at the low shear rate (or maximum strain) portion of the oscillation cycle. Although this intra-cycle strain softening behavior appears to be coincide with high rates, the overall softening effect on G' is strain rate independent and only dependents on strain. We theorized that there are two effects contributing to strain softening

64

in bijel. First, previous rheological characterization of bijel evident that aging, or slow particle rearrangement into maximum packing, takes upward of 2 hours.[18,22,23] At increased strains, it is likely that re-compaction of the interface by interfacial tension does immediately recover the near maximum packing of the interface. As such, there the near-zero shear elastic modulus G_0 is likely a structural dependent function, similar to the model presented by de Souza Mendes.[94] Here, we will attempt to represent the structural dependency using a sigmoidal function G_{struc} that decays with the strain amplitude γ_0. Second, it is likely that the particle structure along the interface can only withstand some critical strain before shear induces force dislocation of particle. Since particles are dynamic along the interface, this force dislocation occurs when only strain and shear rate are sufficiently high. To replicate this behavior, we introduce a strain-like parameter $\dot{\gamma}/\omega$ and an exponentially decaying function $G_{dis}(\dot{\gamma}/\omega)$. Together, we propose the following mathematical representation for the nonlinear behavior of G_2:

$$G_2\left(\gamma_0,\frac{\dot{\gamma}}{\omega}\right) = G_0 * G_{struc}(\gamma_0) * G_{dis}\left(\frac{\dot{\gamma}}{\omega}\right) = G_0 10^{\left(\frac{c_4}{1+c_5\gamma_0^{c_6}}-c_4\right)}e^{-k|\dot{\gamma}|/\omega},$$

where k is decay constant. Incorporating the nonlinear η_2 and G_2 functions into the Maxwell model results in the following constitutive equation:

$$\dot{\sigma}_2 = \frac{\dot{G}_2\left(\gamma_0,\frac{\dot{\gamma}}{\omega}\right)}{G_2\left(\gamma_0,\frac{\dot{\gamma}}{\omega}\right)}\sigma_2 + G_2\left(\gamma_0,\frac{\dot{\gamma}}{\omega}\right)\left(\dot{\gamma} - \frac{\sigma}{\eta_2(\gamma_{int})}\right).$$

The above ordinary differential equation was solved numerically using the Mathematica NDSolve function and examples of the nonlinear stress response under small and medium strain oscillatory shear ($\gamma = 0.1\%$ and 10%, respectively) are plotted in Fig. 3.4c-d. At small strain, the model produced linear viscoelastic response that mirrors the experimental bijel result. At large strain, the model successfully demonstrated linear-to-

nonlinear transition. Specifically, it captured the precipitate drop in stress near $\gamma = \gamma_0$ and the increased plasticity near high $\dot{\gamma}$, which combined to produce a tilted backward stress response. We extended this analysis to the range of strains and frequencies reported in Fig. 3.5, and plotted the simulated responses as Lissajous plots in Fig. 3.6. Comparing the linear responses at low strain (top rows in Fig. 3.5 and 3.6), the model reproduced the increased viscous behavior (more circular response) at low and high frequencies, owing to the two relaxation time scales τ_1 and τ_2 that are associated with α and β relaxation, respectively. Across the tested frequencies, the model also predicted the increasing viscous-like behavior as strain increases, i.e., the Lissajous curves are increasingly circular like at large strains. Further, the onset and transition to the nonlinearities there were discussed above were demonstrated as well. In the medium strain and low frequency regime, the simulated response replicated the precipitate drop in stress at maximum strain, followed by near-constant modulus up to minimum strain, behaviors that were observed in our nonlinear rheology data (Fig. 3.5). Overall, over mathematical interpretation of the shear weakening and strain softening effects based on the shear-induced dilation of the interface demonstrates success in capturing the general linear to nonlinear rheology in bijels.
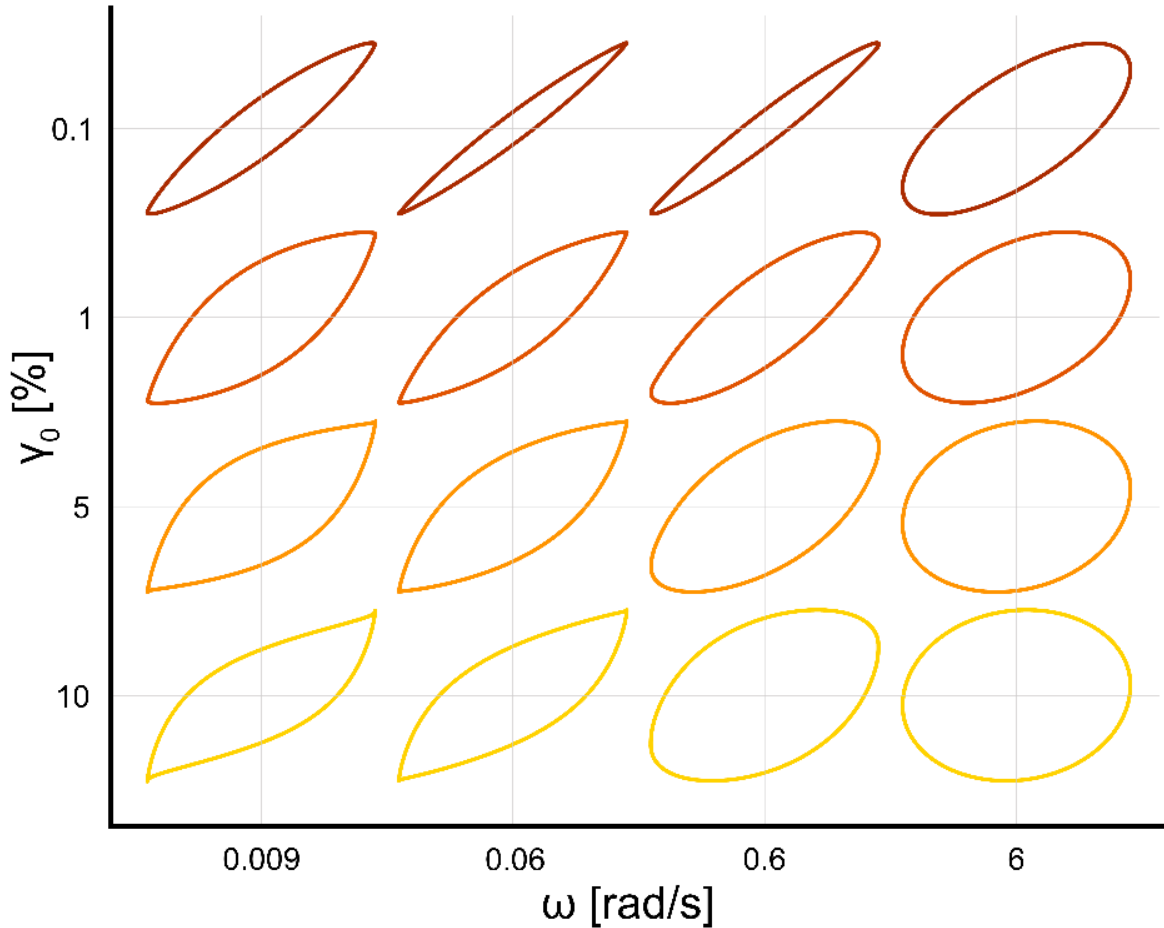
Fig. 3.6 Simulated Lissajous plots (stress vs. strain) of the nonlinear double Maxwell model (see section 3 of Results and Discussion) under small and medium amplitude oscillatory shear at different oscillation frequencies (ω). Each Lissajous plot was normalized to its stress amplitude (σ_0) and stain amplitude (γ_0).

3.3.4 Shear rate dependent particle dynamics

To summarize the strain shear rate dependency of bijel rheology, Fig. 3.7 displays the storage (G') and loss (G'') moduli representation of the frequency response of bijels and our nonlinear viscoelastic model under small to medium strain oscillatory frequency sweeps. Note that these results disregard the nonlinear components of the stress response and report only the primary harmonic. Nonetheless, they represent overall changes in viscoelastic moduli and the relaxation behaviors under large strain deformation. In our previous documentation of similar data, we have attributed the minimum in G'' (Fig. 3.7a) to the

competition between α and β dynamics, which have been further upheld by the stress relaxation experimental result in Fig. 3.2. Furthermore, we have previously reported flattening of the G'' as γ_0 increase (Fig. 3.7a-d), and suggested interference of α-relaxation by shear-induced melting of the interface. Here we tested our theory by qualitatively comparing the experimental data to our nonlinear double Maxwell model prediction (Fig. 3.7e-h). In the low strain limit ($\gamma_0 \leq 0.1\%$, Fig. 3.7e), our model produced a nearly flat G' response and a minimum in G'' that mirror the experimental data (Fig. 3.7a). The increase plasticity generated by shear-induced weakening G_2 and η_2 resulted in overall lowering of the G' similar to rheological results. Moreover, the G'' saw a minor increase as strain increase from $\gamma_0 = 0.1\%$ to 1%, as well as flattening of the low frequency G'' as strain amplitude increase. Remarkably, incorporating simple assumptions regarding the origin of nonlinearities in bijels, specifically the interplay between α and β dynamics, shear induced dilation of the interface, and the re-compaction by interfacial tension, into a simple double Maxwell model successfully predicts general trends of the linear and nonlinear viscoelastic response. The general applicability of our model revealed how disruption and simultaneous recovery of glassy dynamics contributes to both linear and nonlinear bijel rheology.
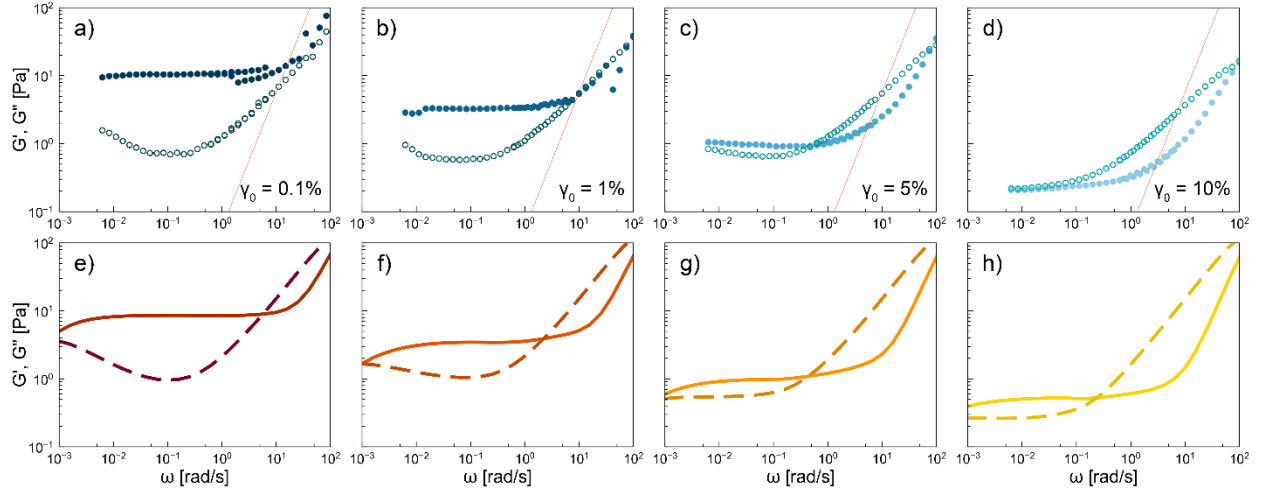
Fig. 3.7 (a-d) Frequency response of 14BD/PC bijels at small and medium strains. (e-h) Simulation of frequency response of bijels by a nonlinear two Maxwell model (see Fig. 3.3). G' are marked by close symbols or solid lines, and G'' are marked by open symbols or dash lines. The red lines in a-d indicate the rheometer inertia limit, which is at least an order of magnitude higher than the sample inertia.[65]

3.3.5 Nonlinear α relaxation

Having established that our proposed model captured the general features of linear and nonlinear bijel rheology, it is possible to numerically calculate the relaxation time $\tau_2 = \eta_2/G_2$ throughout the oscillation cycle to examine the change in α relaxation. $\tau_2(\omega t)$ is plotted alongside $\gamma(\omega t)$ and $\gamma_{int}(\omega t)$ in Fig. 3.8. At intermediate strain ($\gamma_0 = 10\%$) and low frequency ($\omega = 0.009$ rad/s), where nonlinearities were most apparently (see Fig. 3.5 and 3.6), the model predict precipitative drop in the relaxation time scale as the magnitude of γ_{int} increase, i.e., the α relaxation time is at the highest at low γ_{int}. This behavior is in line with our conjecture that creates excess interfacial area which promote particle escapement from cages. As shear rate lowers, and the interfacial tension recompact the interface, viscosity is recovered and extend α relaxation time. The dynamic relaxation time also have important implications for the recoverable ($\gamma_{e,2}$) and unrecoverable ($\gamma_{v,2}$) strains throughout the oscillatory cycle. $\gamma_{e,2}$ and $\gamma_{v,2}$ were numerically decomposed from the nonlinear model

prediction (γ_0 = 10%, ω = 0.009 rad/s) and plotted in Fig. 3.9. In a linear Maxwell system, the recoverable strain (γ_e) is proportional to the overall stress by a constant elastic modulus as shown in Fig. 3.9a. Because the distribution of strain between γ_e and γ_v depends on the instantaneous G and η, which are variable with respect to $\dot{\gamma}$ and γ_{int}, γ_e is no longer a linearly proportional to the resulting stress, and it is off phase from both the overall stress and strain. Overall, the model predicted greater storage of elastic energy as compared to a linear Maxwell model, suggesting that elasticity is recovered within the oscillation cycle despite the constant fluidization of the interface.
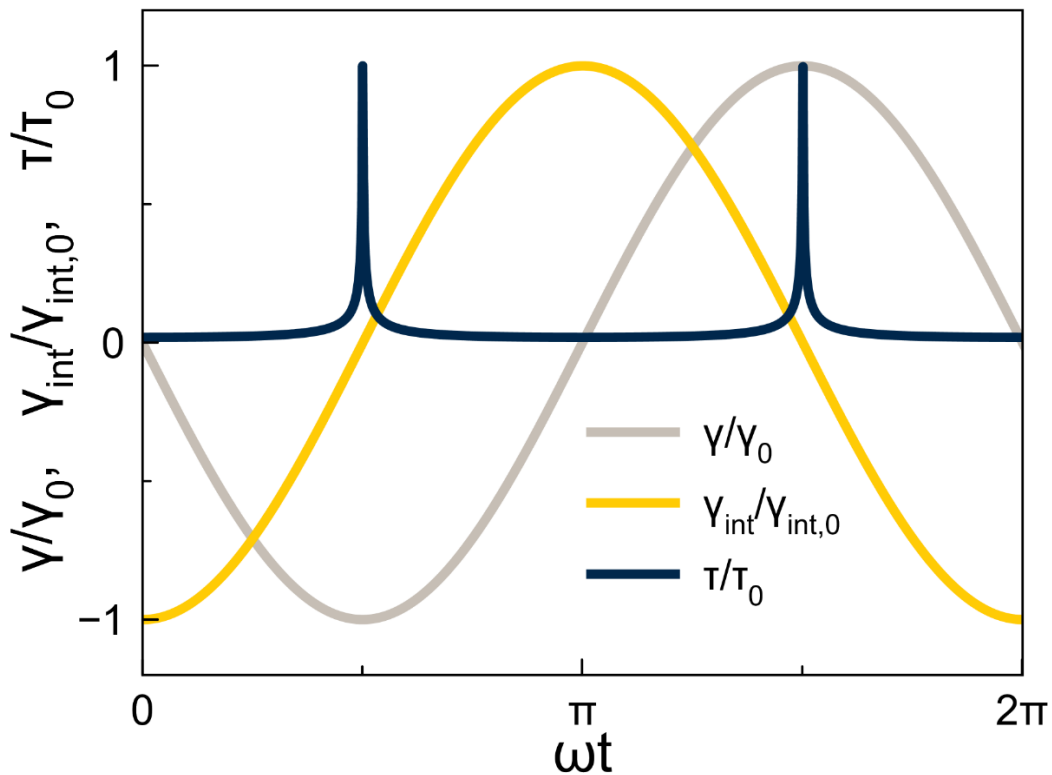
Fig. 3.8 Nonlinear relaxation behavior of bijels under medium amplitude oscillatory shear (γ_0 = 10%) plotted as a function of ωt (ω = 0.009 rad/s).
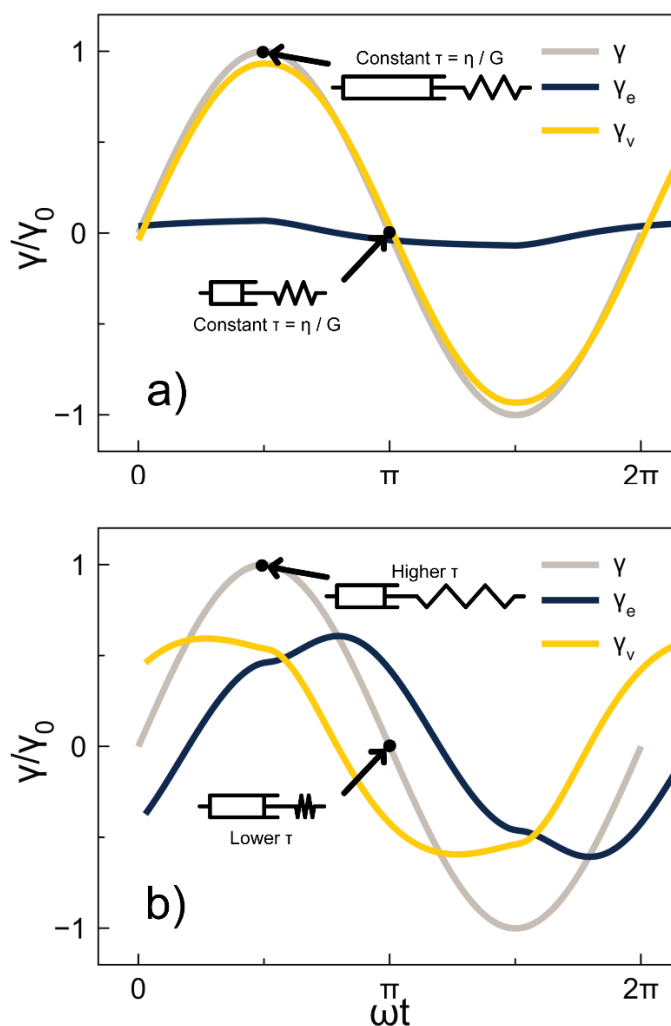
Fig. 3.9 Schematic illustration of oscillatory strain γ (grey) decomposed into recoverable (γ_e) and unrecoverable (γ_v) strains by a linear (top) and nonlinear (bottom, see Fig. 3.3) Maxwell model. Illustration of the spring and dashpot are included to represent the distribution of strain.

3.4 Conclusion

The linear-to-nonlinear rheology transition in bijels was investigated through nonlinear rheological measurements and explained by a qualitative comparison with a nonlinear double Maxwell model. Stress relaxation experiments were conducted to illuminate the extreme short and long-time rheology of bijels and revealed a viscoelastic liquid with a two-step relaxation mechanism. Building upon this finding and our previous investigation of glassy rheology in bijels, we developed a simple double Maxwell model,

whose relaxation time scales reflect Brownian-driven in-cage (β) and out-of-cage (α) dynamics, to explore the interplay between particle dynamics and interfacial deformation. Nonlinear oscillatory measurements reveal signatures of increases plasticity at high shear rates, which corroborate with our conjecture that shear-induced dilation of the interface results in fluidization of the 2D glass structure. We incorporated nonlinear spring and dashpot elements into the double Maxwell model to reflect the loss of viscoelasticity transpire by shear-induced dilation of the interface. Applying small strain oscillatory shear to the model reproduced the frequency response that were observed in bijel rheology. When subjected to higher oscillatory strain, the nonlinear model grossly captured the linear-to-nonlinear transitions where oscillatory shear result in a tilt backward response and increased plasticity at intermediate strain. In addition, the model also demonstrated the loss of viscoelasticity associated with high shear rate deformation, and generated frequency dependent shear moduli that mimics the MAOS response of bijels. Our findings suggest that the rheology of bijels is dominated by the competition between α and β dynamics, which are simultaneously interrupted and recovered by shear-induced stretching of the interface and re-compaction by interfacial tension, respectively.

3.5 Supporting information
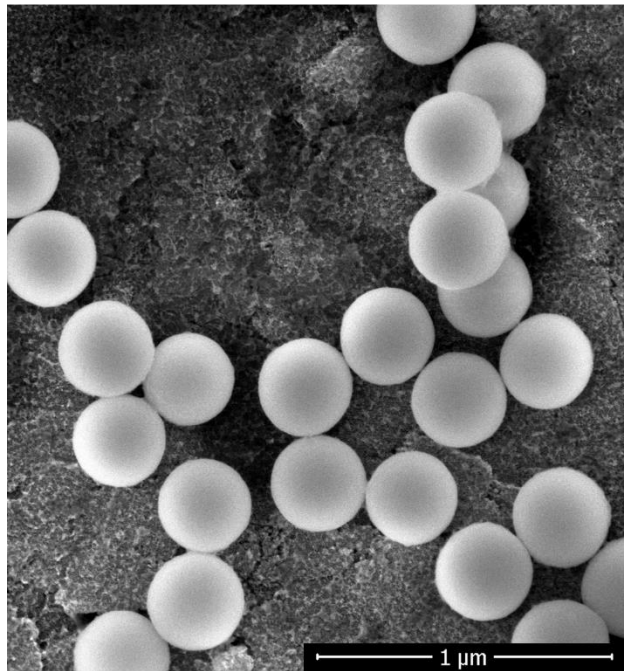
Fig. S3.1 A SEM micrograph of the SNPs used in the preparation of 14BD/PC bijels. Scale bar = 2 µm.
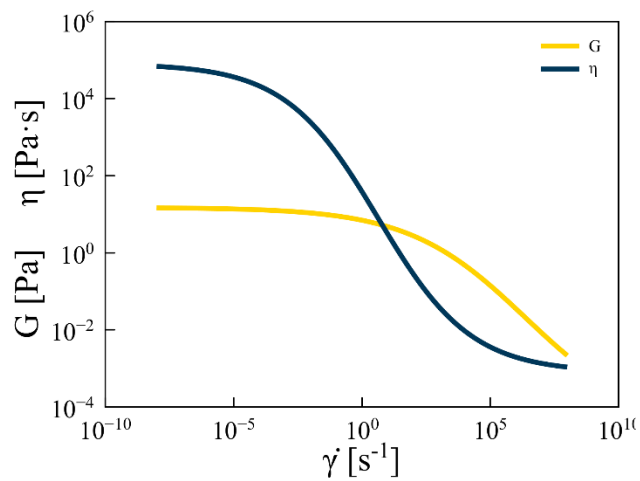
Fig. S3.2 The nonlinear behavior of $\eta_2(\gamma_{int})$ (blue) and $G_2(\dot{\gamma}/\omega)$ (yellow) plotted as a function of the overall shear rate $\dot{\gamma}$.
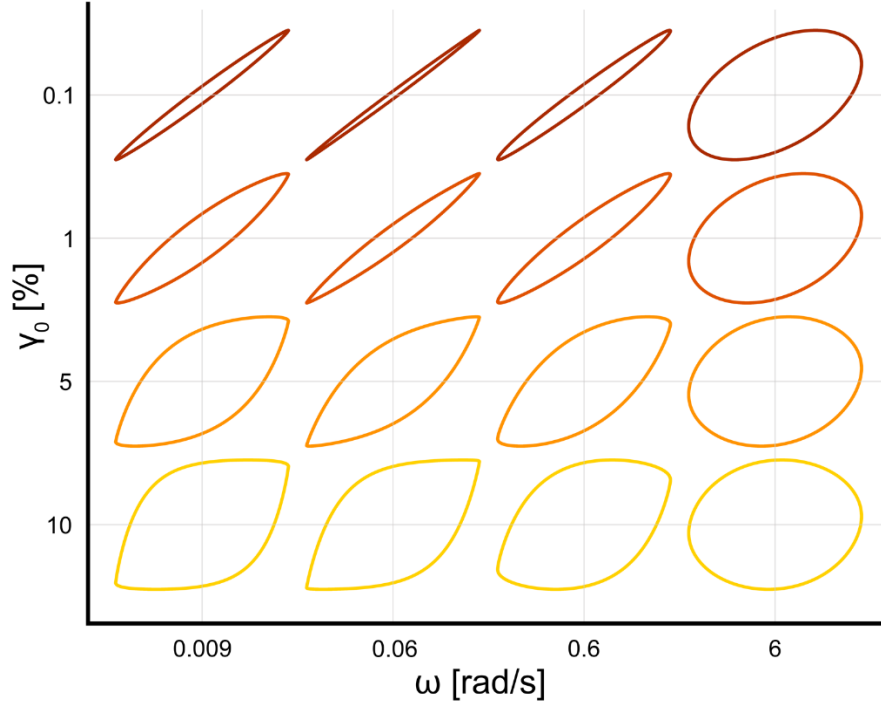
Fig. S3.3 Simulated Lissajous plots (stress vs. strain) of the nonlinear double Maxwell model based on $\eta(\gamma_{int})$ alone (see section 3.3 of Chapter 3) under small and medium amplitude oscillatory shear at different oscillation frequencies (ω). Each Lissajous plot was normalized to its stress amplitude (σ_0) and stain amplitude (γ_0).
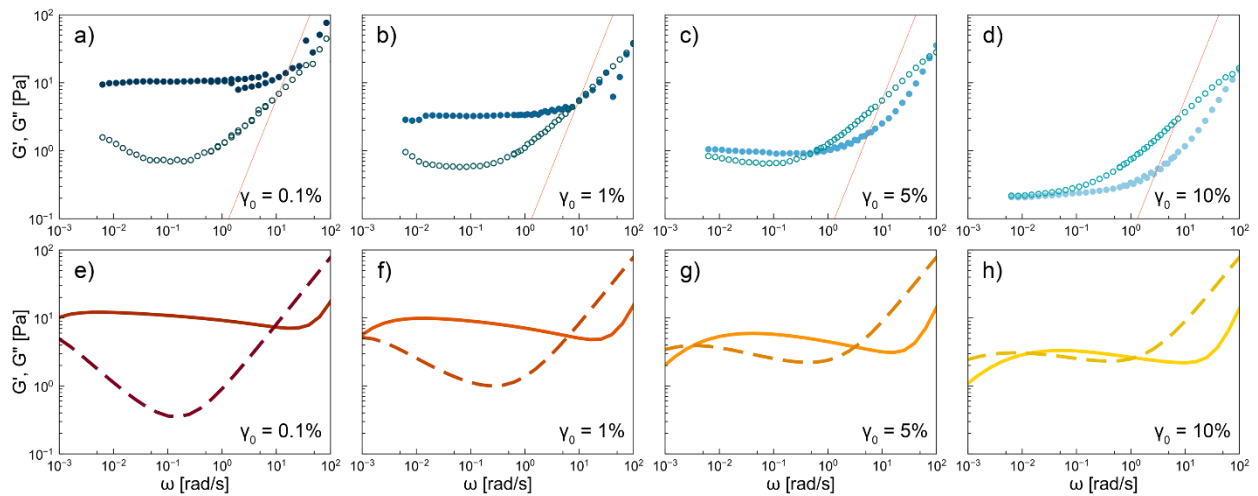
Fig. S3.4 (a-d) Frequency response of 14BD/PC bijels at small and medium strains. (e-h) Simulation of frequency response of bijels by a nonlinear double Maxwell model based on $\eta(\gamma_{int})$ alone (see Fig. 3.3). G' are marked by close symbols or solid lines, and G'' are marked by open symbols or dash lines. The red lines in a-d indicate the rheometer inertia limit, which is at least an order of magnitude higher than the sample inertia.[65]

CHAPTER 4: Rapid production of bicontinuous macroporous materials using intrinsically polymerizable bijels

4.1 Introduction

Bicontinuous interfacially jammed emulsion gels, or bijels, are an emerging class of soft materials conceptualized in 2005 by Stratford et al.,[1] and later experimentally realized in 2007 by Herzig et al.[2] Bijels are typically formed by rapidly quenching a critical mixture of two partially miscible fluids into their miscibility gap, in the presence of near-neutrally wetting colloidal particles.[26] The rapid quench initiates de-mixing of the fluids by spinodal decomposition, while the near-neutrally wetting particles irreversibly adsorb to the fluid-fluid interface.[28] Eventually, the particles become jammed as a result of a reduction in fluid interfacial area, and de-mixing comes to a kinetic halt.[29] The resulting material, a bijel, is a solid-stabilized emulsion with bicontinuous morphology and weak gel-like mechanical properties.[18,22] Since their discovery, bijels have attracted considerable attention as templates for advanced materials synthesis, with applications ranging from cell delivery[15] and regenerative biomaterials[16] to electrochemical energy storage[8-10] and catalysis.[13] The main driver for this rapid surge in interest is twofold. First, inherent to the mechanism by which they are formed, bijels have a unique microstructure with desirable attributes at length scales relevant to the applications mentioned above.[3] Particularly, they comprise a bicontinuous, tubular arrangement of two fluid phases with a uniform and tunable characteristic domain size, and a continuous interface with predominantly negative Gaussian curvatures (akin to saddle points) separating the two phases.[30] These morphological characteristics are particularly attractive in

applications that require transport of different species, reactants, ions, redox agents, cells, nutrients, drugs, or other materials throughout the structure, to drive their desired function.[77,97] Second, because bijels are formed by a thermodynamically-driven de-mixing process, materials synthesis techniques based on bijel templating are inherently amenable to scaleup.[9,14] In pursuit of utilizing the unique morphology of bijels for technological applications, Lee and Mohraz developed a robust method to chemically solidify and lock in their three-dimensional (3D) microstructure, transforming them into near-uniform macroporous functional materials bearing the beneficial morphological attributes of their parent bijels.[17] This invention paved the way for the utility of bijels in the applications mentioned above to be demonstrated. However, a significant shortcoming of Lee's method is that polymer precursors, such as liquid monomers or oligomers, must be introduced into one of the continuous fluid domains by selective mass transfer, after the bijel is formed. This key intermediate step presents the following issues and challenges. First, it makes the process quite time-consuming: while a bijel typically takes a few seconds to form, replacing one of the fluid phases with a monomer solution can take several hours. Further, relying on mass transfer kinetics for this step puts limits on the dimensions and geometries of bijel-templated materials (BTMs) that can be synthesized. Finally, introduction of a third component (monomer solution) can impose interfacial or gravitational stresses within the system, which in turn can alter the bijel microstructure or result in its complete breakdown during the solvent-monomer exchange process.[18,98]

To overcome these issues, here we introduce an alternative bijel processing route, using intrinsically polymerizable bijels (IPBs) comprising partially miscible

76

mixtures of a solvent and a monomer. Upon quenching such a mixture into its miscibility gap, the fluids separate into monomer-rich and monomer-poor phases.[99] The use of a reactive monomer in the mixture's original chemical makeup preconditions the bijel with crosslinking compounds and avoids the need for monomer infiltration. Bijels made from solvent and monomer mixtures are readily transformable into BTMs via selective photo-polymerization of their monomer-rich phase in the presence of a photoinitiator with strong affinity for this phase. To achieve full selectivity in polymerizing the monomer-rich phase, we implement local photon quenching by a fluorescent dye with preferential solubility into the monomer-poor phase. Our method relaxes all the constraints of Lee's method for bijel-based materials synthesis, provides a means for their large-scale production, and thereby opens the door for bringing the applications of these emerging materials to fruition.

Three IPB systems are presented to demonstrate the generality of our approach, and the ability to tune the mechanical properties of the resultant porous materials via their chemical makeup. The first system is a mixture of 1,4-butanediol (BD) and a difunctional monomer, poly(ethylene glycol) diacrylate (PEGDA, M_n: 250 g/mol). The second system is a mixture of propylene glycol (PG) and a trifunctional monomer, trimethylolpropane ethoxylate triacrylate (TMPETA, M_n: 692 g/mol). A third system comprising a blend of two different monomers will be discussed in the context of mechanical property modulation. For this, a monofunctional monomer, methoxy poly(ethylene glycol) monoacrylate (MPGA, M_w: 350 g/mol), is added to replace a fraction of the PEGDA in the BD/PEGDA mixture. Three-point flexural testing demonstrates similar trends between the mechanical properties of BTMs and

those of bulk solid samples prepared with their respective monomers. These results show how the mechanical properties of BTMs can be systematically modulated by using a mixture of two different monomers and changing their relative amounts.

4.2 Results and Discussion

4.2.1 Phase behavior

Development of bijels with new chemistries requires complete mapping of the phase diagram and miscibility limits of their candidate fluids.[2] This information is important for the following reasons. First, to ensure bicontinuity, the pathway to phase separation should minimize the likelihood of droplet nucleation during de-mixing.[100] This is typically achieved by instigating a rapid change in the mixture's thermodynamic state (either temperature or composition), from miscible conditions to deep within its miscibility gap. Knowledge of the mixture's critical point is key to ensuring that this pathway can bypass the nucleation and growth region of the phase diagram. Second, the shape, and particularly symmetry, of the phase diagram dictates the volumetric ratio of the fluid phases upon de-mixing. This parameter plays an important role in the formation of bijels: volumetric ratios significantly deviating from 1:1 will influence the interfacial curvatures, which can in turn complicate particle packing, induce additional stresses at the fluid-fluid interface, and pinch off the bicontinuous domains or even break them up into discrete droplets.[101,6,102] To this end, we assembled a simple thermometer-coupled turbidity meter and experimentally determined the phase boundaries of our three IPB systems.[103] Fig. 4.1a depicts a schematic of the turbidity meter setup, which is based on measuring

78

light transmission through the mixture at different temperatures, as detailed in Section 4.2. We defined the cloud point, or phase transition temperature, as the temperature at which light transmission dropped below 95% of its maximum value at zero turbidity (i.e., when the formation of fluid-fluid interfaces resulted in at least 5% scattering of the incident beam).[104] It must be noted that the locus of the phase boundary identified by this method is not very sensitive to the chosen scattering threshold. This was ascertained by observing that the transmitted light intensity drops dramatically over a narrow temperature range (see Fig. S4.1). For each mixture, the cloud points were measured at various compositions to construct a binary phase diagram (plotted in Fig. 4.1b and 4.1c), and the mixture's upper critical solution temperature (UCST) was identified as the maximum point on the concave down phase boundary.[21] Notably, all three fluid systems have a UCST below 50 °C, easily accessible in simple laboratory settings. The critical compositions for the BD/PEGDA and BD/(PEGDA/MPGA) systems are both 47.5 vol% BD, with UCSTs of 48.7 °C and 46.3 °C, respectively. Because the phase boundaries represent equilibrium conditions governed by the chemical potential of the different constituents,[100] deliberately choosing chemically alike monomers and replacing only a small amount of PEGDA with MPGA (PEGDA:MPGA, volume ratio = 90:10) would not significantly alter the phase behavior. This is further corroborated by the similarly shaped binodal curves and the same critical composition between the two systems. Importantly, this enables blending a third, chemically similar, component into a binary IPB system, as a facile route for fine-tuning the mechanical properties of BTMs (detailed in Section 2.5) without the need to re-map the phase diagram for every new composition. The

symmetric phase diagrams observed in Fig. 4.1b are advantageous to bijel formation, because the mixtures de-mix into near-equal volume domains.[2,21] For the PG/TMPETA system (Fig. 4.1c), the critical composition is 72.2 vol% PG with a UCST of 29.5 °C. Because of its asymmetric binodal curve, spinodal decomposition at the critical composition will result in fluid domains of considerable disparate volumes in this system, which is not ideal for bijel formation.[28] Nonetheless, Bai et al. have demonstrated a method to induce spinodal decomposition in an off-critical mixture by applying a deep quench that bypasses droplet nucleation.[29] Similarly, we formed PG/TMPETA IPBs using an off-critical quench (at 58.5 vol% PG) that de-mixed into near-equal volume domains. The color coding used for the symbols in Figures 1b and 1c will be utilized throughout the chapter to differentiate the three different systems.
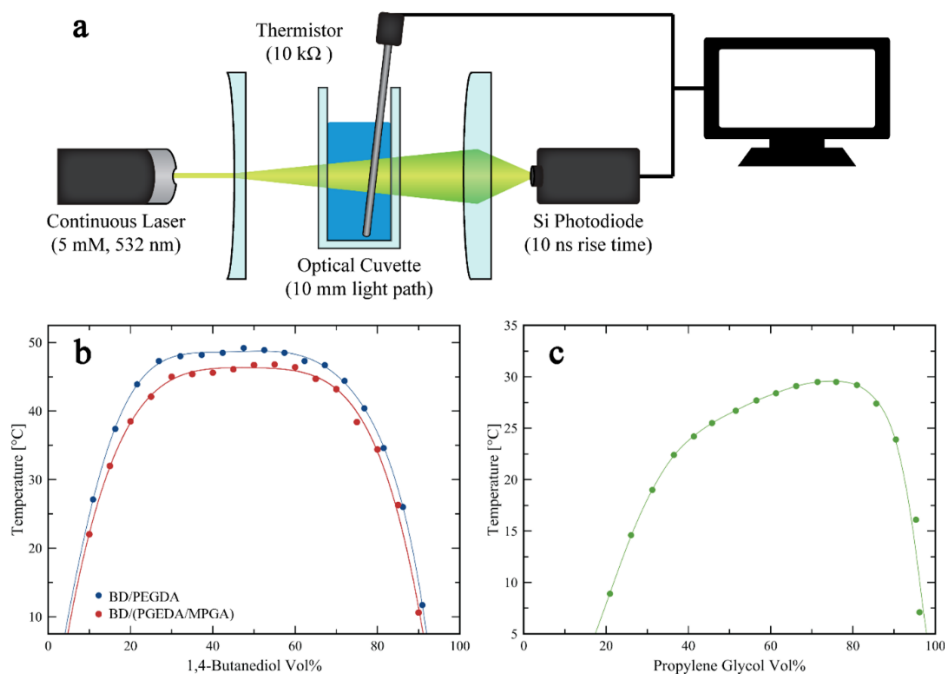

Fig. 4.1 Determination of IPB phase behavior. (a) A schematic of the turbidity meter setup used for cloud point measurements. Phase diagrams for the (b) BD/PEGDA, BD/(PEGDA/MPGA), and (c) PG/TMPETA fluid mixtures.

4.2.2 Formation of IPBs

Previous bijel studies have shown that near-neutrally wetting particles can be fabricated by surface modification of silica nanoparticles (SNPs).[21,23,105] We employed a similar process to synthesize fluorescently tagged SNPs with an average diameter of 200 nm and a coefficient of variance of 8.7%, as measured by scanning electron microscopy (SEM).[106] To render the SNPs near-neutrally wetting, they were treated with hexamethyldisilazane (HMDS) to decorate their surfaces with hydrophobic trimethylsilyl groups (i.e., adding methyl groups to the surface),[49] thereby resulting in a change of particle wettability with respect to the solvent and monomer fluids.[107] For any tested IPB mixture, SNPs treated with too much or too little HMDS became too hydrophobic or too hydrophilic, respectively, to sustain a net-zero curvature at the fluid-fluid interface.[6] These non-optimal SNPs preferentially wetted one phase and imparted curvature on the interface to produce discrete droplets.[28,108] For each IPB system, the appropriate HMDS/particle ratio (detailed in Section 4.3) was determined experimentally through systematic variations until near-neutrally wetting conditions were met, marked by successful bijel formation.[21]

To form BD/PEGDA and BD/(PEGDA/MPGA) bijels, near-neutrally wetting SNPs were dispersed in their respective critical mixtures at 70.0 °C and quenched by placing samples in direct contact with an aluminum heat sink at 22.5 °C. Fig. 4.2a and 4.2b display confocal laser scanning microscopy (CLSM) images of these IPBs stabilized with 1 vol% SNPs. The bright regions in these images correspond to the fluid-fluid interfaces laden with fluorescently tagged SNPs. The bicontinuous and

near-uniform fluid domains in these images confirm successful bijel formation. Interestingly, although PEGDA and MPGA are

chemically similar, SNPs that formed bijels in the BD/PEGDA system failed to stabilize a BD/(PEGDA/MPGA) IPB, and vice versa. This outcome suggests that a small substitution of PEGDA with MPGA alters the three-phase contact angle, and the surface treatment of the SNPs must be adjusted to compensate for this variation.[109] As mentioned earlier, PG/TMPETA IPBs were made by quenching off-critical mixtures, which we found was necessary for successful bijel formation. If, instead, a critical mixture of PG/TMPETA was used, CLSM recordings of the de-mixing process revealed phase separation by droplet nucleation (CLSM frames shown in Fig. S4.2, where a fluorescein dye, which selectively partitions into the PG-rich phase, was added to the mixture to help visualize the de-mixing process). This result concurs with previous simulations of critical quenching in a fluid mixture with an asymmetric phase diagram, which predicted a transition to discrete droplet formation, and loss of bicontinuity.[101,102] We tested various combinations of fluid composition and quenching temperatures, and observed bicontinuous phase separation when a mixture containing 58.5 vol% PG was quenched from 35.0 to 15.0 °C. This pathway enabled the formation of PG/TMPETA IPBs, as shown in Fig. 4.2c, and represents an atypical instance of bijel formation by quenching an off-critical mixture to a relatively shallow depth within its miscibility gap.[23]

The coarsening process of spinodal decomposition in simple liquid mixtures is governed by the interplay between surface tension and fluid viscosities.[100] Asymmetry in molecular dynamics between the fluids, if present, can result in
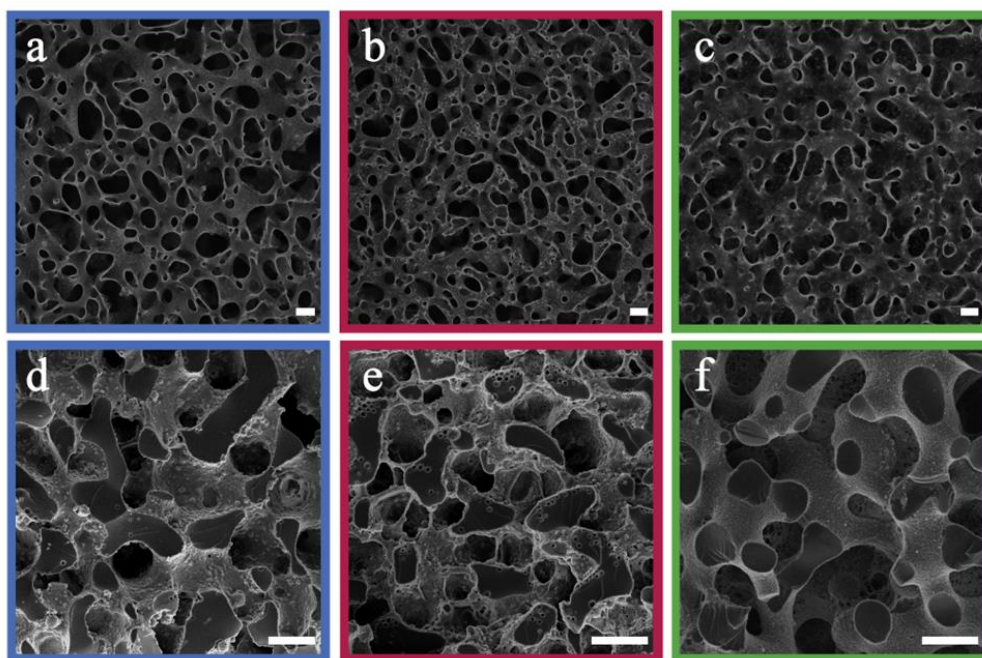
Fig. 4.2 Microstructural characterization of IPBs and BTMs. Fluorescence CLSM images of (a) BD/PEGDA, (b) BD/(PEGDA/MPGA), and (c) PG/TMPETA IPBs. SEM images of BTMs processed using (d) BD/PEGDA, (e) BD/(PEGDA/MPGA), and (f) PG/TMPETA IPBs. Scale bar = 40 μm. The frame colors correspond to the color coding used for the three systems throughout the chapter.

viscoelastic effects and unusual phenomena such as phase inversion or formation of a sponge-like network.[110,111] Such disparity in physical and molecular properties is often linked to the appearance of an asymmetrical binodal phase diagram, akin to the PG/TMPETA mixture presented in Fig. 4.1c.[112] Recently, Zhang et al. simulated thermally induced phase separation of a mixture with a highly asymmetric phase diagram that resulted in asynchronous growth between the two phases, giving rise to a morphological evolution pattern of droplets coalescing to form a bicontinuous network.[113] We therefore speculate that our off-critical quenches in the PG/TMPETA mixture may have initiated nucleation of droplets in the early stage of separation, which subsequently evolved into a percolating network with bicontinuous properties, similar to the mechanism proposed by Zhang et al. Determining the exact phase

separation pathway in this case is beyond the scope of the current study. Nonetheless, our results demonstrate successful formation of bijels in the three tested mixtures, enabled by careful tuning of particle wettability and pathway to phase separation in each system. Note that similar unusual kinetics have been predicted in fluid mixtures exhibiting significant differences in domain volumes or shear viscosities between the two phases.[114-117] Therefore, solvent/monomer mixtures that inherently involve ingredients of drastically different molecular weight or interactions may invoke unusual phase separation phenomena, and alternative pathways to bicontinuous phase separation, such as the off-critical quenching implemented here, should be considered in developing new IPB systems.

4.2.3 Photo-polymerization of IPBs

Fig. 4.3 represents a schematic comparison between Lee's bijel processing technique and our new IPB approach. To achieve selective templating, Lee exposed a bijel to a liquid mixture of monomer and photoinitiator that would selectively partition into one of the bijel fluid phases, typically requiring several hours (~4 hr) to complete, by far the longest step in the whole process, with the rest of the steps taking only a few minutes combined (Fig. 4.3a).[17] This procedure also puts practical limits on the geometries in which BTMs can be formed. Our IPBs are preconditioned with reactive monomers within one of the fluid phases, which are immediately polymerizable using a photoinitiator (Fig. 4.3b). By eliminating the monomer infiltration step, the geometry and dimensions of the BTMs are restricted only by the heat transfer rate for IPB formation (a rapid temperature change is required to initiate spinodal decomposition, as discussed previously).[26] However, an unwelcome
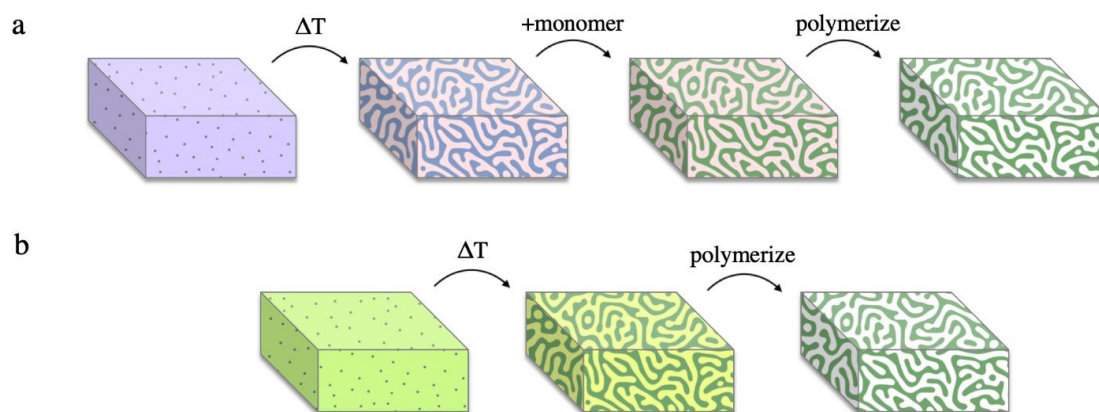
Fig. 4.3 Schematic representation of bijel processing techniques using (a) solvent/solvent bijels and (b) IPBs. (a) A solvent/solvent bijel is formed via a temperature quench. Monomer and photoinitiator with selective miscibility are added to infiltrate one phase of the bijel. After several hours, the monomer is polymerized to form a BTM. (b) An IPB preconditioned with a photoinitiator and a photon quencher is formed via a temperature quench and the monomer-rich phase is immediately polymerized to form a BTM.

consequence of bijel formation using a monomer/solvent mixture is that the monomer-poor phase still contains a finite concentration of monomer, which can negate selective polymerization of the monomer-rich phase. For example, the BD/PEGDA phase diagram (Fig. 4.1b) indicates that the monomer-poor phase of a critical mixture at 22.5 °C contains 12.4 vol% PEGDA. Our initial attempts to create a BTM from such a sample by incorporating 2,2-dimethoxy-2-phenylacetophenone (DMPA) as photoinitiator and exposing the IPB to ultraviolet (UV) light (wavelength, λ = 320-390 nm) resulted in a polymerized monomer-rich phase and a partially-polymerized monomer-poor phase (see Fig. S4.3). A potential resolution could be to widen the mixture's miscibility gap via a deeper temperature quench, further reducing the monomer concentration within the monomer-poor phase.[99] To emulate this process, we extrapolated the BD/PEGDA binodal curve to -22.0 °C, well below the freezing point of BD, and determined the monomer concentration to be approximately 3 vol% PEGDA. A mixture of BD/PEGDA at 3 vol% PEGDA was then prepared and

exposed to UV in the presence of photoinitiator, which still resulted in the formation of a loose polymer network. Therefore, we deemed this deep quenching strategy not viable for achieving selective polymerization in our systems.

To prevent polymerization within the monomer-poor phase, we implemented the following procedure. Sodium fluorescein, a hydrophilic fluorescent dye, and DMPA, a hydrophobic UV-activated photoinitiator, were chosen for their respective preferential solubilities in the monomer-poor and monomer-rich phases of the three tested IPBs. For each IPB system, sodium fluorescein (0.1 mM) was dissolved in the pure solvent liquid, and DMPA (1.0 mM) was dissolved in the pure monomer liquid, before combining the two solutions. Upon de-mixing, fluorescein and DMPA selectively partitioned into the monomer-poor and monomer-rich phases, respectively. The IPBs were subsequently exposed to UV light to initiate polymerization. Within the monomer-poor phase, fluorescein molecules absorbed the incident UV light and emitted visible light (λ = 460-670 nm), in effect locally quenching the UV photons and suppressing partial polymerization in this phase by limiting UV-activation of the photoinitiator. Meanwhile, the monomer-rich domains were polymerized to produce BTMs. Fig. 4.2d-f display SEM images of BTM cross-sections, showing macroporous and spinodal-like structures across all three samples.[8,26] Utilization of IPBs with local photon quenching circumvents the time-consuming monomer infiltration process and enables rapid selective polymerization to produce macroporous BTMs within a total of two minutes, as opposed to ~4 hr via the original Lee method.

4.2.4 Characterization of photon quenching

To quantitively demonstrate the preferential partitioning of fluorescein and DMPA, and their competitive absorption of UV light, we performed a series of spectrophotometry experiments (detailed in Section 4.5) to determine the partition coefficients and the UV-absorbances of each additive within the two phases of the BD/PEGDA and PG/TMPETA IPBs. The partition coefficient is determined by the relative solubilities of additives between the two bijel phases ($C_{solvent}/C_{monomer}$), which varies primarily with temperature and the compositions of the two fluid phases.[118] For the following discussion, spectrophotometry analyses (summarized in Table 1) were conducted to illustrate the behavior of the chemical additives at concentrations corresponding to the polymerization process described in the previous section. The partition coefficient of fluorescein within the BD/PEGDA mixture is 2.55, indicating that fluorescein expresses affinity toward the monomer-poor phase in this system. This affinity is much greater in the PG/TMPETA mixture, where the partition coefficient is 94.72. Conversely, the partition coefficients for DMPA within both IPB systems are of order 10^{-3}, indicating strong affinities for their respective monomer-rich phases. We then calculated the UV-absorbances (λ = 350 nm) of the partitioned fluorescein and DMPA. In each IPB system, the concentrations of the additives within the monomer-poor phase were calculated based on the partition coefficients and then multiplied by the experimentally measured molar extinction coefficients (detailed in Section 4.5) and the bijel characteristic domain size (34 µm, determined from confocal microscopy images) to obtain the reported UV-absorbance values. Although these

values correspond to different concentrations, they are reflective of the photoactivity within the two phases of the IPBs during the polymerization process. In both IPBs, the UV-absorbance values for fluorescein within the monomer-rich phases are two orders of magnitude larger than those of DMPA, showing that fluorescein competitively interacts with, and absorbs, the incident UV light. The fluorescence and absorption spectra of fluorescein and DMPA, respectively, dissolved in the monomer-poor phases of the three different systems are plotted in Fig. 4.4. The mismatches between the emission ranges (λ = 460-670 nm) of fluorescein and the absorption ranges of DMPA ($\lambda < 390$ nm) establish a quenching effect where the activation of DMPA is curtailed by lowering the local UV intensity. Based on our findings, we attribute the effectiveness of our selective polymerization strategy to the partitioning and relative concentrations of additives, fluorescein's competitive absorption of UV light, and its fluorescence effect.

Table 4.1 Summary of spectrophotometry results.

IPB system	Partition Coefficient		UV-Absorbance*	
	Fluorescein	DMPA ($\times 10^{-3}$)	Fluorescein ($\times 10^{-4}$)	DMPA ($\times 10^{-6}$)
BD/PEGDA	2.55	3.92	8.44	3.57
PG/TMPETA	94.72	5.74	4.96	3.42

*Absorbance values were calculated using the concentrations of the partitioned additives: 0.14 mM fluorescein in BD-rich phase, 0.25 mM fluorescein in PG-rich phase, 1.87 mM DMPA in PEGDA-rich phase, and 1.63 mM DMPA in TMPETA-rich phase.
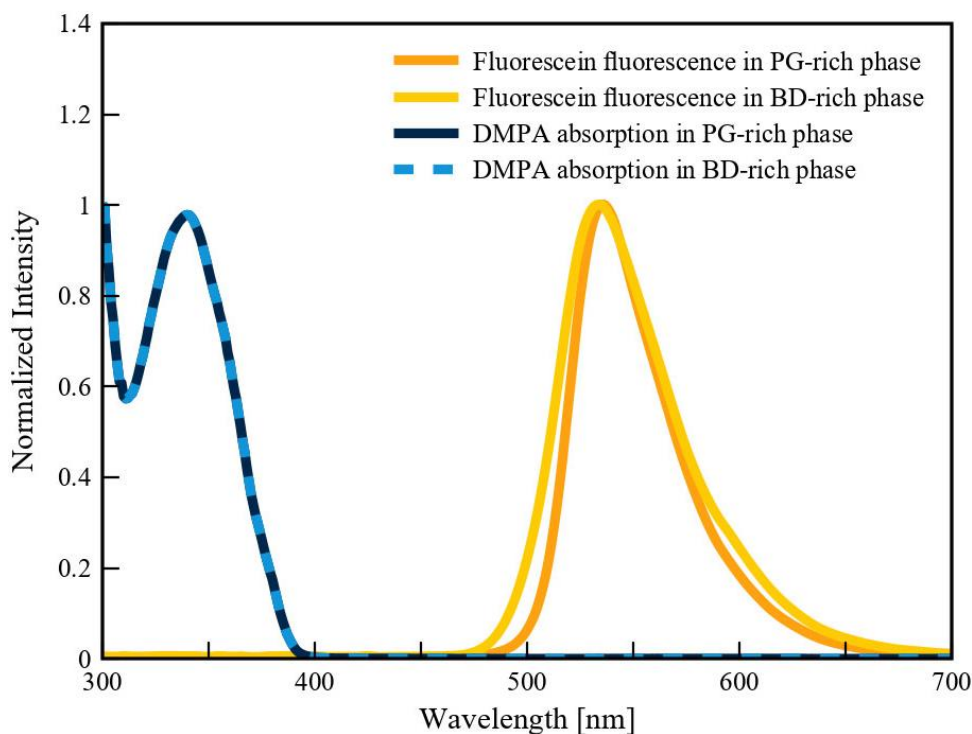
Fig. 4.4 Fluorescence (λ_{ex} = 350 nm) and absorption spectra of fluorescein and DMPA in BD-rich and PG-rich phases. Each spectrum was normalized by the maximum recorded intensity value for each respective test.

4.2.5 Modulating the mechanical properties of BTMs

In this section we demonstrate the ability to modulate the chemical makeup and thereby the properties of BTMs, using different monomer fluids that have comparable miscibility gaps with a given solvent, such as those shown in Fig. 4.1b. While we demonstrate this in the context of mechanical properties, our intent is to establish a general approach for expanding the chemical library of IPBs and the desired characteristics of BTMs derived from them, using monomer or oligomer blends. Three-point bending tests were conducted to measure the flexural moduli of the BTMs and bulk control polymers. BTMs were prepared with 1 vol% SNPs to produce macroporous materials with similar characteristic domain sizes (25-28 μm,

as determined from SEM images).[2] Control bulk polymer samples were prepared by UV-polymerization of the monomer-rich fluids, prepared as a single phase. The BTMs and bulk polymer samples were cut into rectangular coupons and bent using a custom three-point bending test fixture attached to a mechanical tester (see Section 4.6 for details). The average flexural moduli of BTMs and bulk polymer samples are presented in Fig. 4.5. As expected, the macroporous BTMs exhibited lower flexural moduli than their bulk polymer counterparts, which can be attributed to their porosity.[31] Materials derived from the BD/PEGDA mixture exhibited the highest flexural moduli among the three different chemistries tested, while those derived from the PG/TMPETA mixture exhibited the lowest. For crosslinked poly(ethylene glycol), the stiffness of the polymer increases as crosslinking density increases.[119] PEGDA is a short-chain difunctional monomer that polymerizes to form a dense network of highly crosslinked poly(ethylene glycol).[120] In contrast, TMPETA is a larger trifunctional monomer, resulting in a sparser polymer network with a lower degree of crosslinking, hence a more flexible material. As discussed earlier, we take advantage of the relatively similar phase diagrams shown in Fig. 4.1b to create IPBs with a blend of functional monomers, thereby adjusting the crosslink density of the resultant polymer. For this, 10 vol% of the PEGDA in the BD/PEGDA IPB was replaced by a higher molecular weight mono-functional monomer MPGA, which reduced the number of crosslinkable groups and introduced pendent poly(ethylene glycol) chains within the polymer network, resulting in a lower degree of crosslinking.[121] This effect is evidenced by the decreased flexural moduli of the materials derived from the BD/(PEGDA/MPGA) mixture relative to those derived from BD/PEGDA. Overall,

flexural testing shows a similar trend between the moduli of the bulk polymers and

BTMs, affirming that our approach enables facile tuning of the crosslink density in
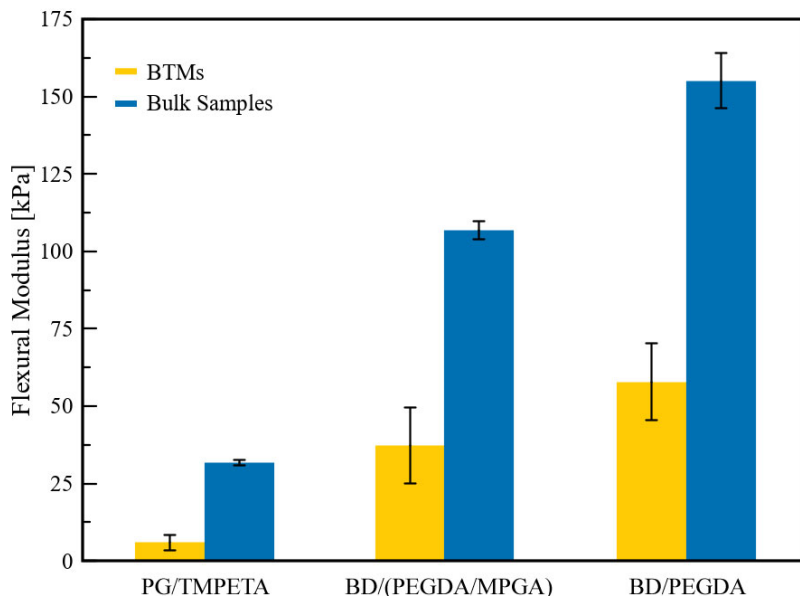
Fig. 4.5 Three-point flexural testing results for BTMs and bulk polymer samples. Error bars represent standard deviation (n = 4,4,6).

BTMs by using monomer blends in the original IPB formulations.

4.3 Conclusions

We established a general two-step approach to produce BTMs that circumvents

a number of limitations in existing protocols. IPBs were formed via the kinetic arrest

of thermally induced spinodal decomposition in partially miscible mixtures of solvent

and monomer fluids. The use of a reactive monomer within the bijel formulation

preconditions one fluid phase with a polymerizable compound, averting the time-

consuming process of monomer infiltration, as well as relaxing the geometric

restrictions associated with this step. Selective polymerization of the monomer-rich

phase was made possible by premixing a photoinitiator and a photon quencher with

disparate affinities for the two fluid phases, and exposing to UV light to initiate

localized polymerization. The resulting BTMs exhibited a morphological resemblance to their IPB templates. By changing the formulation of the monomer-rich phase, we demonstrated a technique to modulate the mechanical properties of BTMs. Our IPB and photon quenching methods are amenable to scalable manufacturing processes. Furthermore, application of our IPB approach to different monomers yields BTMs with tunable mechanical and chemical properties, important design parameters for future research and development of advanced biomedical devices, metallic scaffoldings, or mechanical support materials for electrodes.

4.4 Materials and methods

4.4.1 Materials

The following materials were used as received. 1,4-butanediol (BD, 99%), propylene glycol (PG, ≥99.5%), poly(ethylene glycol) diacrylate (PEGDA, M_n: 250 g/mol), trimethylolpropane ethoxylate triacrylate (TMPETA, M_n: 692 g/mol), 2,2-dimethoxy-2-phenylacetophenone (DMPA, 99%), fluorescein isothiocyanate isomer I (FITC, ≥90%), and tetraethyl orthosilicate (TEOS, ≥99.0%) were purchased from Sigma-Aldrich. Hexamethyldisilazane (HMDS, 98+%) was purchased from Alfa Aesar. Methoxy polyethylene glycol monoacrylate (MPGA, M_w: 350 g/mol) was provided by Sartomer USA. (3-aminopropyl) triethoxysilane (APTES, ≥98%) were purchased from TCI America. Sodium fluorescein salt was purchased from HiMedia. Anhydrous ethanol (200 proof) was purchased from Rossville Gold Shield. Strong ammonia (27-30%) was purchased from VWR. Deionized water was purified with a Milli-Q Advantage A10 water purification system (Millipore Sigma, 18.2 MΩ·cm at 25 °C).

4.4.2 Turbidity meter and cloud point measurement

Fig. 4.1a depicts a schematic of our turbidity meter set up. A generic continuous 5 mW 532 nm laser powered by a constant voltage (2.6 V) power supply emitted a constant power laser beam. A negative lens expanded the laser beam to increase the sampling area (~1 cm dia.), and a positive lens focused the transmitted light onto a silicon photodiode (ThorLabs, 400 ns rise time). The voltage across a load resistor within the photodiode circuit was measured and correlated to the intensity of the transmitted laser beam. The mixture temperature was measured using an immersion thermistor (Omega, 10 kΩ). For each cloud point measurement, a 7 mL mixture of solvent and monomer of known composition was added to a glass optical cuvette (Macro Cell, 10 mm light path), and subsequently heated while being stirred. The intensity of the light transmitted through the single-phase mixture was calibrated as the baseline transmittance. To determine the cloud point, a slow temperature ramp (-0.5 °C/min) was applied to the sample holder using a fluid bath heated cuvette holder; meanwhile, the temperature and voltage were recorded simultaneously using a myDAQ (National Instruments) acquisition device. Cloud points were determined when transmission intensity dropped below the 95% threshold. Binodal curves were generated by fitting the cloud point data with a Fourier series (number of harmonics = 3).

4.4.3 SNP synthesis

A silane-coupled fluorescein solution was prepared by mixing 8.0 mg of FITC, 33.8 μL of APTES, and 6.4 mL of anhydrous ethanol for 15 min. SNPs were synthesized using a modified Stöber method by mixing 1.0 mL of the FITC-APTES solution, 8.0 g of

ethanol, 1.0 mL of deionized water, 680 µL of TEOS, and 295 µL of strong ammonia solution, and stirring at room temperature for 4.5 hr.[122] After this, HMDS (250 µL for BD/PEGDA IPBs, 160 µL for BD/(MPGA/TMPETA) IPBs, or 80 µL for PG/TMPETA IPBs) was added directly to the reaction vial and stirred for another 18 hr at room temperature. Particles were washed by repeated centrifugation and resuspension in ethanol, then subsequently dried in a 75 °C vacuum oven for 1 hr.

4.4.4 BTM preparation and imaging

IPBs were prepared by combining SNPs, solvent solution (0.1 mM sodium fluorescein), and monomer solution (1.0 mM DMPA) in 1.5 mL centrifuge tubes. An ultrasonic horn (Branson Ultrasonics) was used to disperse the SNPs, also heating and mixing the fluids. The dispersions were transferred to a custom disk-shaped sample holder made of two glass coverslips and a 3 mm spacer. IPBs were formed by placing the sample holders onto an aluminum heat sink conditioned to the quench temperature (22.5 °C for BD/PEGDA and BD/(PEGDA/MPGA), 15.0 °C for PG/TMPETA). An inverted microscope coupled to a VT-Eye confocal scanner (VisiTech International) was used to examine the phase separation of the PG/TMPETA mixture. A FluoView 1200 CLSM system (Olympus) was used to examine the internal microstructure of the stabilized IPBs. An EXFO UV lamp (Lumen Dynamics) with a 320-390 nm bandpass filter was used to supply UV light to initiate polymerization. Samples were exposed to UV light for 30 s. The remaining fluids were subsequently removed with repeated ethanol washes and dried in a 70 °C oven. BTMs were cut using a surgical blade to expose a cross-sectional view of the internal microstructure. Before SEM imaging, the BTMs were dried in a 75 °C vacuum oven for

1 hr. An EM ACE600 sputter coater (Leica) was used to deposit an 8 nm iridium coating on the BTMs to minimize the degradation of polymer caused by the electron beam. A Magellan 400 XHR SEM (FEI) was used to obtain images of the BTMs.

4.4.5 Spectroscopy

A series of calibration experiments were conducted to determine the molar extinction coefficients of the fluorescein and DMPA within the monomer-poor phase of each IPB system. Stock solutions of the monomer-poor phase for each system were prepared by mixing IPB solvent/monomer pairs without adding SNPs, fluorescein, or DMPA, and quenching to the bijel formation temperatures to de-mix the fluids. The two resultant phases were separately extracted and loaded into different containers. Fluorescein (0.050-2.4 mM) and DMPA (0.0050-10.0 mM) calibration solutions were prepared by dissolving either sodium fluorescein or DMPA in the monomer-poor stock solutions. The prepared solutions were loaded into a 96-well plate and their UV-absorptions (λ = 320-390 nm, 10 nm increments) were measured using a SpectraMax M3 plate reader (Molecular Devices). For samples containing fluorescein, a UV-blue bandpass filter (Newport, 210-500 nm) was placed on top of the 96-well plate to filter out fluorescent light. The molar extinction coefficients for fluorescein and DMPA in the monomer-poor fluids were determined using the Beer-Lambert Law, $A = \varepsilon l C_i$, where A is the absorbance, ε is the molar extinction coefficient, l is the optical path length, and C is the concentration of the additive in fluid phase i. For each wavelength, the molar extinction coefficient (plotted in Fig. S4.4) was calculated by multiplying the optical path length by the slope of the absorbance vs. concentration graph.[123]

To determine the partition coefficients, fluorescein (0.050-2.4 mM) or DMPA (0.0050-10.0 mM) solutions were prepared by dissolving sodium fluorescein or DMPA in the pure solvent or monomer liquids, respectively. IPB mixtures without SNPs were prepared using either fluorescein or DMPA solutions and subsequently quenched to the IPB formation temperature to mirror the fluid phase separation and additive partitioning within the IPBs. The monomer-poor phases were extracted and loaded into a 96-well plate. UV-absorption tests were performed (λ = 320-390 nm, 10 nm increments) to measure the absorbances of the partitioned additives. The concentrations of fluorescein or DMPA in the monomer-poor fluids (shown in Fig. S4.5) were calculated using the measured extinction coefficients and the Beer-Lambert Law. The concentrations of additives within the monomer-rich phases were calculated through conservation of mass, $C_{mixture}\ V_{mixture} = C_{solvent}\ V_{solvent} + C_{monomer}\ V_{monomer}$, where C is the concentration, V is the volume, and the subscripts denote the fluid phases.[124] The relative volumes of the fluid domains within the IPBs were calculated using the Lever rule and the measured phase diagrams.[21]

The absorption and fluorescence spectra of fluorescein and DMPA were measured using 1.0 mM fluorescein solutions and 10.0 mM DMPA solutions prepared with the stock monomer-poor fluids described above. Absorption tests (λ = 300-750 nm, 1 nm increments) were conducted on the DMPA solutions. Fluorescence tests were conducted by exciting the fluorescein solutions with 350 nm UV light and recording the emitted light intensity for each wavelength (λ = 300-750 nm, 1 nm increments). Each spectrum was normalized by the maximum recorded value for each respective test.

4.4.6 Mechanical testing

Three-point bending tests were performed using an MTS Synergie 100 mechanical tester (MTS Systems) fitted with a custom bending fixture (support span of 10 mm). BTMs and bulk samples were prepared in a parallel plate sample holder made of two glass coverslips and a 1 mm spacer to produce sheets. The polymerized samples were cut into 8×15 mm rectangular coupons and bent to 10% strain. The flexural modulus was calculated as the slope of the initial linear portion of the stress-strain curve.

4.5 Supporting information
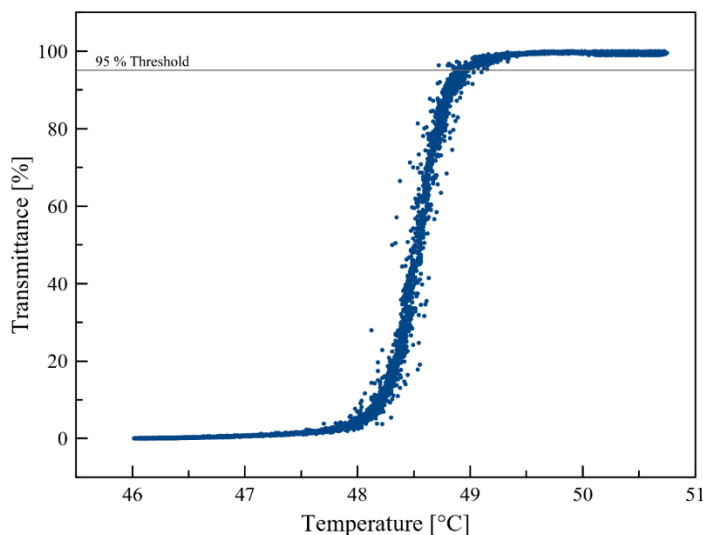
Fig. S4.1 Laser transmittance as a function of temperature of a 60/40 vol% BD/PEGDA mixture during a cloud point experiment. The horizontal line represents the 95% transmittance threshold for determining the phase separation temperature.
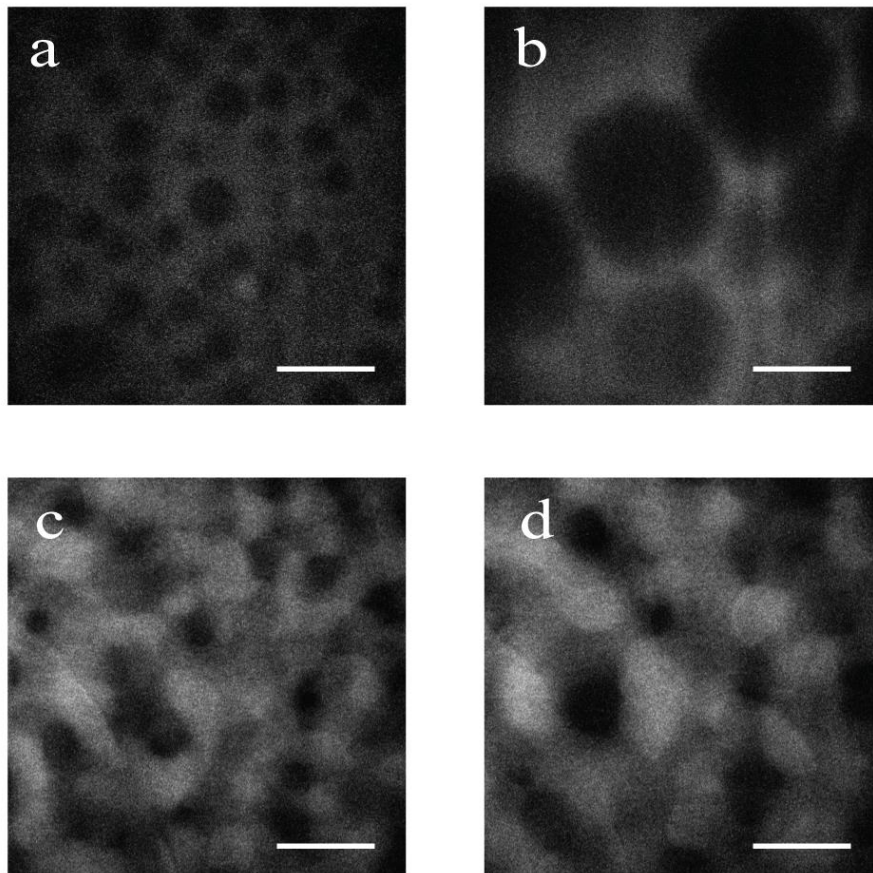
Fig. S4.2 CLSM frames of PG/TMPETA phase separation evolution. Sample (a-b) was quenched from 70.0 °C to 22.5 °C and sample (c-d) was quenched from 35 °C to 15.0 °C. The bright (fluorescein-tagged) fluid phase corresponds to the PG-rich phase in each image. (a-b) Droplet nucleation in a 72.0 vol% PG mixture. (c-d) Spinodal decomposition in a 58.5 vol% PG mixture. Scale bar = 40 µm.
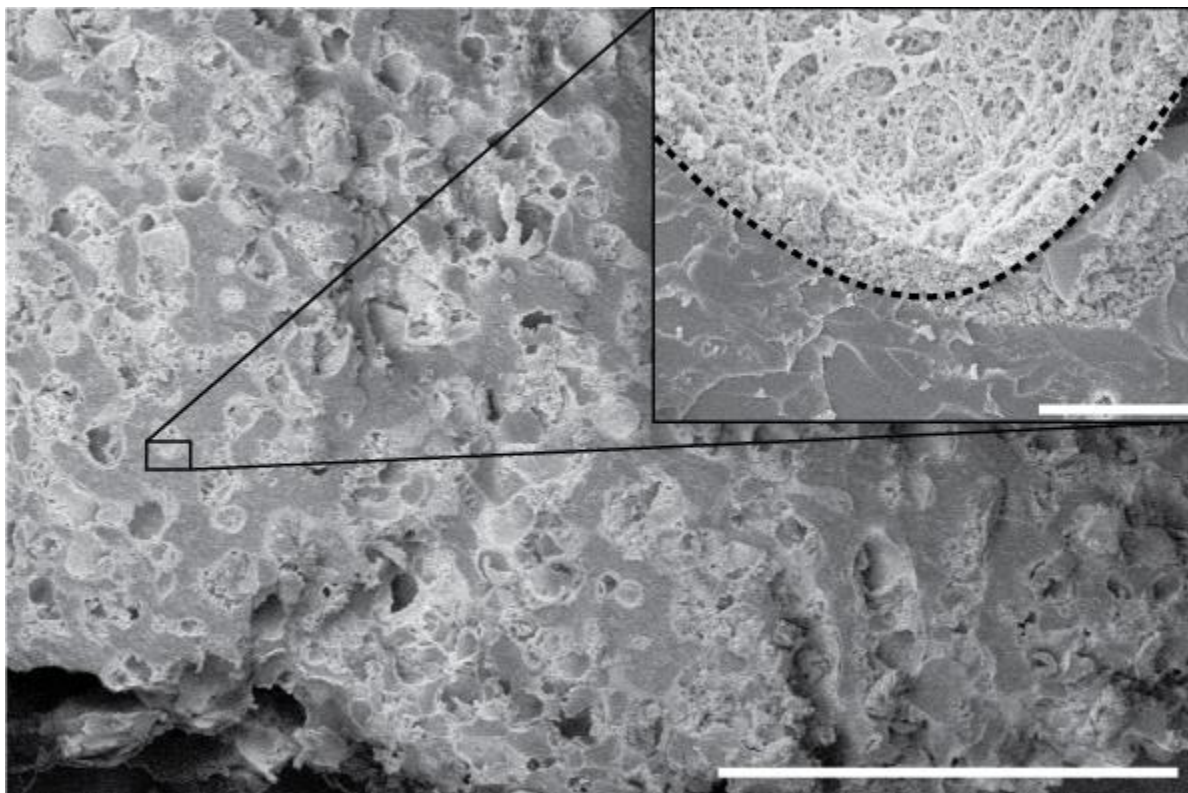
Fig. S4.3 SEM image of a BD/PEGDA BTM with a partially polymerized monomer-poor phase. Scale bar = 400 µm. Inset provides a high magnification view. The dashed line denotes the interface between the partially polymerized monomer-poor phase (above) and the polymerized monomer-rich phase (below). Scale bar = 10 µm.
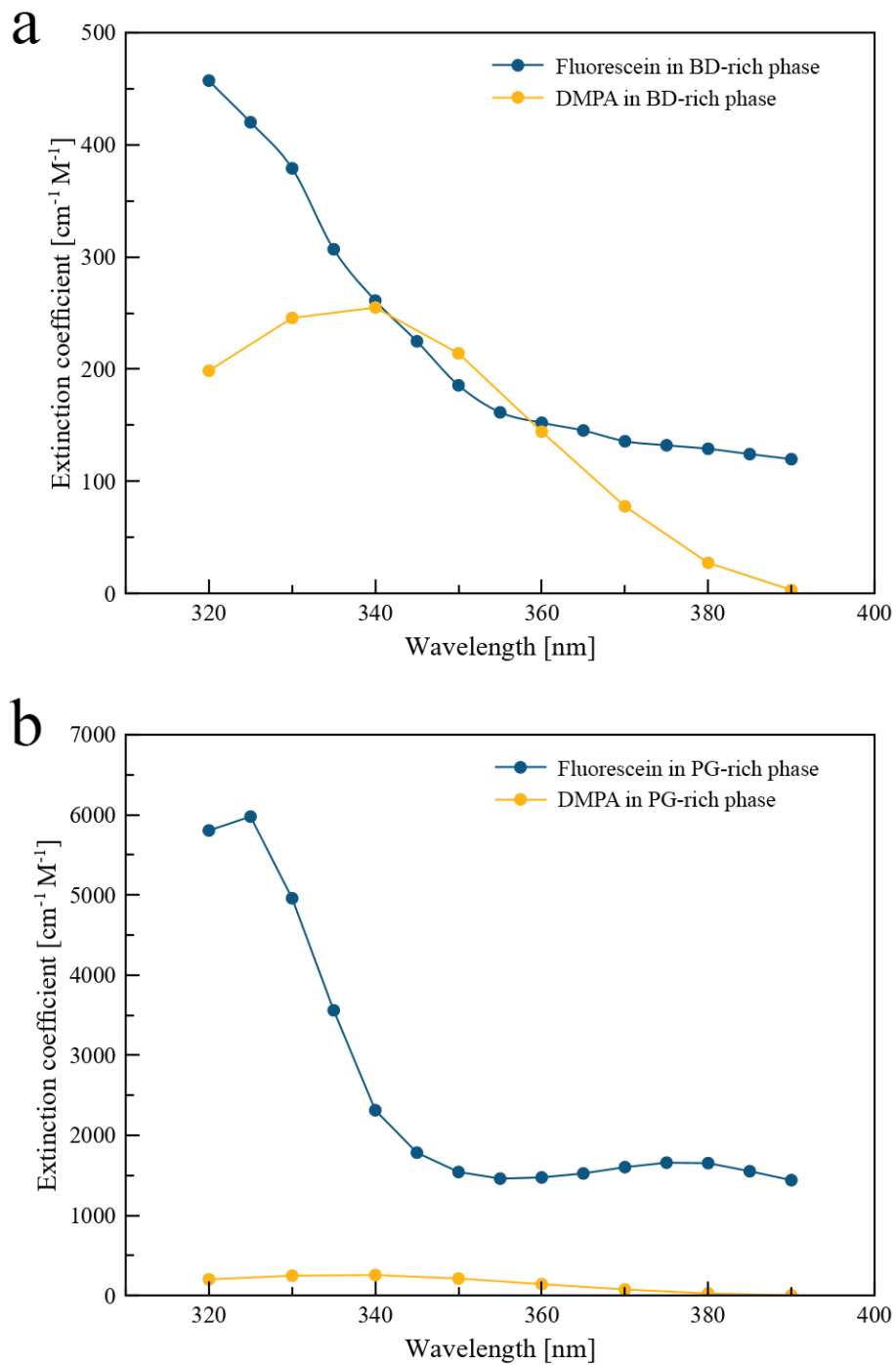
Fig. S4.4 Molar extinction coefficients as a function of wavelength for fluorescein (blue) and DMPA (yellow) dissolved in the (a) BD-rich phase extracted from BD/PEGDA mixtures at 22.5 °C and the (b) PG-rich phase extracted from PG/TMPETA mixtures at 15 °C. Data points were connected to guide the eye.
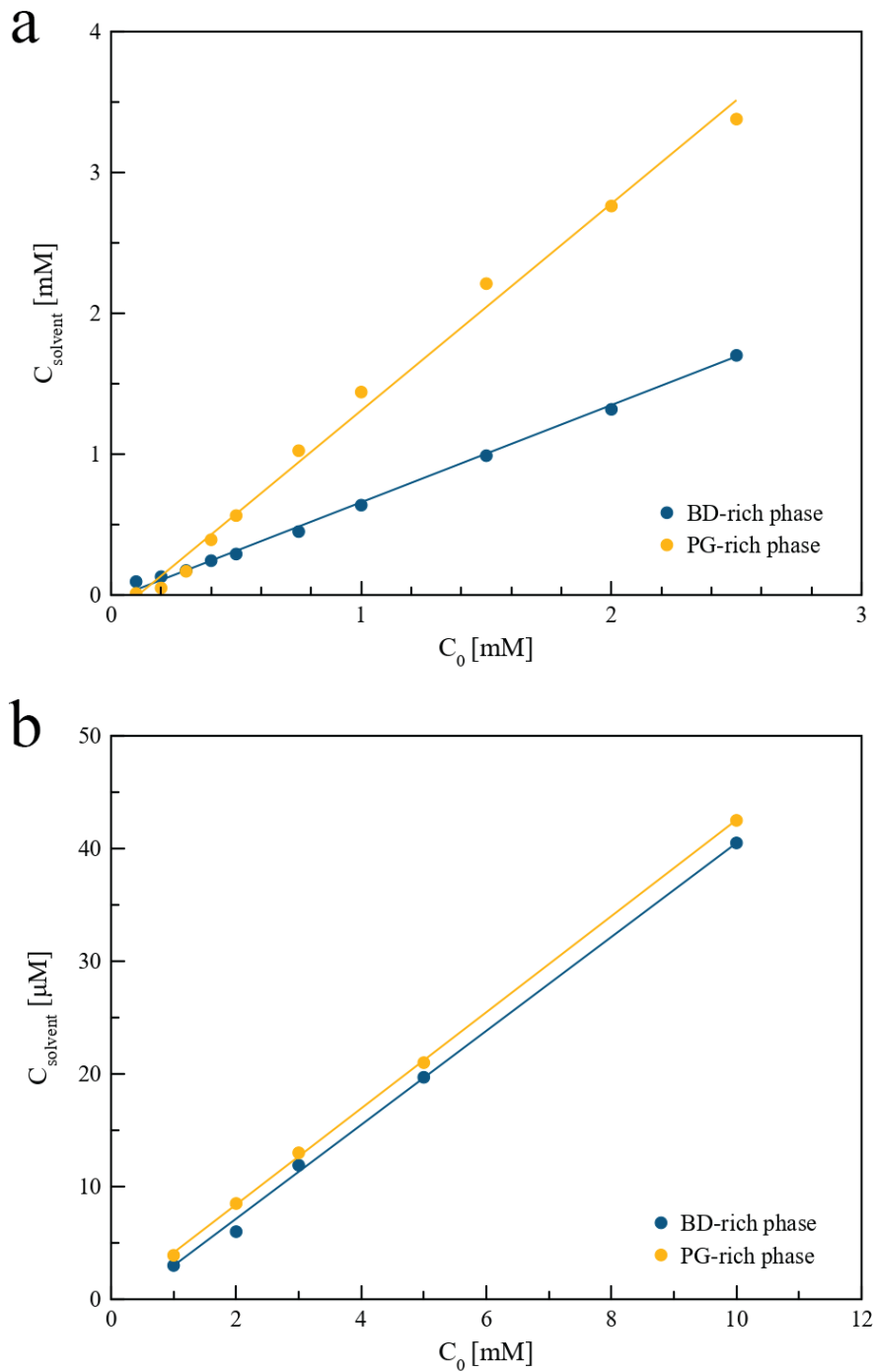
Fig. S4.5 Concentration ($C_{solvent}$) of (a) fluorescein and (b) DMPA partitioned to the BD-rich phase extracted from BD/PEGDA mixtures at 22.5 °C (blue) and the PG-rich phase extracted from PG/TMPETA mixtures at 15 °C (yellow) as a function of the initial concentration (C_0) of fluorescein or DMPA dissolved in the pure BD and PG fluids of the BD/PEGDA and PG/TMPETA mixtures, respectively. Lines were determined via linear least squares regression.

CHAPTER 5: Conclusion and future work

The origin of stability and yielding in bijels was investigated by conducting extensive rheological experiments. Examination of bijels under small amplitude oscillatory shear at different frequencies, temperatures, and volume fractions revealed glassy rheological behaviors reminiscent of Brownian-driven in-cage (β) and out-of-cage (α) dynamics in colloidal glasses. The glassy rheology combined with energetic approximations of interparticle attractions suggest particles are mobile along fluid-particle-fluid interface, and interfacial compaction by interfacial tension along provide sufficient mechanical rigidity for bijel stability. This conjecture was further tested via nonlinear rheology in which bijels were strain to intermediate strain at high shear rate to induce stretching of the interface. Close examination of the nonlinear response, as well as frequency sweeps at intermediate amplitudes reveal overall weakening of the shear moduli by large strain, indicative of strain softening behavior. Further, signatures of cage relaxation and un-jamming at intermediate strains were recorded, which are attributed to the in-plane particle rearrangement at the interface. Based on the experimental results, a nonlinear double Maxwell model was introduced to capture the gross features of the linear and nonlinear bijel rheology. The congruency between the rheology and the model further affirms that bijel rheology is dominated by the competition between α and β dynamics, and bijel exhibit remarkable ductility owing continuous interface which can recovered the jamming nature of the interface after deformation. Having gained a greater insight into the dynamics of the particle-interface layer, I presented a simple approach to template bijels into porous scaffolds with minimal disruption to the interface. For this,

photopolymerization bijels were prepared using mixtures of solvent and monomer precursor. Once formed, these bijels can be rapidly polymerized into polymeric scaffolds, avoiding the time-consuming process of monomer addiction which can introduce mechanical and/or chemical stresses to the interface.

In all the rheological investigation presented in this dissertation, the results are analyzed based on the assumptions that particles are mobile along the fluid interface. While all intuition and evidence point to the existence of α and β dynamics, direct observation of the particle dynamics remains a challenge. Direct correlation of the particle structure to nonlinear rheology of bijels can affirm the link between yielding and particle compaction along the interface. In my work, I have begun studying the individual particle motion by preparing bijels using two populations of silica nanoparticles dyed with different fluorescent dyes. Using a confocal microscope with two lasers of distinct wavelengths and careful manipulation of optics, I was able to obtain snapshots of the particles along the fluid interface within bijels. An example of the snapshot is shown in Fig. 5.1
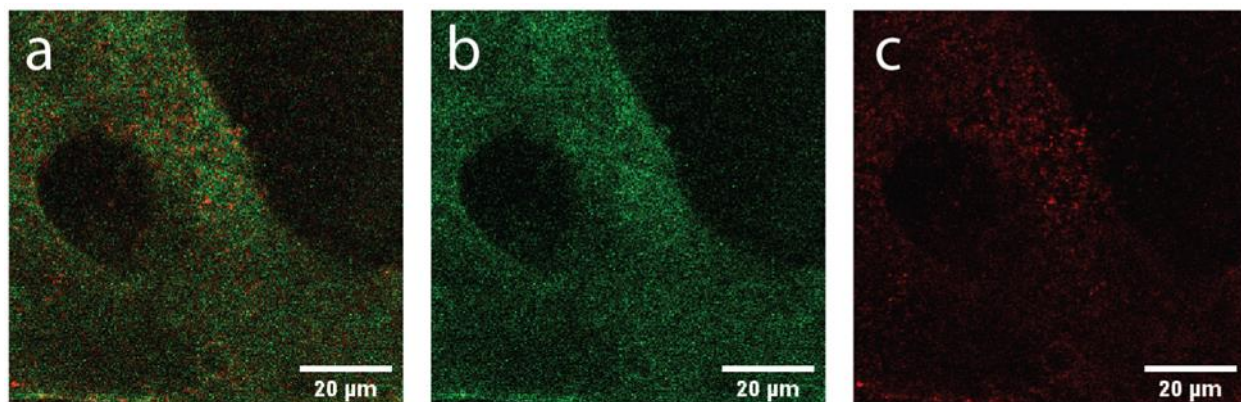

Fig. 5.1 High resolution confocal microscope snapshot of the interface within a bijel. Particles are dyed using two distinct fluorescent dye (illustrated as green and red). The bright pixels shown in b and c correspond to one population of the particles within the bijel.

If indeed bijels are colloidal glasses formed by compaction of the interface, it is likely that the rapid compaction results in imperfect packing and particles are trapped in a high disorganized 2D glassy state. As such, that majority of the particles bares the compaction load by being jammed together, and a subset of the particles are trapped within cages form by neighboring jammed particles. With high-speed and high-resolution microscopy and advance particle tracking techniques, I theorized that the particles along the interface can be tracked and bifurcated into two sub-population of mobile and immobile particles.

Confirmation of particle mobility will not only have implications for the applications of bijels, but also shed lights on other solid-stability emulsions with jammed interface. For instance, shearing of Pickering emulsion results in kinetically arrested droplets with anisotropic geometry, enabling routes for templating of droplets into microparticles with irregular shapes. Greater understanding of particle dynamics will aid designs and implementations of jammed emulsion templating. Likewise, bijels can be un-jammed by shear and self-rejuvenated into anisotropic domains. I theorized that the intrinsically polymerizable bijels presented in Chapter 4 can be mechanically deformed and re-jammed into anisotropic structure, and subsequently polymerized into a polymeric scaffolds with aligned unrestricting pores.

REFERENCES

1   K. Stratford, R. Adhikari, I. Pagonabarraga, J.-C. Desplat and M. E. Cates, *Science*, 2005, **309**, 2198–2201.
2   E. M. Herzig, K. A. White, A. B. Schofield, W. C. K. Poon and P. S. Clegg, *Nature Materials*, 2007, **6**, 966–971.
3   M. E. Cates and P. S. Clegg, *Soft Matter*, 2008, **4**, 2132–2138.
4   K. M. McDevitt, D. R. Mumm and A. Mohraz, *ACS Applied Energy Materials*, 2019, **2**, 8107–8117.
5   M. F. Haase, K. J. Stebe and D. Lee, *Adv. Mater.*, 2015, **27**, 7065–7071.
6   R. Aveyard, B. P. Binks and J. H. Clint, *Advances in Colloid and Interface Science*, 2003, **100–102**, 503–546.
7   M. N. Lee and A. Mohraz, *J. Am. Chem. Soc.*, 2011, **133**, 6945–6947.
8   M. N. Lee, M. A. Santiago-Cordoba, C. E. Hamilton, N. K. Subbaiyan, J. G. Duque and K. A. D. Obrey, *J. Phys. Chem. Lett.*, 2014, **5**, 809–812.
9   J. A. Witt, D. R. Mumm and A. Mohraz, *Journal of Materials Chemistry A*, 2016, **4**, 1000–1007.
10   D. Cai, F. H. Richter, J. H. J. Thijssen, P. G. Bruce and P. S. Clegg, *Materials Horizons*, 2018, **5**, 499–505.
11   M. A. Santiago Cordoba, J. S. Spendelow, A. N. G. Parra-Vasquez, L. A. Kuettner, P. M. Welch, C. E. Hamilton, J. A. Oertel, J. G. Duque, E. J. Meierdierks, T. A. Semelsberger, J. C. Gordon and M. N. Lee, *Adv. Funct. Mater.*, 2020, **30**, 1908383.
12   S. J. Gross, K. M. McDevitt, D. R. Mumm and A. Mohraz, *ACS Appl. Mater. Interfaces*, 2021, **13**, 8528–8537.
13   S. Cha, H. G. Lim, M. F. Haase, K. J. Stebe, G. Y. Jung and D. Lee, *Scientific Reports*, , DOI:10.1038/s41598-019-42769-8.
14   M. F. Haase, H. Jeon, N. Hough, J. H. Kim, K. J. Stebe and D. Lee, *Nature Communications*, 2017, **8**, 1234.
15   T. J. Thorson, E. L. Botvinick and A. Mohraz, *ACS Biomaterials Science & Engineering*, 2018, **4**, 587–594.
16   T. J. Thorson, R. E. Gurlin, E. L. Botvinick and A. Mohraz, *Acta Biomaterialia*, 2019, **94**, 173–182.
17   M. N. Lee and A. Mohraz, *Advanced Materials*, 2010, **22**, 4836–4841.
18   M. N. Lee, J. H. J. Thijssen, J. A. Witt, P. S. Clegg and A. Mohraz, *Advanced Functional Materials*, 2013, **23**, 417–423.
19   A. Maestro, *Current Opinion in Colloid & Interface Science*, 2019, **39**, 232–250.
20   K. A. White, A. B. Schofield, B. P. Binks and P. S. Clegg, *J. Phys.: Condens. Matter*, 2008, **20**, 494223.
21   J. W. Tavacoli, J. H. J. Thijssen, A. B. Schofield and P. S. Clegg, *Advanced Functional Materials*, 2011, **21**, 2020–2027.
22   L. Imperiali, C. Clasen, J. Fransaer, C. W. Macosko and J. Vermant, *Materials Horizons*, 2014, 7.
23   L. Bai, J. W. Fruehwirth, X. Cheng and C. W. Macosko, *Soft Matter*, 2015, **11**, 5282–5293.

24 K. A. Rumble, J. H. J. Thijssen, A. B. Schofield and P. S. Clegg, *Soft Matter*, 2016, **12**, 4375–4383.

25 K. A. Macmillan, J. R. Royer, A. Morozov, Y. M. Joshi, M. Cloitre and P. S. Clegg, *Langmuir*, 2019, **35**, 10927–10936.

26 P. S. Clegg and J. H. J. Thijssen, in *Bijels: Bicontinuous Particle-stabilized Emulsions*, ed. P. S. Clegg, Royal Society of Chemistry, Cambridge, 2020, ch. 1, pp. 1-33.

27 C. Huang, J. Forth, W. Wang, K. Hong, G. S. Smith, B. A. Helms and T. P. Russell, *Nature Nanotechnology*, 2017, **12**, 1060–1063.

28 M. Reeves, A. T. Brown, A. B. Schofield, M. E. Cates and J. H. J. Thijssen, *Phys. Rev. E*, 2015, **92**, 032308.

29 J. H. J. Thijssen and J. Vermant, *Journal of Physics: Condensed Matter*, 2018, **30**, 023002.

30 M. Reeves, K. Stratford and J. H. J. Thijssen, *Soft Matter*, 2016, **12**, 4082–4092.

31 M.-T. Hsieh, B. Endo, Y. Zhang, J. Bauer and L. Valdevit, *Journal of the Mechanics and Physics of Solids*, 2019, **125**, 401–419.

32 A. D. Dinsmore and D. A. Weitz, *J. Phys.: Condens. Matter*, 2002, **14**, 7581–7597.

33 E. Zaccarelli and W. C. K. Poon, *Proceedings of the National Academy of Sciences*, 2009, **106**, 15203–15208.

34 K. N. Pham, G. Petekidis, D. Vlassopoulos, S. U. Egelhaaf, P. N. Pusey and W. C. K. Poon, *Europhys. Lett.*, 2006, **75**, 624–630.

35 Z. Shao, A. S. Negi and C. O. Osuji, *Soft Matter*, 2013, **9**, 5492.

36 T. E. Daubert and R. P. Danner, *Physical and thermodynamic properties of pure chemicals : data compilation*, Taylor & Francis, Washington, DC, 1989.

37 V. Pokorný, V. Štejfa, M. Fulem, C. Červinka and K. Růžička, *J. Chem. Eng. Data*, 2017, **62**, 4174–4186.

38 M. Oettel and S. Dietrich, *Langmuir*, 2008, **24**, 1425–1441.

39 H. Ching, T. J. Thorson, B. Paul and A. Mohraz, *Mater. Adv.*, 2021, **2**, 5067–5075.

40 N. Hijnen, D. Cai and P. S. Clegg, *Soft Matter*, 2015, **11**, 4351–4355.

41 F. Bonaccorso, S. Succi, M. Lauricella, A. Montessori, A. Tiribocchi and K. H. Luo, *AIP Advances*, 2020, **10**, 095304.

42 M. M. van Schooneveld, V. W. A. de Villeneuve, R. P. A. Dullens, D. G. A. L. Aarts, M. E. Leunissen and W. K. Kegel, *J. Phys. Chem. B*, 2009, **113**, 4560–4564.

43 M. T. Elsesser and A. D. Hollingsworth, *Langmuir*, 2010, **26**, 17989–17996.

44 F. Bossler and E. Koos, *Langmuir*, 2016, **32**, 1489–1501.

45 E. Sanz, K. A. White, P. S. Clegg and M. E. Cates, *Phys. Rev. Lett.*, 2009, **103**, 255502.

46 C. Zeng, F. Brau, B. Davidovitch and A. D. Dinsmore, *Soft Matter*, 2012, **8**, 8582.

47 K. D. Danov, P. A. Kralchevsky, B. N. Naydenov and G. Brenn, *Journal of Colloid and Interface Science*, 2005, **287**, 121–134.

48 P. A. Kralchevsky, N. D. Denkov and K. D. Danov, *Langmuir*, 2001, **17**, 7694–7705.

49 V. M. Gun'ko, M. S. Vedamuthu, G. L. Henderson and J. P. Blitz, *Journal of Colloid and Interface Science*, 2000, **228**, 157–170.

50 M. Siebenbürger, M. Fuchs, H. Winter and M. Ballauff, *Journal of Rheology*, 2009, **53**, 707–726.

51 T. Domenech and S. S. Velankar, *Soft Matter*, 2015, **11**, 1500–1516.

52 R. Foudazi, S. Qavi, I. Masalova and A. Ya. Malkin, *Advances in Colloid and Interface Science*, 2015, **220**, 78–91.

53   N. Sanatkaran, M. Zhou and R. Foudazi, *Journal of Rheology*, 2021, **65**, 453–461.

54   S. Ankiewicz, N. Orbey, H. Watanabe, H. Lentzakis and J. Dealy, *Journal of Rheology*, 2016, **60**, 1115–1120.

55   Z. Emami, M. Ehsani, M. Zandi and R. Foudazi, *Carbohydrate Polymers*, 2018, **198**, 509–517.

56   Z. Németh, L. Halász, J. Pálinkás, A. Bóta and T. Horányi, *Colloids and Surfaces A: Physicochemical and Engineering Aspects*, 1998, **145**, 107–119.

57   R. A. Lionberger and W. B. Russel, *Journal of Rheology*, 1994, **38**, 1885–1908.

58   H. Zhang, K. Yu, O. J. Cayre and D. Harbottle, *Langmuir*, 2016, **32**, 13472–13481.

59   S. Reynaert, P. Moldenaers and J. Vermant, *Phys. Chem. Chem. Phys.*, 2007, **9**, 6463.

60   T. G. Mason and D. A. Weitz, *Physical Review Letters*, 1995, **75**, 2770–2773.

61   E. Di Cola, A. Moussaïd, M. Sztucki, T. Narayanan and E. Zaccarelli, *The Journal of Chemical Physics*, 2009, **131**, 144903.

62   W. Götze and L. Sjögren, *Phys. Rev. A*, 1991, **43**, 5442–5448.

63   X. Ji, X. Wang, Y. Zhang and D. Zang, *Rep. Prog. Phys.*, 2020, **83**, 126601.

64   F. Weysser and D. Hajnal, *Phys. Rev. E*, 2011, **83**, 041503.

65   R. H. Ewoldt, M. T. Johnston and L. M. Caretta, *Complex Fluids in Biological Systems: Experiment, Theory, and Computation*, Springer New York, New York, NY, 2015.

66   J. Bergenholtz, M. Fuchs and T. Voigtmann, *J. Phys.: Condens. Matter*, 2000, **12**, 6575–6583.

67   A. Maestro, O. S. Deshmukh, F. Mugele and D. Langevin, *Langmuir*, 2015, **31**, 6289–6297.

68   E. Koos and N. Willenbacher, *Science*, 2011, **331**, 897–900.

69   A. Maestro and A. Zaccone, *Nanoscale*, 2017, **9**, 18343–18351.

70   J. Yang and S. S. Velankar, *Journal of Rheology*, 2017, **61**, 217–228.

71   J. S. Bee, D. K. Schwartz, S. Trabelsi, E. Freund, J. L. Stevenson, J. F. Carpenter and T. W. Randolph, *Soft Matter*, 2012, **8**, 10329.

72   M. F. Haase, H. Jeon, N. Hough, J. H. Kim, K. J. Stebe and D. Lee, *Nature Communications*, , DOI:10.1038/s41467-017-01409-3.

73   F. Günther, F. Janoschek, S. Frijters and J. Harting, *Computers & Fluids*, 2013, **80**, 184–189.

74   H.-L. Cheng and S. S. Velankar, *Langmuir*, 2009, **25**, 4412–4420.

75   J. Witt, D. R. Mumm and A. Mohraz, *Soft Matter*, 2013, **9**, 6773–6780.

76   D. J. French, A. B. Schofield and J. H. J. Thijssen, *Adv Materials Inter*, 2022, **9**, 2102307.

77   K. M. McDevitt, T. J. Thorson, E. L. Botvinick, D. R. Mumm and A. Mohraz, *Materialia*, 2019, **7**, 100393.

78   G. Di Vitantonio, T. Wang, M. F. Haase, K. J. Stebe and D. Lee, *ACS Nano*, 2019, **13**, 26–31.

79   Y. Zhang, M.-T. Hsieh and L. Valdevit, *Composite Structures*, 2021, **263**, 113693.

80   S. P. Kharal and M. F. Haase, *Small*, 2022, **18**, 2106826.

81   E. R. Weeks, *Science*, 2000, **287**, 627–631.

82   M. Kaganyuk and A. Mohraz, *Soft Matter*, 2020, **16**, 4431–4443.

83   K. N. Pham, S. U. Egelhaaf, P. N. Pusey and W. C. K. Poon, *Phys. Rev. E*, 2004, **69**, 011503.

84   G. Petekidis and N. J. Wagner, in *Theory and Applications of Colloidal Suspension Rheology*, eds. N. J. Wagner and J. Mewis, Cambridge University Press, 1st edn., 2021, pp. 173–226.

85   A. W. K. Ma, F. Chinesta and M. R. Mackley, *Journal of Rheology*, 2009, **53**, 547–573.

86   M. Kapnistos, A. N. Semenov, D. Vlassopoulos and J. Roovers, *The Journal of Chemical Physics*, 1999, **111**, 1753–1759.

87   B. L. Peters, K. M. Salerno, T. Ge, D. Perahia and G. S. Grest, *Macromolecules*, 2020, **53**, 8400–8405.

88   A. J. Liu and S. R. Nagel, *Nature*, 1998, 21–22.

89   L. M. C. Janssen, *Front. Phys.*, 2018, **6**, 97.

90   A. Ghosh, V. Chikkadi, P. Schall and D. Bonn, *Phys. Rev. Lett.*, 2011, **107**, 188303.

91   F. Scheffold and P. Schurtenberger, *Soft Materials*, 2003, **1**, 139–165.

92   K. Hyun, M. Wilhelm, C. O. Klein, K. S. Cho, J. G. Nam, K. H. Ahn, S. J. Lee, R. H. Ewoldt and G. H. McKinley, *Progress in Polymer Science*, 2011, **36**, 1697–1753.

93   A. J. Mendoza, E. Guzmán, F. Martínez-Pedrero, H. Ritacco, R. G. Rubio, F. Ortega, V. M. Starov and R. Miller, *Advances in Colloid and Interface Science*, 2014, **206**, 303–319.

94   P. R. de Souza Mendes, *Soft Matter*, 2011, **7**, 2471.

95   K. Kamani, G. J. Donley and S. A. Rogers, *Phys. Rev. Lett.*, 2021, **126**, 218002.

96   C. J. Dimitriou, R. H. Ewoldt and G. H. McKinley, *Journal of Rheology*, 2013, **57**, 27–70.

97   H.-Y. Chen, Y. Kwon and K. Thornton, *Scripta Materialia*, 2009, **61**, 52–55.

98   J. W. Tavacoli, J. H. J. Thijssen and P. S. Clegg, in *RSC Soft Matter Series*, eds. T. Ngai and S. Bon, Royal Society of Chemistry, Cambridge, 2014, pp. 129–168.

99   A. Mohraz, 27.

100   J. W. Cahn, *The Journal of Chemical Physics*, 1965, **42**, 93–99.

101   A. L. Genau and P. W. Voorhees, *Acta Materialia*, 2009, **57**, 6226–6233.

102   E. Kim, K. Stratford, R. Adhikari and M. E. Cates, *Langmuir*, 2008, **24**, 6549–6556.

103   N. Wong and C. M. Knobler, 1978, **69**, 12.

104   R. Van Der Haegen and B. W. Ready, in *Comprehensive Polymer Science and Supplements*, Pergamon, Oxford, 1989, pp. 34–60.

105   D. Cai and P. S. Clegg, *Chemical Communications*, 2015, **51**, 16984–16987.

106   X.-D. Wang, Z.-X. Shen, T. Sang, X.-B. Cheng, M.-F. Li, L.-Y. Chen and Z.-S. Wang, *Journal of Colloid and Interface Science*, 2010, **341**, 23–29.

107   S. A. Kulkarni, S. B. Ogale and K. P. Vijayamohanan, *Journal of Colloid and Interface Science*, 2008, **318**, 372–379.

108   P. A. Kralchevsky, I. B. Ivanov, K. P. Ananthapadmanabhan and A. Lips, *Langmuir*, 2005, **21**, 50–63.

109   B. P. Binks and J. H. Clint, *Langmuir*, 2002, **18**, 1270–1273.

110   H. Tanaka, *Physical Review Letters*, 1993, **71**, 3158–3161.

111   H. Tanaka, *The Journal of Chemical Physics*, 1994, **100**, 5323–5337.

112   J. K. Yeganeh, F. Goharpey and R. Foudazi, *RSC Advances*, 2014, **4**, 12809.

113   G. Zhang, T. Yang, S. Yang and Y. Wang, *Physical Review E*, , DOI:10.1103/PhysRevE.96.032501.

114   H. M. Tanaka, *Progress of Theoretical Physics*, 1999, **101**, 863–873.

115   D. Sappelt and J. Jäckle, *Polymer*, 1998, **39**, 5253–5256.

116   F. Jansen and J. Harting, *Phys. Rev. E*, 2011, **83**, 046707.

117   K. E. Novik and P. V. Coveney, *Phys. Rev. E*, 2000, **61**, 435–448.

118   W. M. Deen, *Analysis of transport phenomena*, Oxford University Press, New York, 1998.

119   A. Priola, G. Gozzelino, F. Ferrero and G. Malucelli, *Polymer*, 1993, **34**, 3653–3657.

120   S. Kalakkunnath, D. S. Kalika, H. Lin and B. D. Freeman, *J. Polym. Sci. B Polym. Phys.*, 2006, **44**, 2058–2070.

121   M. Kim and C. Cha, *Sci Rep*, 2018, **8**, 4315.

122   A. Van Blaaderen and A. Vrij, *Langmuir*, 1992, **8**, 2921–2931.

123   J. Georges, *Spectrochimica Acta Part A: Molecular and Biomolecular Spectroscopy*, 1995, **51**, 985–994.

124   H. S. Fogler, *Elements of Chemical Reaction Engineering*, Prentice Hall, Upper Saddle River, 2006.